Transverse electron beam diagnostics at REGAE

Dissertation

zur Erlangung des Doktorgrades
des Fachbereichs Physik
der Universität Hamburg

vorgelegt von

Shima Bayesteh
aus Teheran

Hamburg
2014

Gutachter der Dissertation	Prof. Dr. Jörg Roßbach Prof. Dr. Markus Drescher
Gutachter der Disputation	Prof. Dr. Jörg Roßbach Prof. Dr. Markus Drescher Prof. Dr. R.J. Dwayne Miller Dr. Klaus Flöttmann
Datum der Disputation	17.10.2014
Vorsitzender des Prüfungsausschusses	Prof. Dr. Michael Alexander Rübhausen
Vorsitzender des Promotionsausschusses	Prof. Dr. Peter Hauschildt
Leiterin des Fachbereichs Physik	Prof. Dr. Daniela Pfannkuche
Dekan der MIN-Fakultät	Prof. Dr. Heinrich Graener

Abstract

The use of high-intensity electron and X-ray pulsed sources allows for the direct observation of atomic motions as they occur. While the production of such high coherent, brilliant, short X-ray pulses requires large-scale and costly accelerator facilities, it is feasible to employ a high-intensity source of electrons by exploiting a more compact design. The Relativistic Electron Gun for Atomic Exploration (REGAE) facility is a small linear accelerator at DESY, Hamburg, equipped with a photocathode radio frequency (RF) gun that produces relativistic ultra-short (<100 fs), low charge (<1 pC) electron bunches of high coherence. By means of time-resolved diffraction experiments, such an electron source can probe ultrafast laser-induced atomic structural changes that occur with a temporal resolution of $\sim$100 fs. A comprehensive characterization of the electron beam, for every pulse, is of fundamental importance to study the atomic motions with the desired resolution and quality. This thesis reports on the transversal diagnostics of the electron beam with an emphasis on a scintillator-based beam profile monitor. The diagnostics is capable of evaluating the beam parameters such as charge, energy, energy spread and transverse profile, at very low charges and on a shot-to-shot basis. A full characterization of the scintillator's emission, the optical setup and the detector (camera) of the profile monitor is presented, from which an absolute charge calibration of the system is derived. The profile monitor is specially developed to accommodate more applications, such as dark current suppression, overlapping the electron probe and the laser pump within 1 ns accuracy, as well as charge and transverse emittance measurements. For the determination of the transverse emittance two techniques were applied. The first one introduces a new method that exploits a diffraction pattern to measure the emittance, while the second one is based on a version of the Pepper-pot technique. A comparison of the measured emittance values to the ones obtained from simulations, shows that they are in agreement. It is demonstrated that with an excellent sensitivity that enables the determination of both the transverse charge distribution and the emittance at very low charges, the profile monitors can provide a measure of the coherence of the beam, as well as of the diffraction quality in every shot of a progressive sequence.

Zusammenfassung

Die Verwendung von hochintensiven gepulsten Elektronen- und Röntgen- quellen erlaubt die direkte und unmittelbare Beobachtung atomarer Bewegungen. Während die Erzeugung solcher Röntgenpulse große und teure Beschleunigeranlagen erfordert, ist es möglich, eine hochintensive Elektronenquelle in einer kompakteren Bauweise zu realisieren. Die neuartige Quelle für relativistische Elektronenstrahlen REGAE (Relativistic Electron Gun for Atomic Exploration) ist ein kleiner Linearbeschleuniger bei DESY, Hamburg, der auf einer Photokathoden Hochfrequenz-Quelle (RF-Gun) basiert. Die Anlage ist geeignet, relativistische, ultrakurze (<100 fs) Elektronenpakete von niedriger Ladung (<1 pC) und hoher Kohärenz herzustellen. Mittels zeitaufgelöster Beugungsexperimente können an dieser Elektronenquelle laserinduzierte, ultraschnelle atomare Strukturveränderungen, die mit einer zeitlichen Auflösung von ca. 100 fs auftreten, untersucht werden. Für jeden Puls ist eine umfassende Charakterisierung des Elektronenstrahls von grundlegender Bedeutung, um die Atombewegungen mit der gewünschten Auflösung und Qualität zu bestimmen. In dieser Dissertation wird über die transversale Diagnostik des Elektronenstrahls mit einem Schwerpunkt auf einen szintillatorbasierten Strahlprofilmonitor berichtet. Die Diagnostik ist ein sehr sensitives System, das die Parameter des Strahls, wie Ladung, Energie, Energiebreite und das transversale Profil bei sehr niedrigen Ladungen und auf einer "shot-to-shot" Basis messen kann. Eine vollständige Charakterisierung der Szintillator-Emission, des optischen Aufbaus und des Detektors (Kamera) wird diskutiert und eine absolute Ladungskalibration des Systems abgeleitet. Der Profilmonitor wurde entwickelt um Applikationen, wie zum Beispiel die Unterdrückung des Dunkelstroms und die räumliche und zeitliche Überlappung des Elektronenstrahls mit dem Pumplaser innerhalb 1 ns, sowie die Messungen der Ladung und der transversalen Emittanz zu ermöglichen. Für die Vermessung der transversalen Emittanz werden zwei Techniken angewendet. Bei der ersten wird eine neue Methode, die ein Beugungsmuster benutzt, vorgestellt, während die zweite auf einer Variante der "Pepper-Pot" Technik basiert. Die gemessene Emittanz ist in Übereinstimmung mit den Ergebnissen von Simulationen. Es wird gezeigt, dass die Profilmonitore eine ausgezeichnete Sensitivität haben, die die Vermessung sowohl der transversalen Landungsverteilung als auch der Emittanz bei niedrigen Landungen ermöglicht, woraus ein Maß für die Kohärenz des Strahls und der Qualität der Beugung abgeleitet werden kann.

Declaration

I herewith declare, on oath, that I have produced this thesis without the prohibited assistance of third parties and without making use of aids other than those specified; notions taken over directly or indirectly from other sources have been identified as such. This thesis has not previously been presented in identical or similar form to any other German or foreign examination board.

Contents

List of Figures

List of Tables

Preface

Exploring the atomic structure of matter, through the diffraction phenomenon, requires sources of high coherence and brilliance with short wavelengths. However, the real-time probe of atomic structural changes, introduces a new demand. The pulse length of the source should be comparable or shorter than the dynamic process to be able to resolve it temporally. The research of ultra fast phenomena, such as chemical and biochemical reactions and phase transitions, are based on pump-probe experiments. While the short-pulse laser sources are used as the pump, the appropriate sources for the probe are coherent X-rays and electrons. In fact, electron sources are brighter and interact more strongly with the matter. Nevertheless, the repulsive space charge forces associated with the electrons should be dealt with. In the first chapter, an introduction to electron diffraction, as well as its major advantages and disadvantages over the optical X-ray diffraction, are presented. The superiority of the RF-gun based electron sources for ultra-fast time-resolved diffraction experiments, such as REGAE (Relativistic Electron Gun for Atomic Exploration), is also discussed. The REGAE facility comprises of a linear accelerator, which serves a photocathode RF gun to produce electrons of up to 5 MeV, for Femtosecond Electron Diffraction (FED) experiment. It enables a direct atomic level view of transition states. A detailed description of REGAE, as well as the operation procedure are presented in Chapter 2.

The effective operation of such an accelerator facility would not be possible without diagnosing the electron beam. Hence, diagnostics tools, capable of characterizing the beam are required to obtain and maintain the desired beam parameters. The diagnostics at REGAE cover charge, energy, energy spread and beam profile measurements. In order to overcome the bunch length broadening due to the space charge effects, the design bunch charge for the pump-probe experiment is very low. Consequently, the charge and beam profile measurements are influenced and the relevant diagnostics should be adapted for this purpose. They all show a great sensitivity at ultra-low charges and are capable of performing single shot measurements. The developed beam profile monitors operate based on the conversion of electrons to visible light by means of a scintillator material. The first step towards evaluating the beam profile monitors is to characterize the scintillator emission. Chapter 3 describes properties of the selected scintillator materials for the purpose of diagnostics and diffraction detection at REGAE. Furthermore, the angular distribution and intensity of the emission from those scintillators are investigated using a Monte Carlo simulation software, GEANT4.

In Chapter 4 the optical design of the profile monitors is described. By coupling an image intensifier to a normal CCD, two detection lines (intensified-CCD and CCD) are implemented into the beam profile monitor setup. This feature offers a wider dynamic range, in which the beam profile can be measured. A full evaluation of the system leads to the determination of the imaging resolution, which is then convolved with the scintillator emission spread to acquire the total resolution of the profile monitor. Other diagnostics such as charge, energy and energy spread are also explained in this chapter. The proper choice of detector is of importance for the diagnostics and an evaluation of different detectors used at REGAE is presented in Chapter 5. An absolute calibration of the detectors, as well as a comparison of their sensitivity are also given.

By means of the diagnostics and especially the beam profile monitors, different measurements were performed and their results are presented and interpreted in Chapter 6. The decay time of the scintillator and the transverse emittance of the beam were measured. In addition, the excellent sensitivity of the beam profile monitors at ultra-low charges, the suppression of the RF induced dark current signal by means of a gated ICCD and also the overlap between the pump laser and the probe electron pulses within 1 ns are demonstrated.

Chapter 1

Introduction to electron diffraction

Electrons can be used to probe the atomic structure of matter through two main distinct modes, transmission electron microscopy (TEM) and electron diffraction. The latter is a demonstration of the wave nature of electrons as well as their particle nature. The electron diffraction phenomenon was observed for the first time by Davisson [1] and Germer and independently by Thomson and Reind, after de Broglie proposed that particles also behave like waves [2, 3] with wavelengths given by:

$$\lambda = \frac{h}{p}, \tag{1.1}$$

where p is the particle momentum and h is Planck's constant. In order to resolve the positions of the atoms in a crystal lattice plane, the wavelength of the probe must be smaller than the characteristic atomic spacing. In particular, hard X-rays of an energy of 10 keV and electrons with a de Broglie wavelength of less than 1 $\AA$ are suitable for studies of atomic structure. When the incident electrons are elastically scattered due to interaction with the charged nuclei and electrons of the specimen through the Coulomb field, scattered waves from the atomic planes interfere and form a diffraction pattern. The constructive interference takes place provided that Bragg's condition is satisfied,

$$n\lambda = 2dsin\theta, \tag{1.2}$$

where n is the integer which represents the order of diffraction, λ is the de Broglie wavelength, d is the spacing between the atomic planes (diffracting planes) and θ is the Bragg angle. The electrons are thus scattered with an angle of two times the Bragg angle. In the crystal structure, the smallest repeating unit is called the unit cell. Many metals, such as gold and aluminum, form crystals with a face centered cubic (FCC) unit cells. The structure is described as a right angled cube with an atom at each corner of the unit cell and an atom situated in the middle of each face of the unit cell. The atomic plane spacing is then formulated as:

$$d = \frac{a}{\sqrt{h^2 + k^2 + l^2}}, \tag{1.3}$$

where a is the lattice parameter or the unit cell's dimension and h, k, l are Miller indices which show the orientation of the diffracting planes with respect to the crystal unit cell axes. Constructively interfering electrons create Bragg peaks which correspond to bright points in the diffraction pattern. Diffraction contrast within a single crystal would emerge as a spot pattern, while through a polycrystalline material a ring diffraction pattern is formed. Many inorganic materials are polycrystalline and contain small crystals, so called crystallites. The arising spots from Bragg reflection of each individual crystallite contribute to the formation of the diffraction rings. The azimuthal angle, ϕ (see Fig. 1.1) of a spot is determined by the azimuthal orientation of a crystallite around the direction of the incident beam. Due to the random azimuthal orientation of the crystallites, many diffracted spots from the crystallites with the same scattering angle and distinct azimuthal angles form a ring [4]. Each ring, or order of diffraction, corresponds to a different orientation and atomic plane spacing (d). If the lattice parameter is known and the Miller indices are recognized, then the wavelength of the incident electrons can be deduced. In another case, if the energy of the incoming electron beam is known with a decent accuracy, the lattice parameter is attained. In both cases, the spacing between the undiffracted electrons and the Bragg peaks leads to a measurement of the scattering angle.

In the TEM mode, electrons penetrate a thin specimen, interact with it and image the exposed part of the specimen on a downstream detector. This resembles, to a large extent, the known light microscopes, with the advantage of providing more profound vision of the atomic structures. The imaging system is substantial for electron microscopes. In Fig. 1.2 a schematic of a conventional electron microscope is depicted. It provides a magnified image of the atomic positions inside the sample specimen. The first lens before the sample, the condenser, concentrates the near-parallel electron source onto the specimen. The objective lens then gathers the scattered electrons on the back focal plane (BFP) to construct a diffraction pattern and then focuses them on the image plane in a real space imaging scheme. The TEM setup can also contain an intermediate lens which serves as a magnification tuner, when its focal length is varied. Apart from that, it facilitates the electron microscope operation in diffraction mode, as well as in imaging mode. The final element is a projector lens, which produces an image, or a diffraction pattern, across the TEM screen.

1.1 Observing the dynamics of atomic structures

Far more important than observing the atomic structures of matter in a static mode is to resolve the atomic structural changes as they occur. Ultra-fast Electron Diffraction (UED) paves the path towards observing the atomic motions in real time, which has a strong impact on an extensive area in science, including physics, chemistry and biology. The main concept is the use of short electron bunches to probe fast processes

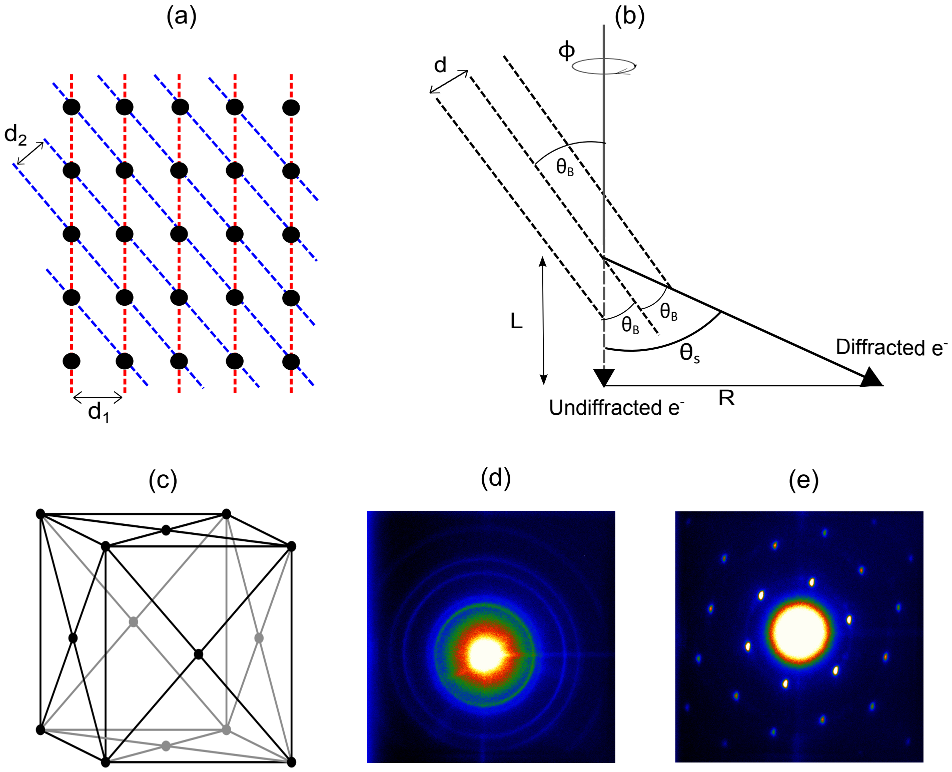

Figure 1.1: (a) A cubic lattice with an atom at each lattice point. The vertical and diagonal lines are the diffraction planes with lattice spacing of d_1 and d2. (b) Diffraction of electrons from an atomic plane with spacing d. If the reflected electrons from the planes are satisfying the Bragg's condition, Bragg peaks are formed as a result of constructive interference of the electrons' wavefronts. θ_B is the Bragg angle and θ_s is the scattering angle which is two times larger than the Bragg angle. (c) A unit cell of a face centered cubic crystal is illustrated. A right angled cube with an atom at each corner of the unit cell and an atom situated in the middle of each face of the unit cell. (d) Ring diffraction pattern of a polycrystalline material. (e) An example of a spot diffraction pattern from a single crystal. Both images have been obtained at REGAE.

in specimens, while they evolve. The required shutter speed to capture atomic motions during the transition state fits to a 100 fs timescale or even less [5–8]. In other words, in order to temporally resolve the afore mentioned fast processes, electron bunches of the same length or shorter are needed. The availability of femtosecond lasers, facilitates the generation of such short bunches. Nevertheless, the atomic position in space needs to be resolved, which explains the use of electrons with de Broglie wavelengths much smaller than the characteristic atomic spacing. Another alternative source for atomically resolved dynamics are hard X-rays. In a comparison, the scattering cross section of the electrons is much higher than that of X-rays, by a factor of $10^5 - 10^6$ [7, 9, 10]. This means that for the same intensity of the diffraction, fewer $(10^5 - 10^6)$ electrons are needed. Thus, the main difficulty in employing electron bunches, which is the space-charge broadening due to Coulomb repulsion between the electrons, can be relaxed to some extent. Space charge broadening becomes critical for Femtosecond Electron Diffraction (FED), where electron bunches should be compressed to the femtosecond

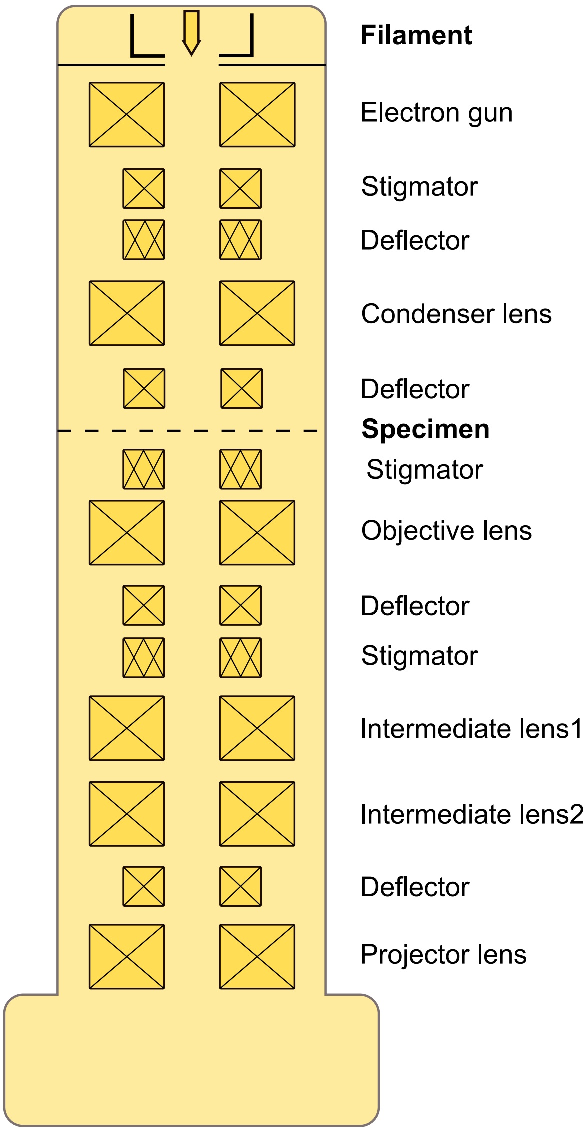

FIGURE 1.2: Schematic of a conventional electron microscope. The electrons are generated by a filament and then accelerated through an electron gun. The condenser lens concentrates the beam onto the specimen. After that, the objective and projector lens can create either the diffraction pattern or the image of the transmitted electron through the specimen. The intermediate lenses tune magnification of the image of the microscope. The deflectors adjust the alignment of the electron path along the microscope and the stigmators correct astigmatism effect.

length regime. As a solution to the space charge effects, probe electron bunches of low charge are of interest, with a peak current which produces the required diffraction intensity in a single shot. Electrons can be generated through a table-top or small-size experiment, while generation of highly coherent X-rays requires more complicated and expensive facilities. Third generation Synchrotron light sources, fourth generation light sources, XFELs, and also table-top plasma sources can produce X-rays for the desired time-resolved experiments. The third generation light sources lower the transverse emittance and improve the concentration of the radiation, so called brilliance, by orders of magnitude with respect to the previous generations of synchrotron radiation. Modern synchrotron facilities such as PETRAIII [11] in Germany, Spring-8 in Japan [12] and ESRF in France [13] are capable of producing hard X-rays, being served for time-resolved studies. However, the typical bunch length of ∼picosecond does not suit them to study the fast femtosecond processes. In fourth generation light sources, the performance is significantly increased in important parameters of the beam like, brightness, coherence and pulse duration. Linac-based FELs offer sub-ps X-ray pulses of high density and fully coherent in transverse plane, which suit for the atomically resolved studies in single shot. FLASH in Germany [14], LCLS in the USA [15], FERMI@Elettra in Italy [16] and SACLA in Japan [17] are the FEL facilities, capable of generating soft and hard X-rays. With the X-rays, the beam intensity is not limited like the in case of the electrons, however since the deposited energy in the sample is significantly higher as compared to the electrons, the crystals can be destroyed in a single shot. In contrast, crystal damage caused by electrons in electron diffraction experiments is negligible.

In order to avoid multiple scattering of electrons from a specimen, the thickness of the solid state sample should be of the order of hundreds of nanometers, while the typical sample thickness in the X-ray diffraction can be 10-100 μm. This is a consequence of the strong interaction between electrons and atoms. Based on this fact, there are strong constraints on the preparation of the sample, especially in the course of irreversible sampling, within a laser pump-electron probe experiment, when the samples have to be replaced. Therefore, the structural studies should be performed in near single shot condition.

1.2 RF gun based relativistic electron diffraction on femtosecond time scale

For the purpose of electron microscopy, electrons are accelerated via DC guns fields. Beforehand, the extraction of electrons from a cathode surface can be realized through thermionic emission, field emission or photoemission. If a material is heated up to sufficiently high temperature, the electrons gain enough energy to overcome the work function. A thermionic cathode (filament) functions on this basis. When the electrostatic field on the surface of a metal is increased sufficiently, the electrons, instead of escaping over the potential barrier to overcome the work function, escape through it by quantum-mechanical tunneling. Based on this phenomenon, field emission cathodes are designed. In the photo-emission process, electrons are released from the cathode due to the photo-electric effect, after being exposed to the laser beam. After electrons are extracted from the cathode, they are accelerated to their final kinetic energy as a result of a potential difference between the cathode and an anode surface for a specific period of time. Typical DC guns yield energies of a few hundred keV. Due to design constraints, the extraction field has a maximum value of ∼10 MV/m. The first observation of atomic motions on a femtosecond timescale and taking advantage of a new concept of a very compact electron gun design, was demonstrated by Siwick et al in 2003 [18]. In this work, a photo-cathode electron gun provided sub-500 fs high density electron bunches to probe the structural dynamics of a melting process. On the basis of the mentioned compact design, the achieved temporal resolution of the structural dynamics is better than 200 fs [19]. In compact DC guns, the electron pulse broadening is reduced due to the short propagation distance. However, by going to the relativistic regime, the space-charge effect and consequently the pulse broadening are significantly suppressed. In both longitudinal and transverse direction, the growth of the bunch as a result of the space charge field scales as $1/\gamma^3$ [20]. Due to the suppression of the space-charge effect within the relativistic regime, further compression of the electron pulse becomes feasible. Moreover, the transverse momentum spread caused by the space-charge force is reduced and consequently the transverse emittance is improved. Finally it can be concluded that the temporal and spatial resolution of the probing process is better preserved by increasing the energy of the electrons.

One of the most important parameters of UED, which has a great impact on the diffraction quality, is transverse coherence length (L_c). Longer coherence length in transverse plane expresses a better ability to observe interference phenomenon. This characteristic distance should be several times the unit cell dimensions of the under study specimen. The relation between the coherence length, the beam quality (beam emittance) and the beam optics (beam size) is expressed as follows [21],

$$L_c \approx \frac{\hbar}{mc} \frac{\sigma_x}{\epsilon_n}, \tag{1.4}$$

with σ_x and ϵ_n as the RMS beam size and emittance. The smaller and better the transverse emittance, the longer the coherence length is.

Regarding the samples thickness, since the mean free path of MeV electrons increases relative to non-relativistic electrons, the samples can be thicker. A normal conducting RF-gun based on the photoelectron emission is capable of accelerating the electrons up to several MeVs. The accelerating gradient can reach several tens of MV/m. An RF compression cavity can be used to focus the electron beam longitudinally.

The Relativistic Electron Gun for Atomic Exploration (REGAE) is one of the pioneering facilities in the world, which serves relativistic electrons of 2–5 MeV for static and dynamic electron microscopy [22]. A beam compression down to several femtoseconds at the sample position which is necessary to achieve the equivalent resolution of the observation of atomic motions, is expected. The RF stability in phase and amplitude, as well as the precision of determining the time zero have been improved during 2013 and are approaching the design goal. In chapter 2, a complete description of the entire facility is given. Atomically resolved dynamics in diffraction mode is the main focus of the REGAE project so far. However, there are ongoing efforts to perform studies in the real space imaging mode. Hence, a lens system capable of collimating and focusing the electrons and finally magnifying the image is needed. Focusing electrons through such a lens system increases the space-charge force and constrains both the temporal and spatial resolution of the sampling. Nevertheless, relativistic electrons have a smaller de Broglie wavelength than electrons of lower energy. Eventually, due to space charge effects, the spatial resolution will be worse than the conventional TEMs, which is the price to pay for the gain in temporal resolution.

1.3 Existing relativistic femtosecond electron diffraction facilities

In order to give an impression of ongoing RF gun-based ultra-fast studies in the world, a few facilities are mentioned and their achieved prominent results are shortly discussed.

The first demonstration of relativistic electron diffraction, using a photocathode RF gun, was presented by Hastings et al [23] in 2006. They observed single-shot static diffraction patterns from a 160 nm Aluminum foil using the 5.4 MeV electron beam from the Gun Test Facility at the Stanford Linear Accelerator. No attempt for time-resolved sampling was made in this demonstration experiment.

At the UCLA Pegasus RF photoinjector facility, laser-induced melting of a single crystal gold foil by time-resolved relativistic electron diffraction was reported [24]. The beam energy and charge was 3.5 MeV and $\sim$1 pC, respectively. The electron bunch length was measured to be less than 200 fs, using an RF deflector. In that experiment, a timing jitter of ±800 fs was present as a result of RF amplitude jitter and phase fluctuation, which adds an uncertainty to the probing resolution of the melting process, since it was recorded in several shots.

The structural evolution within several picoseconds was continuously resolved with $\sim$200 fs resolution at the Tsinghua (Thomson Scattering X-ray source TTX) facility. An S-band RF deflector was used to streak the diffraction pattern of a single crystal of gold with a thickness of 20 nm. The beam energy, charge and length were 2.7 Mev, 0.34 pC and 5.5 ps, respectively. With the mentioned resolution of $\sim$200 fs, the whole structural dynamics was captured in one shot [25].

At Osaka university, a compact ultrafast electron diffractometer has been developed. It generates MeV electron pulses from a laser-driven photocathode. Three electromagnetic lenses are employed around the target chamber. A condenser lens focuses the beam onto the sample and the diffraction pattern is magnified by the last two lenses. The movable projecting lens allows a variation of the magnification of the diffraction image. They observed single shot static electron diffraction from a 180-nm-thick single crystal of Silicon with an excellent quality, using electrons of 3 MeV.

Chapter 2

Relativistic Electron Gun for Atomic Exploration (REGAE)

REGAE is a small linear accelerator constructed and operated in the framework of the Center for Free Electron laser (CFEL), in a collaboration of Max Planck society, Hamburg university and DESY. The facility is located at the DESY campus in Hamburg, Germany. A Radio Frequency (RF) photoinjector system provides electron bunches of high coherence for Femtosecond Electron Diffraction (FED) experiments. The first electron beam at REGAE was launched in November 2011. The atomic structures of the samples under investigation are deduced from the electron diffraction pattern. However, the main goal is to observe structural changes which occur as a result of chemical reactions or phase transitions on short time scales of the order of several femtoseconds. Thus, based on beam optics simulations [26], the beam conditions should be arranged such that space charge effects drop significantly and the bunch can be compressed down to $\sim$7 fs. This can be achieved when the electrons' energy is relativistic and the number of electrons in the bunch is lowered. A coherence length of 30 nm is required to study proteins via good quality electron diffraction patterns. It corresponds to the transverse emittance of about 7 nm rad with a beam size of 0.5 mm. The design parameters of the electron beam are presented in table 2.1. In this chapter, the elements of the REGAE facility and their applications are described. In addition, a general insight of the entire project, acquired results and also prospective potentials are briefly discussed.

2.1 RF (Radio Frequency) system

At REGAE 3GHz RF signals, generated by an RF generator (Master oscillator), are amplified by an RF amplifier and then by a klystron, which is supplied by a high voltage modulator. The high power RF from the klystron is conveyed by waveguides towards the accelerating cavities. A T-shaped shunt divides the power in a way that 75% of the power are fed through the RF coupler into the gun cavity and 25% into the buncher cavity. Both the gun and the buncher are standing wave S-band cavities. The gun cavity comprises of 1.5 cells, while for the buncher 4 cells are coupled to form the whole cavity.

Table 2.1: Acquired beam parameters at the sample position based on the beam dynamics simulations in ASTRA [26].

Repetition rate	< 50 Hz
Energy	2-5 MeV
Charge	<1 pC
Emittance	$\approx$ 7 nm rad @ 80 fC
Coherence length	30 nm
Bunch length	7 fs
Beam size	0.5 mm

The cylindrical cells are closed at both ends, except irises leaving only a small hole for the beam. If the cavity is filled with a electromagnetic wave, multiple reflections at both ends of the structures shape a standing wave. When the cavity cells are operating in the monopole modes (TM-modes), in which the longitudinal component of the magnetic field approaches zero, the longitudinal electric field of the studying wave contributes to accelerating the electrons. The structures of the cavities have been designed in such way that the resonance frequency in the monopole modes, which are the main operational modes, occur at 3 GHz. The cavities gradients relate to the distributed powers as follows:

$$E_{gun} = 47.67 \left[\frac{MV}{MW^{1/2}m}\right] \sqrt{P_{gun}}, \tag{2.1}$$

$$E_{buncher} = 29.02 \left[\frac{MV}{MW^{1/2}m}\right] \sqrt{P_{buncher}}, \tag{2.2}$$

where E is the peak gradient and P is the power, see Fig. 2.1.

The third harmonic of a Ti:Sapphire pulsed laser, 266 nm, is used to generate photoelectrons from a Cesium Teluride (Cs_2Te) or a metal photocathode, located in the back plane of the gun cavity. When the electrons are injected into the cavity at an RF phase where they gain maximal energy, the on-crest condition phase is met. In the buncher cavity, electrons are accelerated and compressed when the cavity is operated at an off-crest phase, such that the head of the bunch gains less energy than the tail from the electric field and an energy chirp is introduced to the bunch.

A phase shifter is located in the waveguide distribution arm for the gun. It consists of a 3 dB splitter, which forms a 4-port. Two ports form RF in and out, the other two are connected to arm that are short-cut. The length of the arms can be adjusted by using two stepper motors, which set the gun and buncher phase and power independently. In Fig. 2.2 the RF system is schematically displayed.

Because of the limited coupling efficiency, a part of the incoming power is always reflected and results in a cross talk of the cavity fields. Therefore, varying both phase shifters' positions equally and without an offset causes a change in the phase of the buncher and the gun with respect to each other, as well as to a change in the cavity amplitudes.

When the phase shifters move with an offset to each other, the power distributions into the cavities alter independently [27].

Due to the resistance of the cavity walls, ohmic heating takes place, and as a consequence the cavities expand. This effect results in a variation of the resonance frequency, leading to subsequent instability of the RF phase and amplitude. To prevent the expansion of the cavities and to ensure a constant resonance frequency, a water cooling system was designed. In order to operate with an RF temporal stability of ∼10 fs for the time-resolved experiment, an RF field stability of 0.01% in amplitude and 0.01 degree in phase are required [28]. Such requirements demand a temperature stability of 10^{-3} °C. Deviations of the temperature beyond this level of stability cause subsequent variations in the RF phase and amplitude which are corrected for by using the feedback loop in the Low Level RF (LLRF) system. The temperatures of the cavities are optimized by requiring that the RF signal reflection is minimal [27].

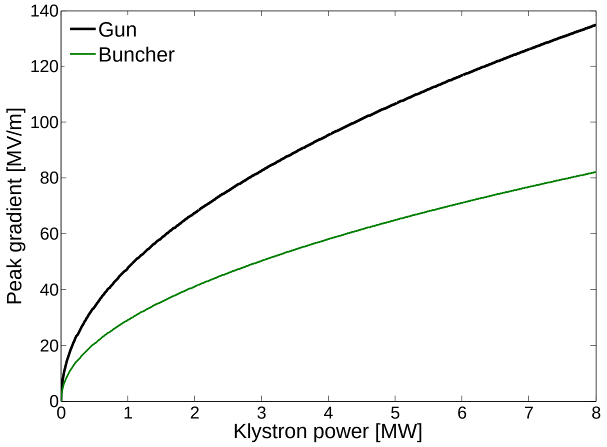

FIGURE 2.1: The gradient in the gun and the buncher cavities as a function of the klystron power. Courtesy of K. Flöttmann.

2.1.1 Low Level RF (LLRF) system

In order to maintain a time arrival jitter between the laser and the RF below 10 fs, the RF amplitude and phase should be stabilized within 0.01% and 0.01 degree, respectively. The LLRF is in charge of providing stable RF power synchronous to the laser.

A Master Oscillator (MO) is used as a reference clock for the REGAE RF system with a base frequency of 1 GHz. The MO outputs include 3 GHz for the vector modulator to drive the klystron, 83 MHz towards the laser oscillator and 1 GHz to the timing module, which triggers the high voltage modulator, the LLRF, the laser amplifier and some diagnostics components. The reflected and forwarded RF signals from the cavities are mixed with a 3.025 GHz signal from the Local Oscillator (LO) box, then down-converted to an Intermediate Frequency (IF) of 25 MHz and finally digitized by an Analog to Digital Converter (ADC) unit with a sample frequency of 125 MHz. In the LLRF controller, the measured amplitude and phase values from the RF cavities

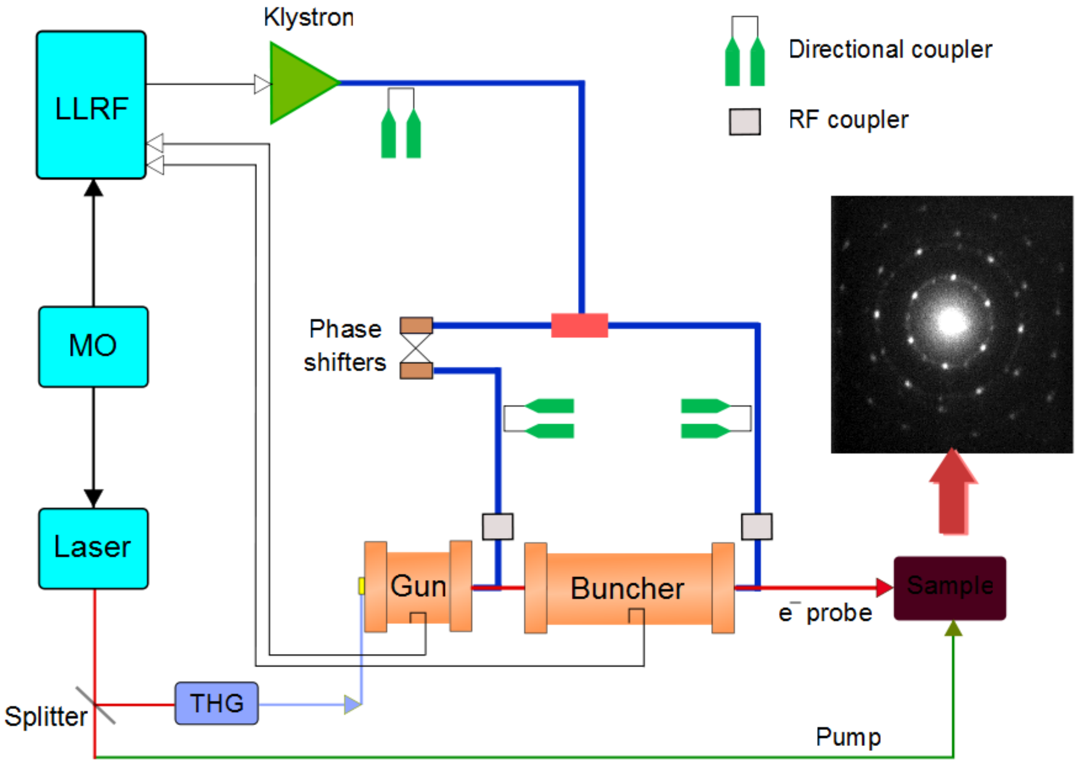

FIGURE 2.2: 3 GHz RF pulses generated by the master oscillator are amplified in the klystron, which is supplied by the high voltage modulator. The high power signal is divided in two arms, directed and coupled by power couplers to the buncher and gun cavities. By moving the phase shifter arms, the RF phase in the cavities can change independently. The third harmonic of the laser pulse, synchronous to the RF pulse, strikes the photocathode that leads to electron beam generation and diffraction as a result of colliding to a target material. The material undergoes an atomic evolution when another fraction of the laser beam pumps the sample. The varying diffraction patterns illustrate the dynamics of the material structure, caused by the excitation.

are compared to the set point values from the DOOCS server and digital feedforward signals are generated accordingly. A feedforward learning algorithm corrects the RF signal based on a comparison of measured and expected amplitude and phase in the gun cavity. The LLRF controller is triggered by the timing module with the repetition rate of the machine ($\leq$ 50 Hz) and the offset values are sampled with a the rate of 125 MHz to generate the corrected RF signals. Thereafter, they are converted into analog signals by a Digital to Analog Converter (DAC) unit and drive the klystron through the vector modulator. A fast feedback loop for corrections within an RF pulse of 6 μs length is in preparation. A layout of REGAE's LLRF system is shown in Fig. 2.3.

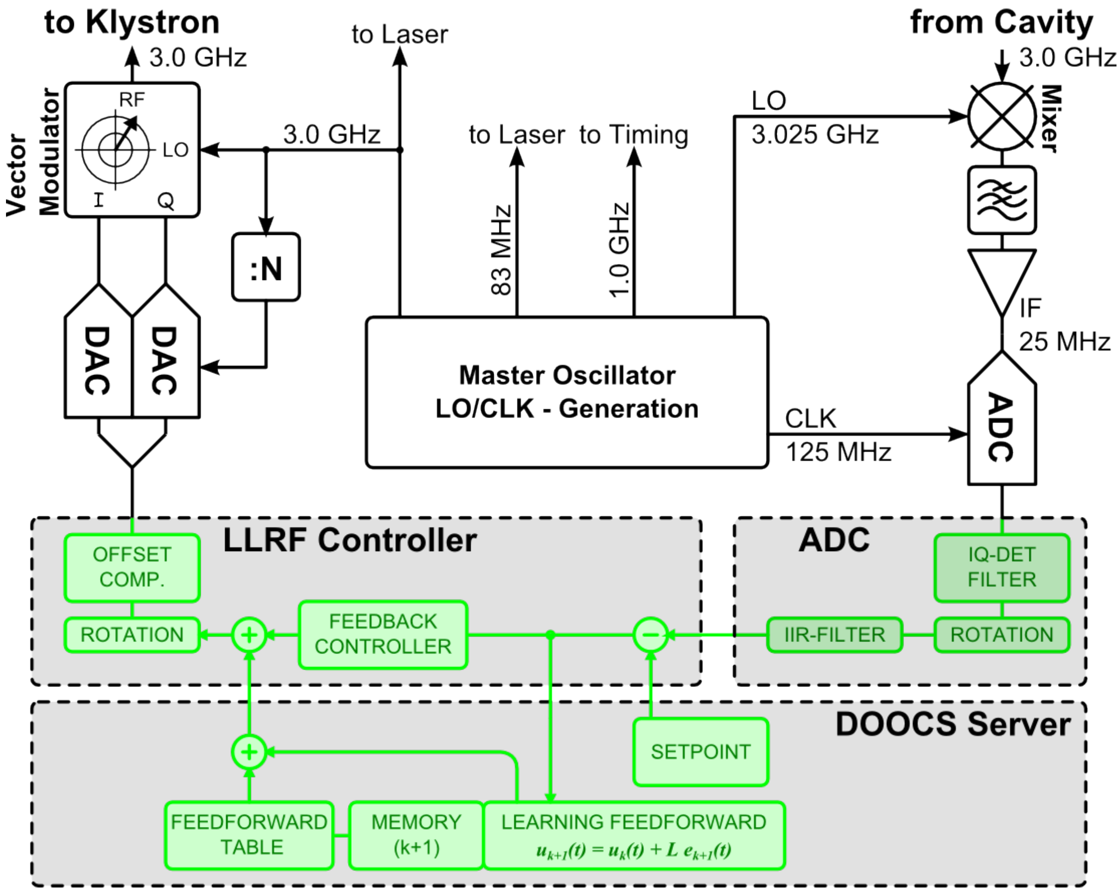

Figure 2.3: Layout of the REGAE LLRF system. Courtesy of M. Hoffmann.

2.2 Laser system

As one on the most important sub-systems at REGAE, a Ti:Sapphire laser provides photon pulses, which are coupled into the photo-cathode gun. These pulses result in generation of photo-electrons that are arranged in bunches. They also exert evolutionary changes in the target specimen, once the pump-probe experiment takes place. The Ti:Sapphire laser is a commercial Coherent Elite Duo system [29] that generates femtosecond pulses with a center wavelength of 790 nm, 8 mJ per pulse, and 40 fs at 1 kHz. It consists of an oscillator (Micra-5) and a laser amplifier (Legend Elite Duo) for boosting the output power [30]. The laser amplifier and oscillator specifications are summarized in table 2.2. A high-energy ultra-short pulse is achieved within the amplifier when the Chirped Pulse Amplification (CPA) [31] method is applied on the seed pulse.

In order to fulfill the photoemission process condition, the characteristic energy of the photons that is absorbed by the electrons on the cathode atoms, should be high enough to overcome the work function of the material, so that the electrons are ejected from the photocathode. UV light of 266 nm is created from a part of the laser beam as a result of Third Harmonic Generation (THG) through two Barium borate (BBO) crystals. The UV excitation pulses illuminate the cathode surface and initiate the electron bunches. The existing photocathodes at REGAE and their characteristic work functions are listed in table 2.3. To acquire the desired parameters of the electron bunches, a proper care

Table 2.2: Laser amplifier and oscillator characteristics.

	Oscillator	**Amplifier**
Repetition rate	83 MHz	1 KHz
Central wavelength	790 nm	800 nm
Pulse duration	10 fs	40 fs
Energy per pulse	4 nJ	8 mJ

of the laser beam quality at the RF photocathode is of importance. The laser beam properties and its influence on the electron beam quality have been studied via ASTRA simulations and are briefly described [30].

Spatial profile and intensity distribution of the laser beam: The laser beam size and spatial distribution plays an important role in determining the transverse emittance of the beam that is dominated by the thermal emittance and space charge effects. The transverse emittance is better for smaller laser beam diameter. The simulation results show that, the flat-top intensity distribution, in both longitudinal and transversal dimensions, results in lower transverse emittance and consequently higher coherence length of the electron beam compared to the Gaussian distribution.

Laser pulse duration: The electron bunch duration and the emittance are proportional to the laser pulse length, respectively. An applied beam stretcher system to the laser pulse, provides flexibility in adjusting the bunch length from 100 fs to 1.5 ps FWHM.

Another branch of the laser beam, directed towards the sample, is generated through different nonlinear optical processes, such as the Second Harmonic generation (SHG) and the Non-collinear Optical Parametric Amplifier (NOPA).

Table 2.3: Work functions of the existing photocathodes at REGAE. All cathodes are located in a cathode box together with a scintillator cathode which is used for laser coupling and alignment onto the cathode area.

	Chemical formula	Work function (eV)
Molybdenum	Mo	4.6
Cesium Telluride	Cs_2Te	4.9
Gold	Au	5.1
Platinum	Pt	6.35

2.2.1 Laser synchronization

For the UED experiment, the laser and the RF should be synchronized within 10 fs through a synchronization setup. The laser oscillator is supplied by the MO with a frequency of 83 MHz. A small fraction of the signal power from the laser oscillator goes to the synchronization loop and the rest goes to the laser amplifier. The 36th harmonic of the oscillator repetition rate, 3 GHz, is obtained from a photo diode spectrum with a band pass filter. The signal is later amplified and then mixed with another signal from the local oscillator, which is locked to the MO. The two signals are down converted and sampled through an ADC unit with a rate of 125 MHz and sent to an FPGA unit. In the FPGA control, the offset of the phases is calculated and converted to an analog signal. It acts on a driver to drive a piezo element inside the laser cavity. A comprehensive description can be found in [28].

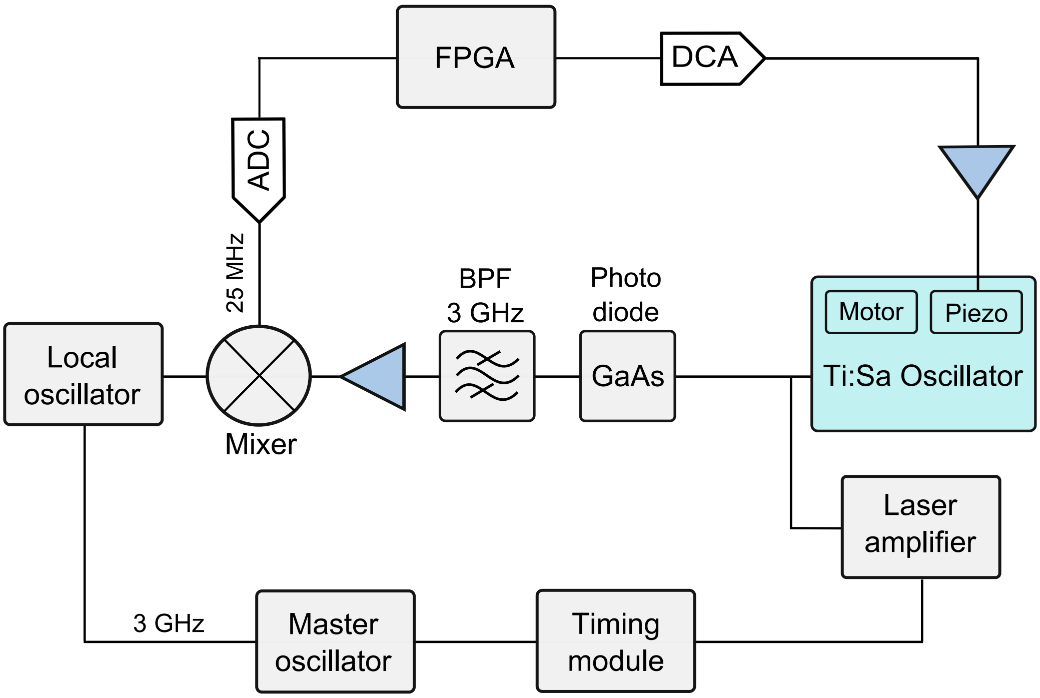

Figure 2.4: Layout of the REGAE synchronization system.

2.3 Magnets

2.3.1 Solenoid

Three double and one single solenoid are the installed focusing magnetic lenses. A coil of current with multiple turns produces a cylindrical symmetric magnetic field. The longitudinal component of the magnetic field focuses the traversing charged particles. Figure 2.5 shows the solenoid magnetic field of the REGAE solenoids as a function of the axial position, whereby the peak field is calculated as $(2.3\ I + 0.3)$ mT. I is the solenoid current. The focusing strength of the solenoids is given by:

$$\frac{1}{f} = (\frac{e}{2\gamma m v_z})^2 \int B_z^2 dz, \tag{2.3}$$

where the peak fields are given as,

$$B_{max} = (21.2I + 0.3), \quad B_{min} = (-21.1I - 0.2). \tag{2.4}$$

It can be deduced that the focusing distance is proportional to the square of the longitudinal momentum of the beam. The solenoids have a weaker influence as the energy of the beam increases. In addition to the focusing, a rotation is introduced to the outgoing beam, which is proportional to the integral of the field strength, B_z, and inversely proportional to the square of the beam's longitudinal momentum. However, for the double solenoids, since the field strength changes symmetrically around the longitudinal axis, the resulting rotation is zero.

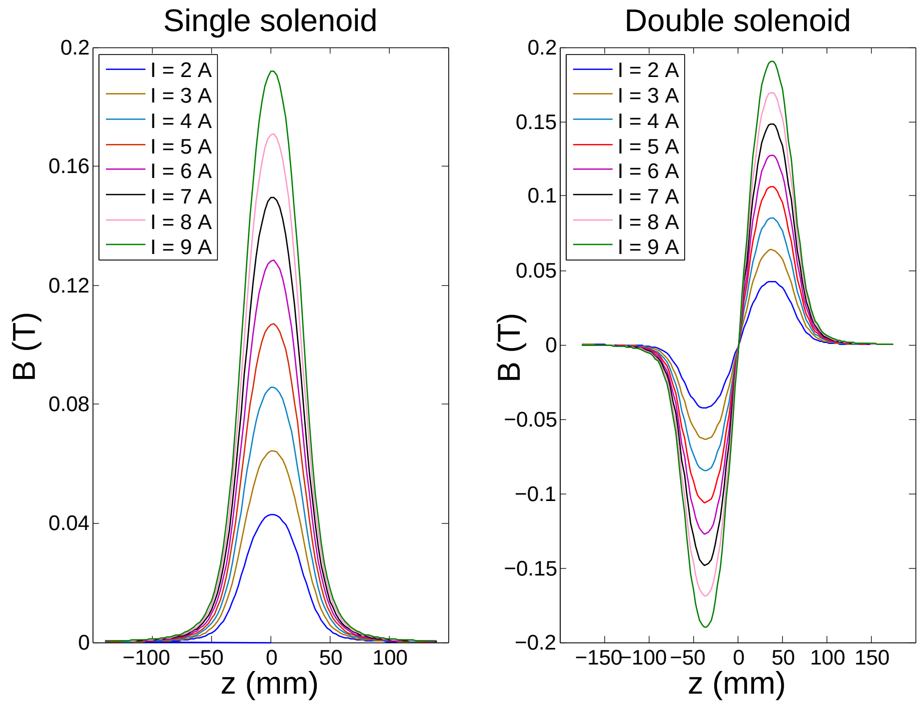

Figure 2.5: Magnetic field strength along the solenoid axis for the single solenoid (left) and the double solenoid (right).

2.3.2 Steerer

There are four positions along the REGAE beam line where steerer pairs are installed. They change and modify the electron trajectory and align it to the mechanical axis of the beam line. The air coil magnets are based on printed circuit boards, on which layers of copper are etched in a rectangular spiral pattern. The component of the current along the direction of the beam induces a magnetic field, which affects the electrons in the transverse plane. Two boards that are bent into a cylindrical shape form a dipole. At each location, two pairs of boards are placed orthogonally to each other, in order to introduce field induced kicks onto the electrons in horizontal and vertical direction. A complete description of the steerer magnets can be found in. [32].

2.3.3 Magnetic dipole

A dispersive arm is installed for energy and energy spread measurement at REGAE. The magnet is a horizontal dipole, which enforces a vertical and uniform magnetic field on the charged particles. It deflects the electron beam 90 degrees to a screen monitor that is centered at 540 mm distance from the beam line (in horizontal direction). The imposed magnetic field and centripetal force on the relativistic particles are related as shown in Eq. 2.5. A variation of the particle's energy leads to a change in the electron path length or a horizontal shift in the position of the outgoing beam.

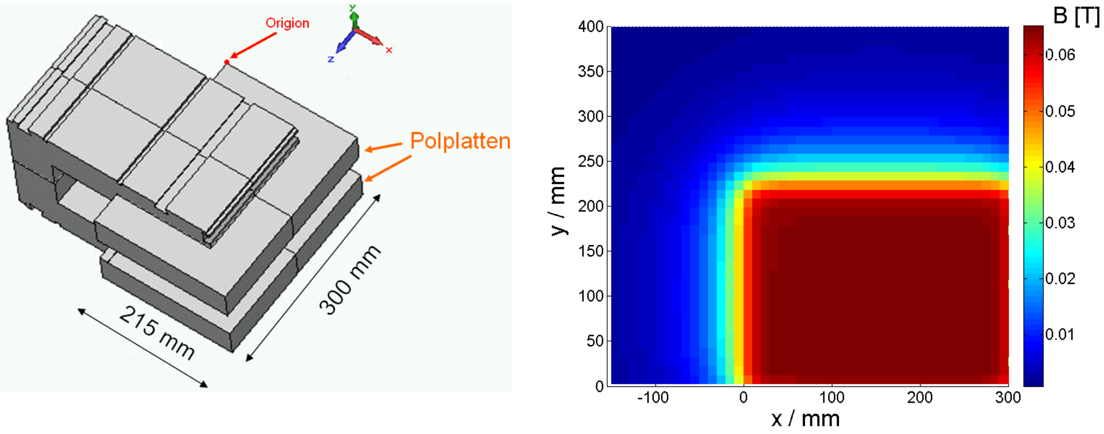

FIGURE 2.6: The dipole spectrometer magnet which is based on a horizontal HERA corrector magnet (left) and its field map (right). Courtesy of H. Delsim-Hashemi.

$$m\gamma v^2/r = evB_y. \tag{2.5}$$

The momentum of the electron beam is measured from the current of the dipole (I),

$$p\ [MeV/c] = 4.3I\ [A] + 0.054. \tag{2.6}$$

Figure 2.7 shows how the total energy, the kinetic energy and the momentum vary as a function of the magnet current.

2.3.4 Compensation coil

The electrons in the beam line are influenced by external magnetic fields such as DC and AC fields. At REGAE, among other DC fields, the earth magnetic field, has the most significant contribution to the external field formation. Since REGAE is installed in north-south direction, the main component of the field has no effect on the beam. In the

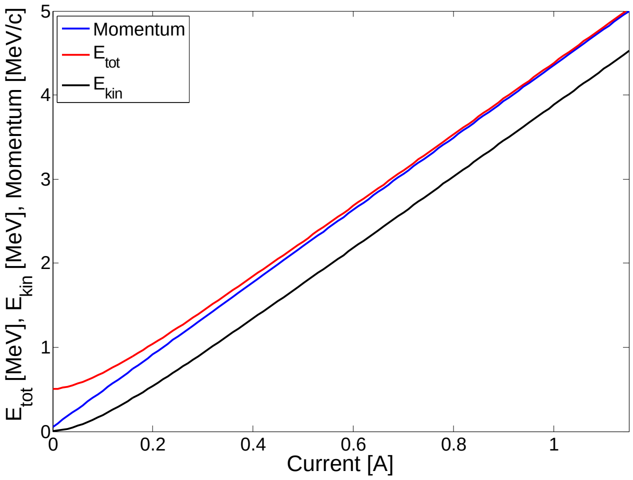

Figure 2.7: Total energy, kinetic energy and momentum versus current.

vertical plane, B_y influences the electrons significantly, in a way that it causes a deflection of 1 mm/m in the horizontal direction for an energy of 5 MeV. In order to compensate for the earth's magnetic field, a long pair of magnetic coils has been designed and mounted symmetrically around the beam line (see Fig. 2.8). The optimized compensation of the vertical field is fulfilled once the current of the coils is set to -9.75 A. At this optimal value of the current, B_y (z=6.5 m) = 0 and $|B_y(\text{z=9 m})| < 0.2\ \mu$T along the beam line [33].

2.4 Diagnostics

Currently at REGAE the diagnostics cover beam transverse profile, charge, energy, energy spread and emittance measurements. There are three diagnostics stations in the accelerator section. The first two stations are the so called Double Diagnostics Crosses (DDC1 and DDC2), but only one cross of each station is dedicated to the beam diagnostics. Two Faraday cups at DDC1 and DDC2, together with a current monitor (DaMon) are located close to DDC2 and perform charge measurements. The transverse beam profile is measured by means of scintillator-based profile monitors, located at DDC1, DDC2 and DC3. The scintillator screens are rotated by 45 degree with respect to the beam line. The second crosses of the above mentioned stations are occupied by dark current collimators to remove the dark current contribution traveling with the beam along its path [34]. The third station, located downstream to the side, includes a single cross (DC3) and it is allocated to measure the beam energy and energy spread, when the spectrometer dipole disperses the electron beam towards a scintillator crystal, positioned at DC3. A Faraday cup behind DC3, is used to monitor the beam charge after being dispersed. The transverse profile monitors are extended by a fourth station in the target chamber to optimize the beam condition for the diffraction experiment. For the layout see Fig. 2.9. Since the transversal diagnostics is the main topic of this thesis,

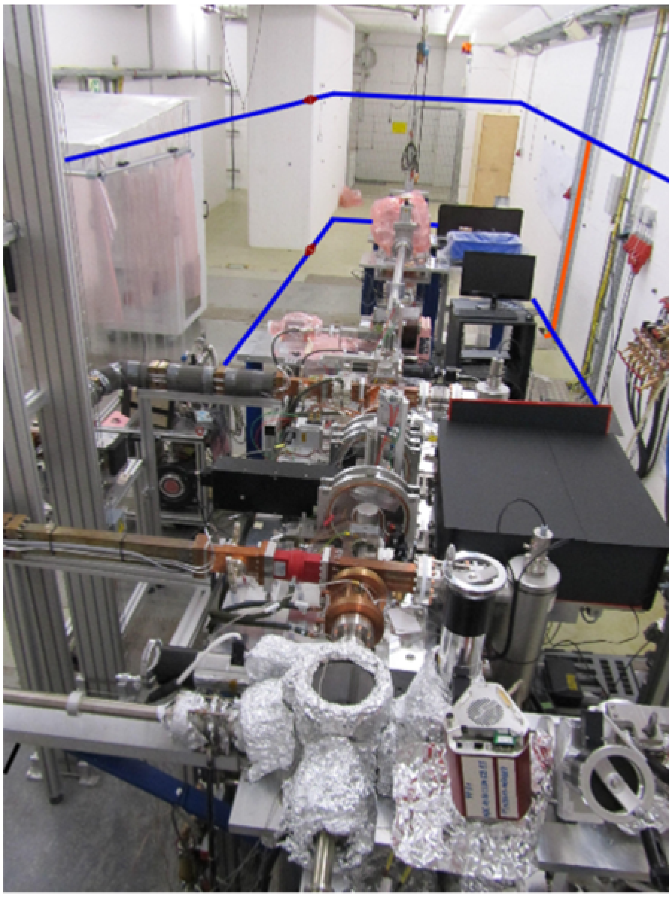

FIGURE 2.8: The pair of compensation coils are depicted in blue. The width and length of each coil are 3.3 m and 14.6 m, respectively.

in the subsequent chapters chief concerns for diagnostics, challenges, specific approaches and eventually the results will be discussed in detail.

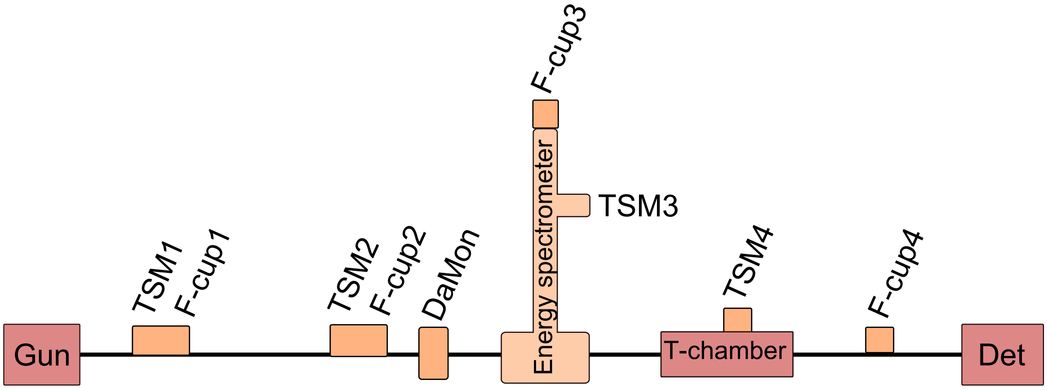

FIGURE 2.9: An overview of the machine, emphasizing on the diagnostics, which includes transverse screen monitors (TSM), charge monitors (DaMon and Faraday cups) and energy spectrometer.

2.5 Target chamber

The target chamber is the starting point of the experiment, where the diffracted electrons from the target material encompass valuable information on the atomic structure of the material. The main element inside the chamber is a sample holder and it comprises of different samples. So far, all the samples used at REGAE are inorganic samples (Si, MoS_2), due to the strong diffraction pattern that such crystals can provide. The sample holder is driven by a commercial manipulator (VAB: PM12-150) with traveling range of $\Delta X = 10$ mm, $\Delta Y = 10$ mm and $\Delta Z = 150$ mm. It incorporates a cold finger to provide cooling and heating capabilities for certain experiments. According to the requirements of different experiments, various versions of the sample holder have been installed inside the chamber, so far. An example of the sample holder is depicted in Fig. 2.10.

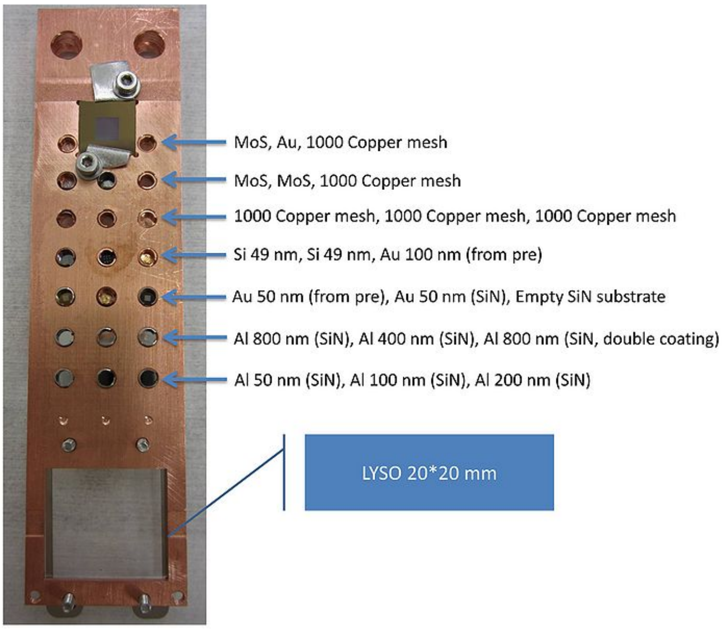

FIGURE 2.10: Sketch of an installed sample holder at REGAE. The holes in the upper part of the sample holder are filled with different target materials. The large hole at the lower part is occupied by a scintillator crystal that is viewed by a transverse profile monitor.

2.6 Electron diffraction detector

REGAE relies on indirect electron detection i.e. the electrons are converted into visible photons through a scintillator material. A Fiber Optic Scintillator (FOS), consisting of a scintillator material, CsI(Tl) in front of a fiber optic plate, forms the converter element. The FOS plate is placed perpendicular to the beam. A silicon wafer with an aluminum coating of 30 nm, with a 45 degrees tilt, reflects the light to the direction of the coupling optics and a detector. The energetic primary and secondary electrons and photons that are generated as a result of the interaction of electrons with the scintillator material, cannot reach the optics and the detector, because they are transmitted through the silicon wafer (see Fig. 2.11).

The REGAE detector is an EMCCD (Electron Multiplying CCD) type from ANDOR, iXon3-888 (DU888-DC-BV). It fulfills the requirements concerning the sensitivity and dynamic range of the detection and has been shown to be capable of single electron detection [35].

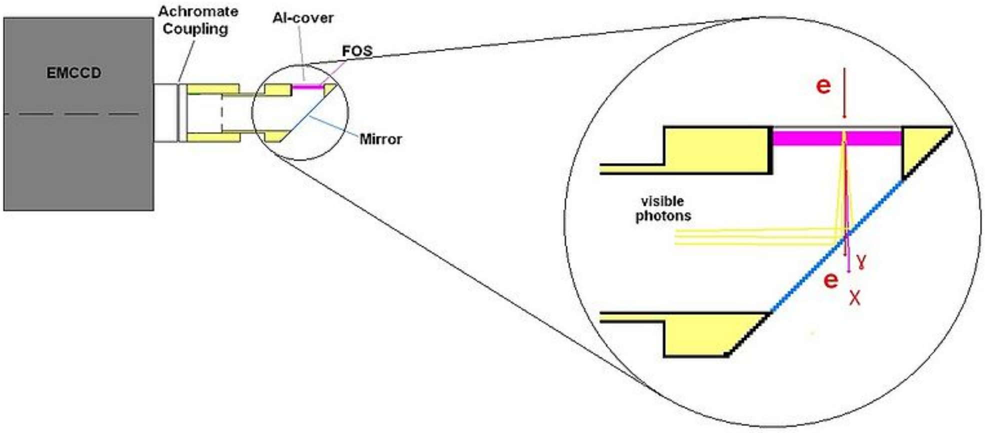

FIGURE 2.11: Electron diffraction detector with EMCCD and achromatic coupling lens (left). The zoomed area on the right side indicates the direction of the electron beam as it traverses the FOS. The generated visible light is collected and reflected by the mirror to the collecting optics and then imaged onto the detector. Courtesy of H. Delsim-Hashemi.

2.7 Machine preparation and operation

In order to attain favorable beam parameters and perform the envisaged experiments at REGAE, a good preparation of the accelerator is of importance. A brief description of the machine operation and the challenges are discussed in this section. A layout of REGAE, including all the elements, is illustrated in Fig. 2.12.

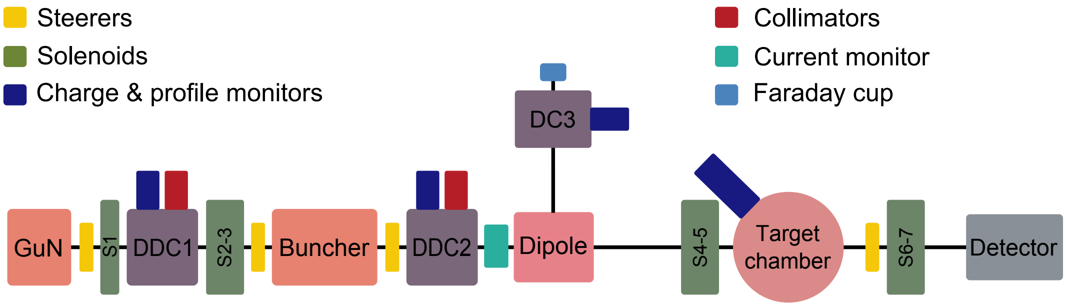

FIGURE 2.12: The beam line at REGAE. The beam proceeds from the gun section towards the experimental section. Distances between the elements are not to scale.

The RF power is coupled to the REGAE cavities with the repetition rate of the machine of maximum 50 Hz. Figure 2.13 shows the cavity voltage after being filled with the RF field. With the synchronization setup into operation, the arriving UV-laser beam coincides with the RF field within the time window of 6 μs. The most suitable position of the laser beam within the RF pulse is the plateau of the signal, where a uniform electric field is applied to the photoelectrons. On the one hand, the steady plateau is attained when the RF pulse is long enough, on the other hand, it should not be too long to avoid a drastic raise in the dark current intensity. The laser pulse delay time and the RF gate length are both adjusted through a timing panel that controls the timing module unit, fed by the master oscillator. Simultaneously, the Faraday cup and screen monitor at DDC1 can be used to find the position of the laser beam within the RF pulse.

Once the timing relation between the RF and the laser is optimized, the phase relation should also be investigated. A phase scan is performed by measuring the charge with a charge monitor and plotting it as a function of the RF phase. All the charge monitors can be used for the scan, but in the case of Faraday cups, the beam should be focused by the solenoids to the monitor. The resulting plot represents the phases, where the emission starts and terminates, also the operating phase is deducible (see Fig. 2.14). The maximum achievable gradient at the cathode is 110 MV/m. The energy of the beam, E [MeV], relates to the RF gradient, V [MV/m], as $E = 0.047\ V - 0.103$. This relation is obtained from a linear fit of the simulated data in ASTRA.

Under ideal conditions, the gun cavity is supposed to accelerate the electrons at the zero phase and the buncher cavity only to compress the beam without any acceleration at 90 degrees. The zero phase for the cavities are the points in the emission phase where the maximum energy is gained by the electrons. The energy is measured by the spectrometer while the klystron phase changes. Since the klystron drives both cavities, the buncher is detuned for measurements of the RF gun alone. Investigations show that the maximum energy is obtained at 40 degrees from the phase where the emission starts. With the buncher in use, in order to find the maximum bunching phase, the same study should be performed. The goal is to find a phase difference between the gun and the buncher such that both the acceleration in the gun and the bunching in the buncher reaches the maximum values. For this reason, a scan of the energy gain as a function of the phase difference is required. To alter the buncher phase with respect to the gun phase, the phase shifter is used. However, it changes the phases and amplitudes of the cavities. Thus, for each scan point, the amplitude and phase of the gun is redistributed to remain constant. A further correction is required due to the variation of the buncher's amplitude. It depends on the gun amplitude and phase. Based on the most recent measurements, the maximum energy is reached for a phase difference of -197 degrees from which the bunching phase deviates by 90 degrees. The derived value corresponds to the phase shifter position of 39.5 mm [27].

The experiment is proceeded after all the required optimizations in the accelerator are carried out. Using solenoid 1 and solenoid 2-3, one can create a fairly collimated beam at the sample plane with a reasonably large size that encloses each sample. The diffracted electrons are transmitted to the back focal plane of the objective lens, solenoid 6-7, where the scintillator screen is located. A diffractive pattern is subsequently imaged. There is also a pair of steerers after the target chamber, which aligns the diffraction pattern onto the detector plane. In order to achieve a dynamic diffraction with femtosecond resolution, a laser pulse pumps the sample material to exert the changes that are going to be probed by the electron beam. Beforehand, the temporal and spatial overlap between the electron and laser beam should be performed. The necessary spatial overlap is found by using a profile monitor at the target chamber, while the temporal match is feasible by moving a delay stage in the pump laser beam line.

The first time-resolved diffraction experiment was carried out and the dynamics of a melting process in a gold crystal sample was observed with a temporal resolution of 1.2 ps. Static diffraction using samples such as Gold, Silicon and Aluminum are also obtained and it is easily reproducible. The grid meshes, together with the samples in the upper part of the sample holder (see Fig. 2.10), can be imaged when the electrons are transmitted to the scintillator screen at the focal point of the objective lens. Shots of electron diffraction and real space imaging are illustrated in Fig. 2.15.

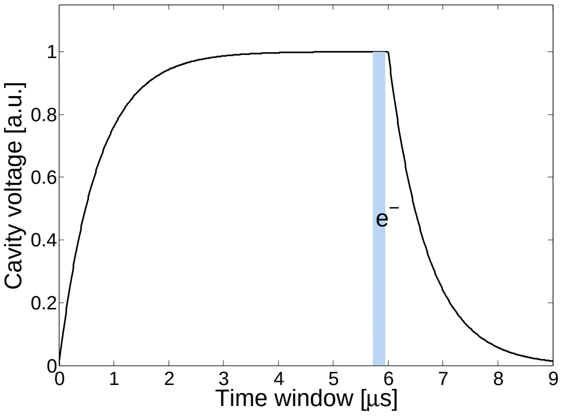

FIGURE 2.13: The RF field inside the cavities. The plateau region is the ideal position in time, where the laser beam can be placed, so that the photoelectrons are generated in a uniform field.

2.8 Other planned experiments

At the moment, REGAE's beam line is established mainly for the time-resolved electron diffraction experiment. Two other experiments are foreseen to be performed at REGAE, therefore, modifications and extensions in the beam line are required to be carried out accordingly.

2.8.1 Time resolved transmission electron microscopy

Real space imaging at high energy has some advantages over the conventional TEMs. Space charge effects degrades the quality of the electron bunch. It influences the temporal resolution of the dynamic TEM and the spatial resolution of the image by increasing the bunch length and introducing a momentum spread to the bunch. This effect is reduced at higher energies and lower charges. Beam dynamics simulations show that with a bunch charge of less than 20 fC and an energy of 3 MeV, the energy spread drops

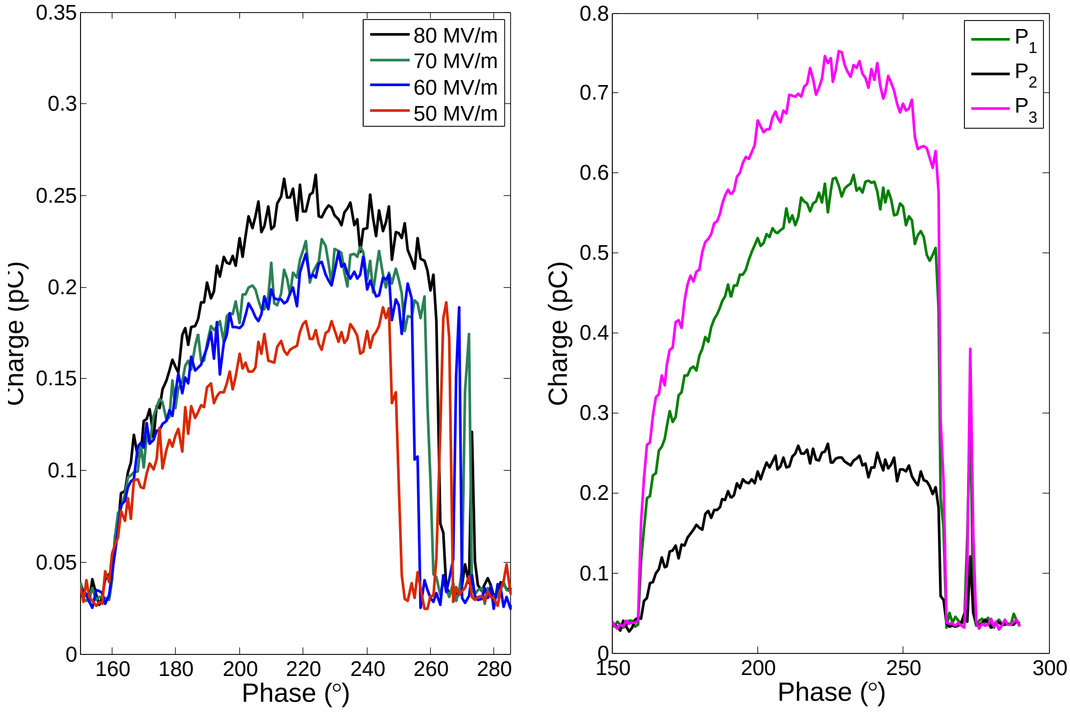

FIGURE 2.14: Left: phase scan for different field amplitudes when the laser power is constant. At higher gradients the gun phase range of the emission is more extended and also the amount of charge grows. Right: phase scan for different laser power levels ($P_3 > P_1 > P_2$) when the gradient is kept constant. For decreasing values of the power, the charge rises less steeply due to a suppression of space charge effects. P_2 corresponds to the case where space charge effects are negligible.

significantly and the conditions for a TEM experiment are met [36]. Theoretically, at REGAE's operating energies, the total stopping power in a tissue drops to about its minimal value. This translates to an optimal energy, where multiple and inelastic scatterings are significantly suppressed. Thus, samples of higher thickness can be used in high energy dynamic TEMs. For less than 10^5 electrons arranged in a bunch of 1 ps length, the peak current is high enough to gain a reasonable contrast of the image in a single shot. While a nanosecond resolution of dynamic TEM has been achieved [37], real space imaging of living cells, with temporal resolution of picoseconds to microseconds and spatial resolution of 1–10 nm, is of significant interest for dynamic transmission electron microscopy (TEM). In order to achieve such high resolution, a magnification of 10^4-10^5 is desired. A strong focusing will be applied to the electrons by a permanent magnetic solenoid as the condenser lens [38]. An identical lens, as an objective, focuses the beam on the object plane of an intermediate lens, which causes further magnification. Finally, a projector lens forms the image on the detector. The entire lens system has been designed in a way that the emittance growth remains small and the required magnification is accomplished. The permanent magnets will be placed inside the forthcoming version of the sample chamber which has been designed to suit both dynamic TEM and plasma experiments. Another detection system is considered for real space imaging and it will be installed downstream of the current detector, which is presently

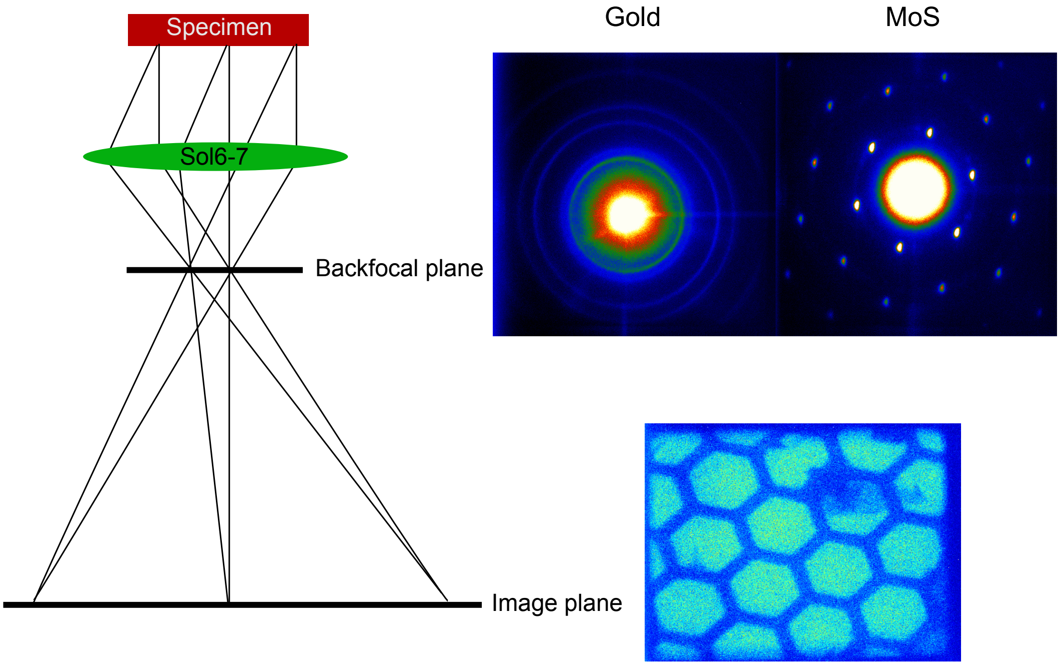

Figure 2.15: Schematic optics behind the specimen at REGAE. The diffraction pattern is formed in the back focal plane of the objective lens, which in this case is solenoid 6-7. Two examples of diffraction are shown, obtained with gold and MoS samples. At some distance from the back focal plane, the exposed area by the electron beam is imaged on the image plane. The picture on the bottom depicts part of the grid that holds the sample. A magnification of ~ 22 is estimated.

in use for the diffraction experiment.

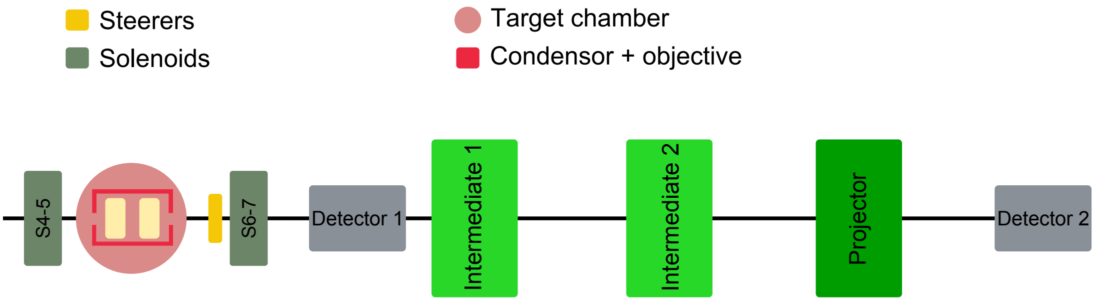

Figure 2.16: The REGAE beam line will be extended as illustrated. The extension and modifications consist of a new design for the target chamber, which is suitable for both TEM and plasma experiments, as well as of new magnets for real space imaging.

2.8.2 Laser Wakefield Acceleration (LWFA) probing

LAOLA, the Laboratory for Laser- and beam-driven plasma Acceleration is a collaboration between groups from DESY and the University of Hamburg. It carries out research in the relatively new field of plasma wakefield acceleration (PWA). REGAE is one of the sites that hosts a branch of the LAOLA experiments, which is entitled as 'external injection' [39]. The separation between electrons and ions in the laser-induced plasma cell, imposes a very strong accelerating field on the externally injected electrons of the order of 100 GV/m. The advantages of this accelerator type, compared to the conventional forth generation light sources, are the extremely high gradient and the compact size of the accelerator, of the order of millimeters. To better characterize this accelerating field, a well defined electron beam of 5 MeV probes a laser-induced plasma. While performing such pump-probe experiment, the external electron bunch and the driving laser should be synchronized within 10 fs to guarantee the stability of the acceleration and an optimal energy spread. The wakefield inside the plasma can be reconstructed by comparing the electron beam with known parameters, before it traverses the plasma cell, with the beam, which is characterized after the plasma accelerating cell. The bunch charge of 100 fC and length of less than 10 fs must be focused so that a transverse size of less than 3 μm is reached. The same permanent solenoid magnet that is employed as the condenser lens for TEM experiment, would provide the intense focusing to reduce the beam size. The high power (>1 TW) driver laser beam line will be constructed and coupled to the new target chamber. Additionally, an electron spectrometer will be installed downstream of the target chamber for the electron beam characterization.

Chapter 3

Characterization of scintillator crystals

Since the beam profile monitors at REGAE operate based on the conversion of the incident electrons to visible light on a scintillator, characterizing the material and the resulting emission is a first step towards evaluating the monitor system.

Scintillator is a material, which emits a pulse of light due to the conversion of deposited energy by an incident ionizing radiation to visible photons. Since the intensity of the generated light depends on the deposited energy, the measurement of the number of emitted photons from a well-characterized scintillator also determines the incident radiation energy. Scintillators are mainly classified as inorganic and organic. While organic scintillators (plastics, liquids) are composed of aromatic hydrocarbons and scintillate based on their molecular levels, inorganic scintillators are mostly made of halides and oxides and the scintillation is characterized mostly by the crystal structure. Inorganic scintillators are made of elements with large atomic number and they possess high densities, leading to a better efficiency of the interaction between matter and radiation. On the contrary, low density and low atomic number of organic compounds, make them in general less efficient in terms of intensity. Because of several desirable properties of inorganic scintillators, such as high stopping power, excellent quantum efficiency and energy resolution, their use is extended to a wide range of applications in a number of scientific fields like high energy physics and particle detectors, medical imaging, astrophysics and accelerator physics. In this chapter, the structural properties, scintillation mechanisms and emission properties of inorganic scintillators, as well as characteristics of the used scintillators at REGAE and the simulated results related to these materials are presented.

3.1 Scintillation process in inorganic scintillators

Luminescence centers in crystal structures are responsible for scintillation. These centers either have intrinsic origin or are created as wanted or unwanted impurities in the lattice structure. Accordingly, the crystals are classified as intrinsic or extrinsic scintillators. There is a third category in between these classes, which consists of the self-activated crystals or scintillators.

If the deposited energy is conveyed to the electrons in the valence band (the last occupied atomic level), such that it acquires an energy larger than the energy gap between the valence band and the conduction band (first empty state), the electron travels to the conduction band. Eventually, with the empty place in the valence band they create an electron-hole pair. In scintillator crystals, the band gap contains energy levels, which are indeed the intrinsic or extrinsic luminescent centers. The electron-hole pairs might enter these centers and cause the emission of light in the visible range [40]. The energy levels of the band gap should be contained in the forbidden energy band in order to avoid re-absorption of the emission [41].

Depending on the type of the ionizing radiation and its energy, the processes that are involved in energy absorption and subsequent scintillation are different.

In case of a traversing charged particle through a medium, ionization (or excitation) of atoms and bremsstrahlung are the most likely processes involved in the energy deposition. The particle interacts with the atoms by exciting or ionizing them. The collision stopping power, which is the average rate of energy loss per unit path length of a matter, is given by the Bethe formula for relativistic charged heavy particles [42] (see appendix A). However, the stopping power differs when the incident particle is an electron [42, 43] (see appendix A).

When the incident particle is scattered by the field of the atomic nuclei, an X-ray photon is radiated. The interaction with the atom is bremsstrahlung and the lost energy per unit path length is called radiative stopping power. The bremsstrahlung is the dominant process at energies of few tens of MeV.

In scintillator crystals, if the energy is deposited by collision, it results in scintillator emission. In other words, the higher the collision stopping power, the better the light output is. According to the Bethe formula, a high effective atomic number (Z_{eff}) of inorganic scintillators raises the collision stopping power and results in a higher amount of light (see appendix A). At the electron energy range of REGAE, 2–5 MeV, the dominant process is collision and the radiative stopping power has a small contribution relative to the collision stopping power. Figure 3.1 shows collision, radiative and total stopping power in LYSO and CsI crystals (existing scintillators at REGAE). The plots are produced by the ESTAR database, which calculates stopping powers and ranges for electrons [44].

The traversing electron, deposits a portion of its energy along its passage through the medium and this energy should be transferred to the luminescence centers to induce the emission of the scintillator. Due to the atomic excitation or ionization, holes are created in the valence or inner core band and electrons in the conduction band. These electron-hole pairs are called primary excitations. Subsequently, a large number of secondary excitations are produced as a result of inelastic electron-electron scattering and Auger processes. After this stage, electrons and holes are thermalized and their kinetic energy

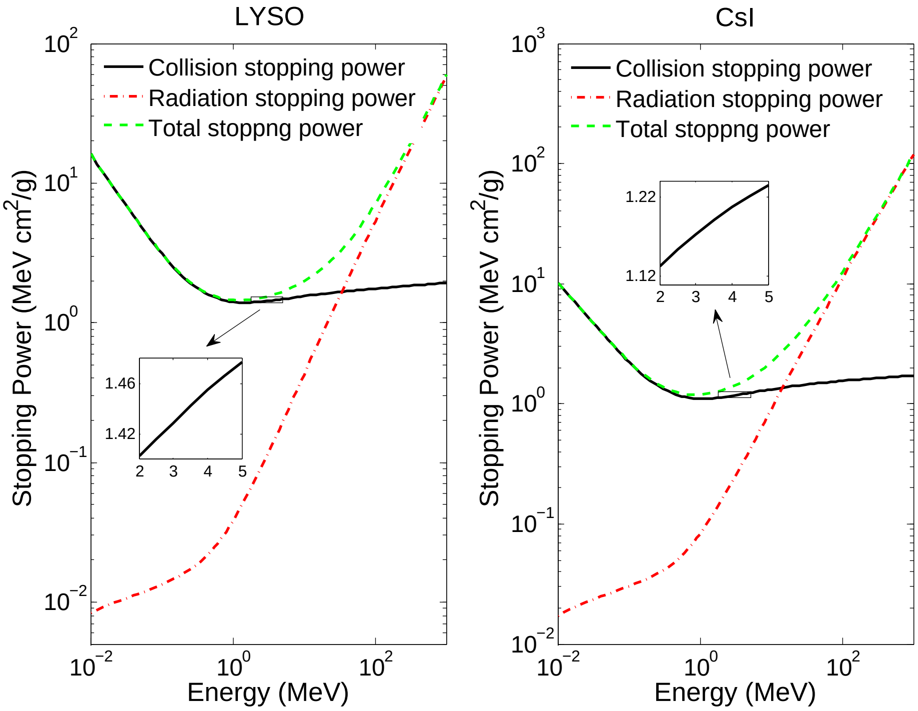

FIGURE 3.1: Collision, radiative and total stopping powers of electrons as a function of their energy in LYSO (left) and CsI (right) compounds.

is reduced. They transfer the energy to the luminescent centers and subsequently the excited centers get relaxed by radiating visible photons (see Fig. 3.2).

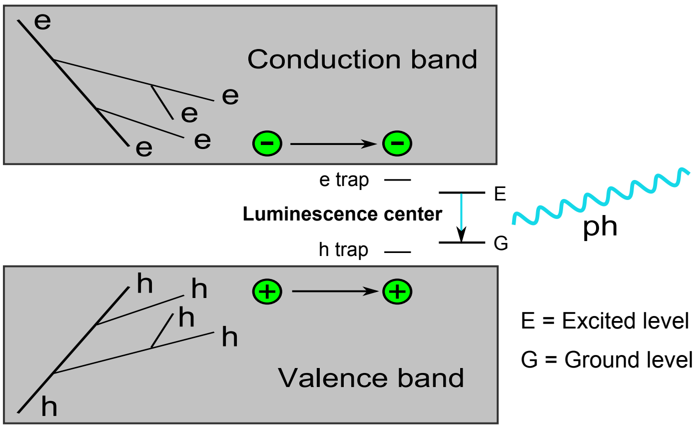

FIGURE 3.2: Schematic of the scintillation process.

3.2 Some general characteristics of scintillators

3.2.1 Light yield

The number of emitted photons per unit of the deposited energy in a scintillator medium is defined as the light yield. If the energy loss of the ionizing radiation is E_e, assuming that the electron-hole energy is equal to the band gap energy, the number of generated electron-hole pairs can be given as [40],

$$N_{eh} = \frac{E_e}{bE_g}, \tag{3.1}$$

E_g denotes the band gap energy and b is related to the crystal structure. Equation 3.1 shows that only a fraction of energy loss (scaled to $1/b$) by the radiation in the material can be converted into electron-hole pairs. However, the emitted light intensity can be reduced due to other reasons, such as:

- Thermal quenching: The non-radiative relaxation of the luminescent centers is called thermal quenching. In this case the centers are de-excited by emitting phonons. This effect is strongly temperature-dependent and the light yield degrades with increasing temperature of the environment. The quantum efficiency of the luminescent centers as a result of this effect can be denoted by L.
- Absorption: The scintillator bulk medium is not perfectly transparent to the emitted light. At some point, the existing impurities and defects, which are created during the crystal growth, can absorb the photons and reduce the light yield. T shows the transmission efficiency of the bulk medium.

If the conversion efficiency is defined as the product of the luminescent efficiency (L) and the transmission efficiency (T), The number of generated scintillation photons are given as,

$$N_{ph} = \frac{E_e}{bE_g}.LT \qquad 0 < L, T < 1. \tag{3.2}$$

3.2.2 Decay time

The decay time of a scintillator is the time interval between excitation of a luminescent center and $1/e$ of the radiation intensity from this center. If only one type of luminescent center exists, the emission profile is exponential and it ends after multiples of the decay time. In reality, scintillators contain more than one luminescent center type and the total decay time is a superposition of all decay constants. The rise time of the scintillator is also defined as the time, which it takes for the deposited energy to be transferred to the luminescent centers and to excite them. The decay time from a luminescent center, comprises of the radiative and non-radiative rate of emissions from the scintillator. The latter is characterized by a much faster time constant, in contrast to the desired radiative constant. Hence, although non-radiative emission contributes to a lower light yield, it can shorten the decay constant of the scintillator [40]. However, the radiative decay time is limited to [45],

$$\tau = 1.5 \times 10^{-5} \frac{9\lambda^2}{f\left(n^2+2\right)^2 n}, \tag{3.3}$$

where f is the oscillator strength of the transition from the initial to the final state, λ the wavelength of the transition in nanometers and n the refractive index. The quadratic dependence of the decay time on the emission wavelength is responsible for the fast decay component of those scintillators emitting in the blue and near UV region. Ce-doped scintillators are in this category and they are classified as rapid scintillators [41], i.e LYSO(Ce).

In addition to the fast scintillation, many scintillators show a very slow luminescence. Phosphorescence is the main reason of such emission and the amplitude of phosphorescence at a fix point of time after irradiation is defined as the afterglow. The time constant assigned to this process can vary from several microseconds to several hours. The phosphorescence behavior of LYSO:Ce scintillator will be described in this chapter.

3.3 Selected scintillator crystals at REGAE

A good scintillator is characterized by its outstanding light yield, fast emission response, high density, excellent energy resolution and high light transmission within its emission spectrum. However, finding a scintillator that possesses all theses properties is not feasible and therefore, depending on the case of study the definition of a good scintillator differs and a proper material is the one that suits best to the experimental conditions.

3.3.1 LYSO:Ce

Cerium-doped Lutetium Yttrium Orthosilicate ($Lu_{2-x}Y_xSiO_5$) is an ideal generation of scintillators. Because of its crystal structure, high density and large atomic number, it is characterized as a scintillator with extremely good light yield. In addition, the emission is released within a very short time scale and self-absorption of the emitted visible light is negligible. Therefore, this scintillator material is known as a proper candidate for various applications in nuclear physics, medical imaging, high energy physics, etc.

The successful growth of single crystal LYSO was demonstrated in 2000 [46]. It was introduced as an attractive alternative to cerium doped oxyorthosillicate (LSO), which was discovered in 1992 [47] and had a number of remarkable advantages over the existing scintillators. Besides retaining the optical and physical properties of LSO, ease and cost of LYSO growth due to a lower melting point (2100 °C), makes it a proper alternative to LSO. Apart from that, LYSO improves the poor uniformity of the LSO light yield to some extent. In addition to the higher light yield, it performs better with respect to a serious problem of LSO that is the large variation of the light yield from crystal boule to crystal boule and even from top to bottom within the same crystal boule [48].

Nevertheless, the mentioned inhomogeneity in light yield still remains as a characteristic feature of LYSO.

LYSO has two activator centers and one of them is dominant in the scintillation process at room temperature. The peak of the emission occurs at around 430 nm, while the peak of the photo-excitation spectrum is at about 360 nm [49]. LYSO is considered as a fast scintillator with a reported decay time better than 50 ns [46, 50]. To this, we should add the afterglow of the scintillator, which is released in relatively much longer time (see 3.5). It shows a very high light yield (LY) of $\sim$ (25000–30000) ph/MeV [46]. It possesses a high density and a large atomic number of ρ = (7.1–7.4) g/cm^3 and Z_{eff}=66, respectively, which causes an increase in stopping power and ionization loss in the material and consequently a higher scintillation intensity. This crystal is highly transparent to the emitted light and a good transparency occurs above the theoretical limit, at a wavelength of 400 nm [40]. Because of the excellent radiation hardness of LYSO, it is a good material to be used in a severe radiation environment [51].

For the purpose of electron beam diagnostics at REGAE, LYSO screens are employed. They offer high light output, which makes them suitable for low-charge diagnostics. Additionally, one can take advantage of their fast scintillation process to suppress the high-gradient induced dark current, when the detection window is shortened as much as the characteristic decay time of the scintillator. The currently installed LYSO pieces were purchased from Omega Piezo technologies Inc [52], with customized dimensions of (20×20×0.3) mm^3. The experience of using this scintillator material for challenging low-charge single shot diagnostics has been satisfactory so far.

3.3.2 CsI:Tl

Tallium doped cesium iodide (CsI:Tl) is classified as a high light yield scintillator. Nevertheless, due to the relative low density and the effective atomic number of this material the ionizing stopping power is relatively low. The very long decay constant can be considered as the main disadvantage of CsI(Tl) and this can limit the applicability of this material. The physical properties such as, photon yield, atomic number, density and decay time, associated with this scintillator, are LY = 52000 ph/MeV, Z_{eff} =54, ρ =4.51 g/cm^3 and τ=1 μs, respectively [53]. In addition, the peak of its emission occurs at 560 nm, i.e. with respect to the emission of LYSO it is shifted to longer wavelengths. The normal visible CCD sensors show a better efficiency at such wavelengths. Cesium iodide also has a useful property, when grown in thin layers and on specially prepared substrates by the vacuum-evaporation technique. There is a gap between the columns, which is filled with reflective coating to minimize the loss or cross talk between the columns [54]. The columns of the scintillator work as light guides and limit the passage of the light within the micro-pillar structure. While in a single crystal the emitted light is highly diffused, with a prismatic activated CsI, the light is conducted along the columns. Consequently, there is a gain in the light output and resolution. Apart from a well-efficient optical transmission and high detection efficiency, the columnar scintillator provides an excellent spatial resolution. With the aim of efficiently converting x-rays to visible light to be detected by a solid-state imaging device, Hamamatsu has developed a fiber optic plate with columnar CsI(Tl), which is called FOS [55]. It consists of a supporting base of a fiber optic plate (FOP), on which the scintillator material is directly deposited by the aforementioned vacuum evaporation method. The columns are grown perpendicular to the FOP as the extension of each individual fiber rod. The scintillated photons are emitted in the scintillator column and guided first by the scintillator and further by the individual fiber core. Since CsI(Tl) is slightly hygroscopic, a protection film is required to avoid mechanical damage and makes it resistance to moisture [55].

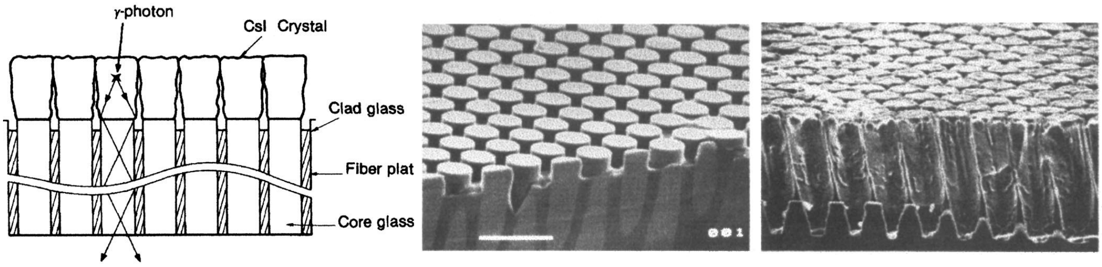

Figure 3.3: Schematic of an FOS (left). Columns of the luminescence material are formed as the extension of fiber columns with almost equal cross sections. Microscopic image of FOP (middle) and FOS (right) [56, 57].

At REGAE, an FOS is used in the diffraction detection system. The diffracted electrons hitting the luminescence CsI(Tl) generate optical light. Due to the high light yield of the scintillator and significant optical transmission through the fibers, the FOS can provide a bright source of light. Since the diffused component of the light is eliminated at the very early stage inside the scintillator, the FOS out coming source is collimated to some extent. Additionally, the pillar structure of the FOS improves the resolution of the imaging. If the optics is optimized for a decent resolution and collection efficiency, the entire detection system can reach a great performance. It has been demonstrated that the REGAE detection system has reached the sensitivity of single electron detection [35]. Recently, the application of the FOS at REGAE has been extended to electron beam diagnostics as well. In the DC3 station, two pieces of FOS, one commercialized as high resolution (HR) and the other as high light output (HL), as well as a piece of single crystal LYSO are installed. Besides beam energy and energy measurement, the objective is to compare the performance of the three different structures in terms of resolution and intensity of the beam profile.

The currently mounted FOSs at REGAE are rectangular-shaped. The physical surface is (18×18) mm^2 and the effective area which is deposited by the CsI(Tl) is (15×15) mm^2. The fibers' diameter is 6 μm and millions of them are bundled parallel to each other to form the FOP. The CsI layer and the FOP thicknesses are 0.15 mm and 3 mm, respectively.

As a standard X-ray detection device, the glass type and FOP thickness of the FOS have been optimized such that the X-ray absorption coefficient is maximal to avoid direct strike of the X-ray photons with the solid state detector sensor. In the case of REGAE, an indirect electron detection is dealt with. A mirror reflects the optical photons towards the detector and separate them from the secondary electrons, which are transmitted through.

3.4 Simulations of the scintillators

In order to develop a better understanding of the scintillation process, evaluate the performance of the detection system and optimize the related experimental parameters, such as the detection resolution or the collection efficiency, Geant4 [58] can be used to simulate the relevant configurations. Geant4 is a toolkit for simulating the passage of particles through matter, in which all aspects of the simulation process have been included: the geometry of the system, the materials involved, the fundamental particles of interest, the generation of primary particles of events, the tracking of particles through materials and external electromagnetic fields, the physics processes governing particle interactions, the response of sensitive detector components, the generation of event data, the storage of events and tracks, the visualization of the detector and particle trajectories [58]. Geant4 is written in C++ and exploits advanced software-engineering techniques and object-oriented technology. The shape and the geometry of all the components of the setup and the related materials, as well as the sensitive elements that record each individual hit to simulate the detector, can be defined. Tracking in Geant4 contains various classes for tracks and steps, using different processes, which describe the physics interaction models. From an impinging charged particle on a medium filled with a specific material, the optical processes that can lead to photon generation are scintillation, Cerenkov and transition radiation. Those main processes that can be involved in transportation of optical photons inside the medium are reflection and refraction at medium boundaries, bulk absorption and Rayleigh scattering. The optical properties of the medium, which are key to the implementation of these types of process are stored as entries in a properties table linked to the material. They can be expressed as a function of the photon's wavelength. The properties that should be assigned to a scintillator material are the emission spectrum, decay time and photon yield of the scintillator.

The process of scintillation in LYSO(Ce) and CsI(Tl) has been simulated by Geant4. Different geometries have been examined and all processes at optical wavelengths are included. Some optical properties of the scintillators, which are given to the class of material as input information are shown in Fig. 3.4.

3.4.1 Scintillation in single crystals, LYSO(Ce) and CsI(Tl)

The intensity of the emission and scintillator resolution can be investigated as a function of the material thickness, electron beam energy and specific geometries of the experiment.

In a simple geometry case, a rectangular scintillator screen is built as the interaction medium in the simulation. A sensitive detector is attached behind the screen, with an equal surface area. The area size is adjusted to $(20{\times}20)$ mm^2 and agrees with those of the REGAE LYSO screens. The optical photon events are collected by the sensitive medium and they convey most of the required information such as spatial, angular and energy distribution of the beam profile on the scintillator surface. The incoming particle is an electron, which strikes the scintillator medium in the center and perpendicular to it. The scintillator resolution is defined as spatial distribution of the scintillated photons

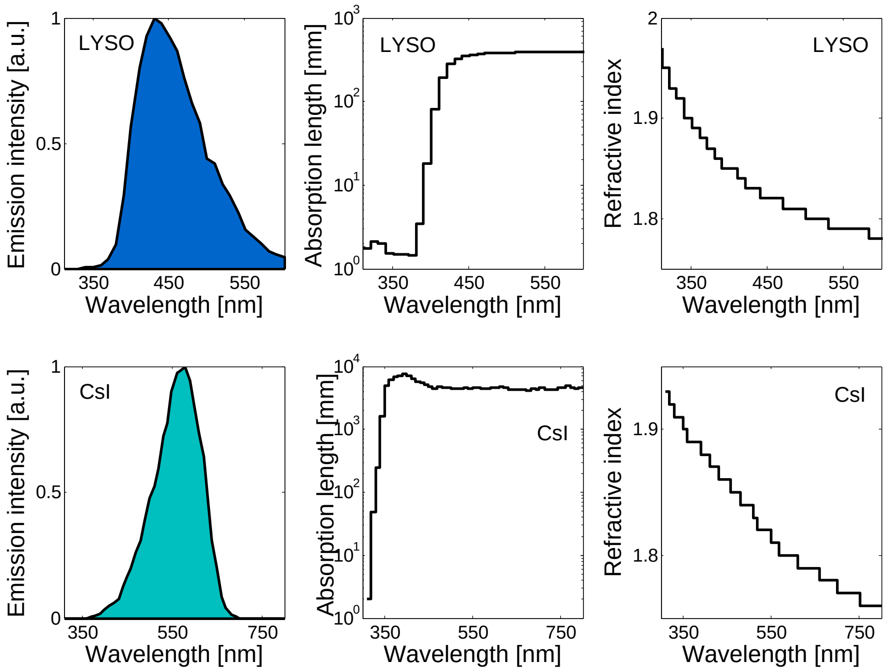

FIGURE 3.4: From left to right: the emission spectrum, absorption length and refractive index of two luminescent materials, LYSO(Ce) [40] and CsI(Tl) [59, 60] as a function of the photon wavelength.

on its back surface, as a result of hitting multiple electrons in the same point on the scintillator's front surface. In other words, the scintillator resolution is a measure of extension of a point electron source after the scintillation process. As a case of study, the luminescence process in LYSO and CsI are simulated, when the scintillator thickness varies in a range of 100 μm to 500 μm. The available LYSO crystals at REGAE have a thickness of 300 μm. Via this simulation, the relation of the scintillator resolution and the light output intensity with respect to the scintillator thickness has been studied. Figure 3.5 shows the scintillator response to the material thickness. The error bars on the light yield values are due to the statistical fluctuation of the number of generated photons within 1000 runs of a single electron impinging on the luminescent medium. For determining the resolution, the entire photon events related to all 1000 electron hits are accumulated, therefore the statistical error associated with the resolution is negligible. The RMS size of the photon emission on the scintillator surface is taken as the resolution. Changing the case of study, the effect of the electron energy variation on the scintillator resolution and light yield is investigated. The results are shown In Fig. 3.6.

According to the simulation results, the out coming intensity of the scintillator is proportional to the scintillator thickness. However, while a thick material desirably improves the intensity, the resolution is sacrificed. In the case of LYSO, the resolution starts to degrade after a thickness of 300 μm, while in CsI the resolution does not change that steeply. The geometrical spread of the photons, due to the scintillator thickness, is one of the reasons for the degradation of the resolution. When the energy of the electrons changes, the light yield is not affected significantly, because the electron stopping power within this range of energy does not alter a lot. However, the resolution improves as the the energy increases. The variation of the resolution in both simulation cases is explained by multiple scattering. As electrons traverse a medium, they are deflected due to the Coulomb scattering from the nuclei. The RMS scattering angle is given as [42]:

$$\theta_0 = \frac{13.6\ MeV}{\beta cp} z\sqrt{x/X_0}(1 + 0.038 \ln x/X_0), \tag{3.4}$$

βc, p and z are the velocity, momentum and charge number of the electron, x is the thickness of the material and X_0 is the radiation length. Since the LYSO crystal has higher stopping power compared to CsI, its radiation length should be shorter. The radiation length values assigned to LYSO(Ce) and CsI(Tl) are 1.1 cm and 2.43 cm, respectively. It can be noted that the scattering angle scales inversely to radiation length, and consequently, under the same conditions for both scintillators, the radiation from LYSO is more influenced by the multiple scattering process. Degradation of the resolution by the thickness and energy reduction is also explained in Eq. 3.4, where the scattering angle is linearly and inversely proportional to the particle momentum and medium thickness.

In Fig. 3.7, the collision stopping power, which results in scintillation, is proportional to the light yield and is calculated by using the ESTAR database. In this database, other quantities such as radiation and total stopping powers as a function of energy are calculated. The collision stopping power scales with the scintillator light yield. In Fig. 3.1, it is shown how the variation of the collision stopping power and light yield can be compared for the energy range of 2–5 MeV. They both show that the change in stopping power, and consequently the light yield, is negligible.

According to the first design of the diagnostics, the normal to the LYSO screen is rotated by 45 degrees around the y-axis with respect to the electron beam line. The reflective component from the front surface of the scintillator is coupled to the optics (see Fig. 3.8). In case of the REGAE detector, the FOS is placed normal to the beam line. After the very recent upgrade at DC3, the beam arrives at the screens surface perpendicular and the forward emission from the back surface of the crystal is collected by a mirror, which directs the 90-degree deflected beam to the diagnostics optics. One can compare the light collection efficiency and scintillator resolution in the latter mentioned setups. In the simulations, the interaction medium together with the sensitive medium are rotated by 45 degrees. The detector is attached once to the front surface to capture the backward emission and once to the back surface of the scintillator to detect the forward emission. The beam profile on the LYSO surface, in terms of intensity and resolution, is evaluated for four different geometries as shown in Fig. 3.8. In case of a tilted screen, the electron passage in the medium is longer and therefore the deposited energy and consequently the light yield increase. On the other hand, the scintillator tilt enforces an extra spread on the beam profile in the horizontal direction. When the screen is normal to the beam axis, no further extension is added to the beam profile. The forward and backward emissions from the scintillator for equal rotational geometry, resemble a lot in terms of

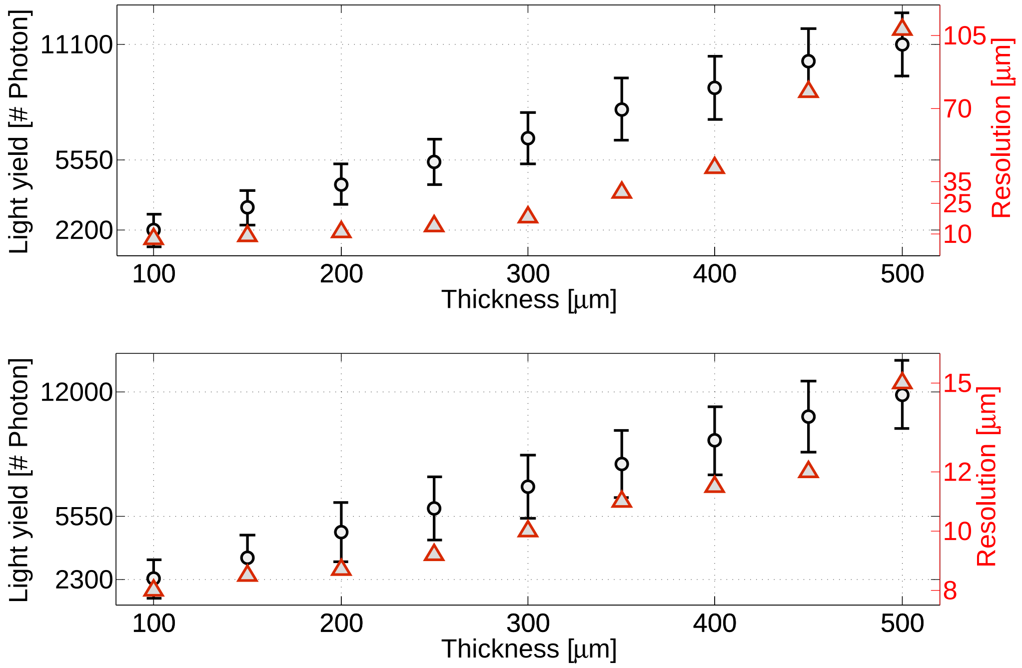

FIGURE 3.5: Light yield and resolution as a function of the thickness of the scintillator. The electrons energy is 5 MeV.

the scintillator resolution and output intensity. This implies that the light is emitted almost isotropically.

Figure 3.9 illustrates two basic designs of the transverse beam profile monitors. Currently, REGAE benefits from both designs. For fixed dimensions of the scintillator screen, the collection efficiency of each setup was obtained from simulations. The efficiency of the first setup is higher due to the longer passage of electrons inside the matter.

3.4.2 Fiber optic scintillator (FOS)

Earlier in this chapter, the advantages of an FOS and especially of the one used at REGAE, were listed and explained. Specific experiments were performed to characterize this device more precisely. In addition, as the use of FOS is expanded to more applications, simulating this device becomes equally important.

In the FOP, the fiber optics form bundles that are parallel to each other. Each fiber consists of a core glass and a clad glass that encircles the core glass. The refractive index of the core should be higher than that of the clad glass. At the boundary surface between the core and the clad glasses, any light with an angle exceeding the critical angle is internally reflected. Multiple reflections from the boundary surfaces, cause propagation of light along the fiber. The angle at which light enters the fiber is the same as the angle

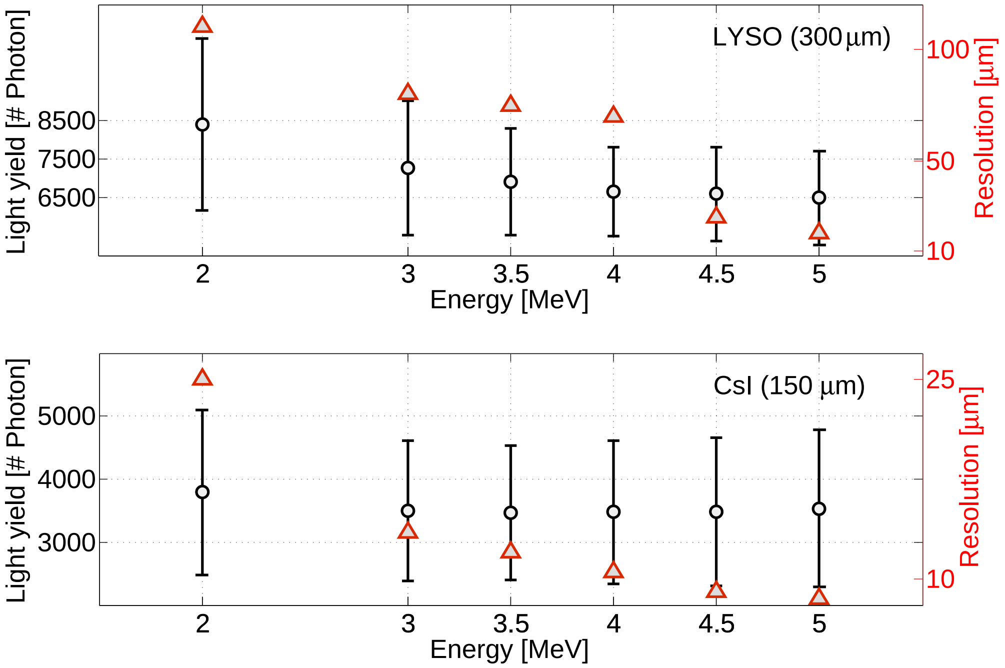

FIGURE 3.6: Light yield and resolution versus energy of the incoming electrons. The thicknesses of LYSO and CsI are 300 μm and 150 μm, respectively.

at which it leaves the fiber. Figure 3.10, depicts a traversing photon through a single fiber. If light hits the core glass, the maximum acceptance angle ($\theta_{acc,max}$) is given by,

$$\sin \theta_{acc,max} = \frac{n_1}{n_0} \cos \theta_c, \tag{3.5}$$

where θ_c is the critical angle. The quantities that are necessary to be known for simulating the fiber, are the refractive indices of the core and clad material and the optical photon absorption length. From the Hamamatsu catalog, the refractive indices can be found, however the glass materials are kept as confidential by the company. It is however known that the absorption length in the core material should be such, that the optical photons traveling along 3 mm of the fiber, are barely dissipated. Therefore in the simulation, a long absorption length has been considered for the core material and most of the photons that are bounced in the fiber, transfer to the end of that. In the structure of the fiber optic plate, there are absorbent glasses to absorb any stray that was not reflected in the core. There are different methods of adding this material to the FOP structures. The FOP is normally designed so that the stray light is absorbed in two or three passes. Within the simulation, the absorption lengths of optical photons inside the clad glass has been introduced to be very short to accomplish absorption of the unwanted photons. When an electron hits the scintillator and generates light, not all the emission can be coupled to the fiber and be transported. The transmittance of a fiber has been estimated by GEANT4 simulations. For this purpose, two different setups have been created, one comprising of a fiber optic and another that does not.

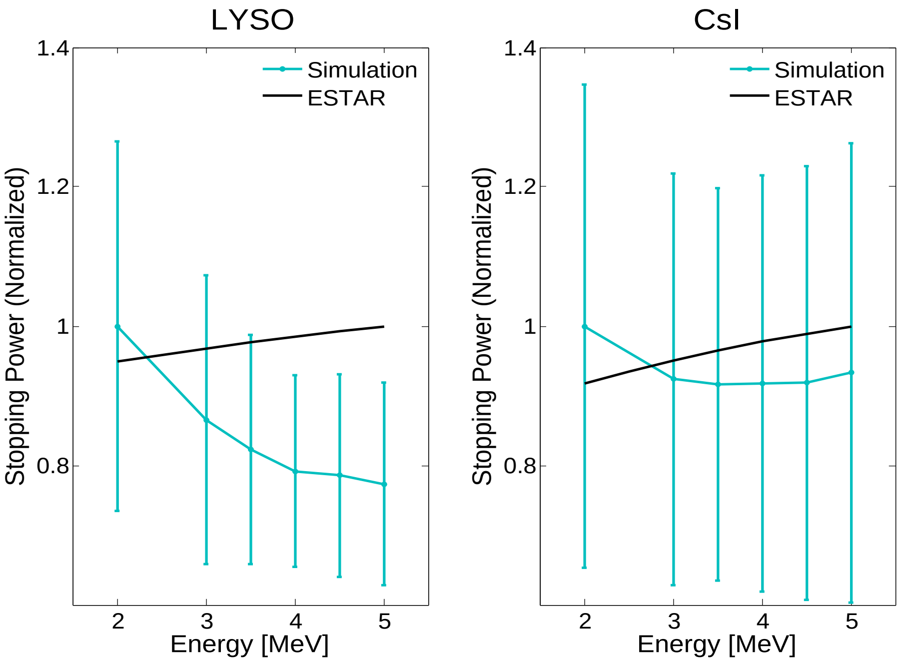

Figure 3.7: Collision stopping power calculated from the ESTAR database and inferred from Geant4 simulations as a function of the electron energy.

Figure 3.11, illustrates the two setups. The one on the left shows a cylinder of CsI(Tl) crystal scintillator with a thickness of 0.15 mm. A detector of the same shape and equal cross section is placed behind the scintillator with a zero distance from the back surface of the scintillator medium. The same shape and material have been chosen in the second geometry. In between the scintillator and the detector, there is a bar of fiber optic. The core diameter is equal to the detector's and CsI's diameters, 6 μm. The clad thickness is 1 mm. The photon counts on both detectors are derived from the simulation and it is concluded that 45% of the light is not coupled to the fiber optic. In other words, the transmittance of the light by the fiber is 55%. The simulated fiber has the best acceptance angle among other available types of FOPs. The core and clad refractive indices are 1.82 and 1.495 in this type and if the surrounding area is air ($n_0 = 1$), the acceptance angle is 90° (see Eq. 3.5). Thus, the estimated transmittance is the maximum possible value. The employed FOSs at REGAE are of this type.

The pillar structure of the scintillator plays an important role in improving the transmission efficiency. Figure 3.12 shows that if the scintillator's diameter increases, in such way that we approach a single crystal case, the efficiency of the light transmission by the fiber degrades.

The FOS can be simulated when an array of millions of joint scintillator-fiber columns are placed parallel to each other. Hence there is a simulation model to evaluate the FOS, for various possible configurations. Further experimental evaluation of FOS and its emission profile are presented in the next section.

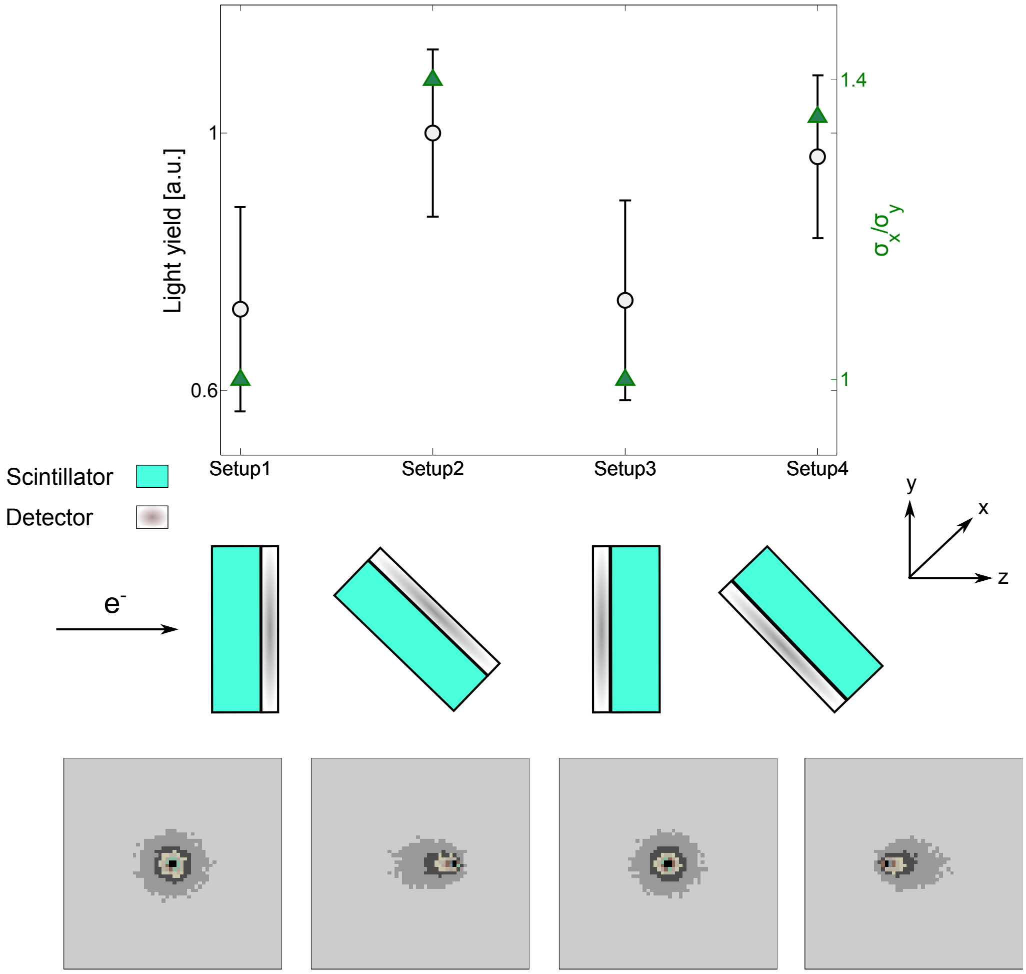

FIGURE 3.8: Light output and ratio of the horizontal RMS size to the vertical RMS size (top) for four different simulation setups (middle). The corresponding beam profiles on the detector are also shown (bottom). For all the setups, the beam energy was set to 5 MeV and the scintillator material is LYSO(Ce) with dimensions of $(20\times20\times0.3)\text{mm}^3$

3.5 Experimental evaluation of FOS and LYSO(Ce)

As it was explained above, one expects a more collimated light from FOS because the very diffused component of the emission is eliminated. On the other hand, the radiation from LYSO is expected to be more diffused. These features can be demonstrated and examined through an experiment. The intensity of particle-induced scintillation from a LYSO screen and an FOS is measured as a function of distance from them. A beta source of $^{137}_{55}Cs$ with activation of 200 kBq supplies electrons for this measurement. The FOS and LYSO are placed beneath the radiation source and their entire surface is exposed to the source. The FOS has an aluminum layer for protecting the CsI scintillator and it also reflects the backwards photon emission. Therefore the FOS is blocked from its back-side, while the LYSO is a transparent crystal and the backward component of

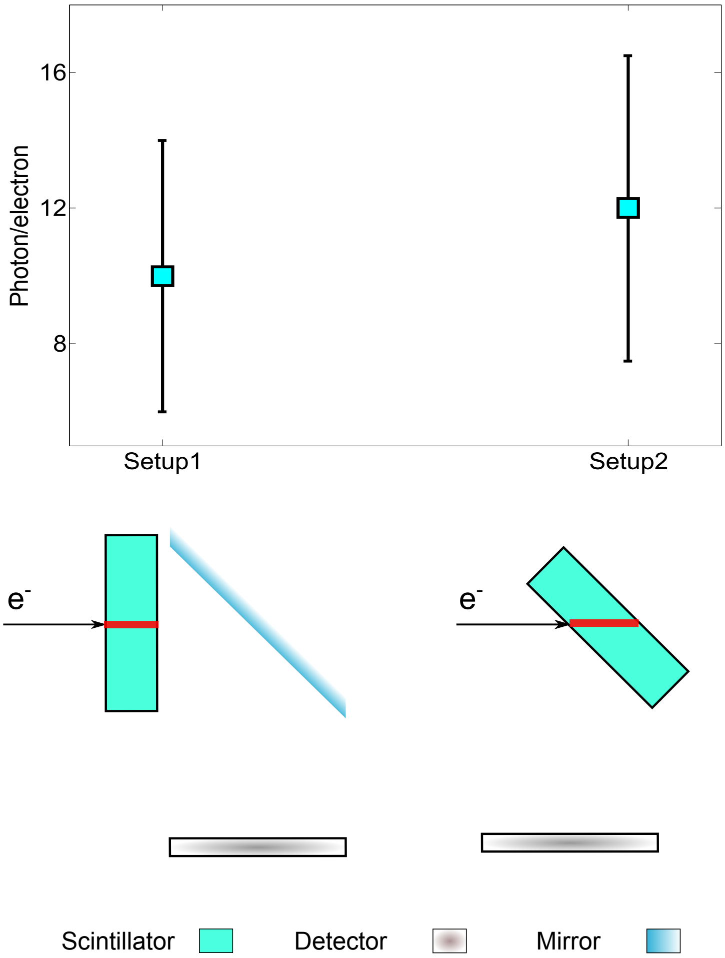

Figure 3.9: Collection efficiency obtained for different setups (top). The geometry corresponding to each setup is also shown (bottom). The beam energy is 5 MeV and the LYSO(Ce) screen has dimension of (20×20×0.3) mm^3.

scintillation can be reflected from the surrounding and contribute to the background. Thus, the back surface of the scintillator is covered by light-tight tapes. Moreover, the radiation source is inside an enclosure of plexiglas. The source is radiating in 4π and it causes unwanted light emission from passage of electrons inside the enclosure matter. Accordingly, a coverage of light-tight tape around the enclosure is also required. Under the scintillator and FOS, there is a 45 degrees mirror, which guides the light from the vertical to the horizontal axis towards the optics and the detector. A C-mount camera lens with excellent F-number of f/0.95 (see Appendix B), collects the light and focuses it on an sCMOS camera chip, Neo [61]. For this experiment the detector is cooled down to -35°C. In order to suppress the background light, the entire setup is enclosed by a light-tight shield and the measurements are performed in a dark room to minimize penetration of undesired background photons into the setup. A schematic of the experiment is depicted in Fig. 3.13. By changing the distance between the mirror and the opto-detection system, the intensity of the emitted light is measured. The camera is exposed to the radiation for periods as long as 100 seconds. The relative variation of the intensity as a function of the distance is monitored and the emission profile is derived.

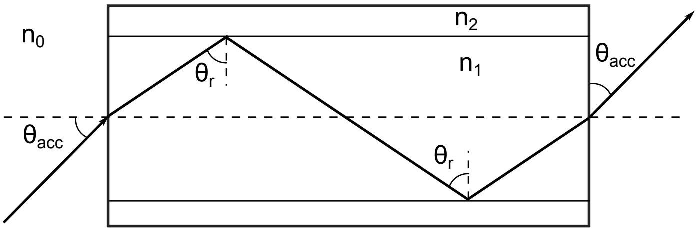

FIGURE 3.10: Schematic of the passage of a trapped photon inside a fiber. n_0, n_1 and n_2 are the refractive indices of the surrounding material, core and clad glass, respectively.

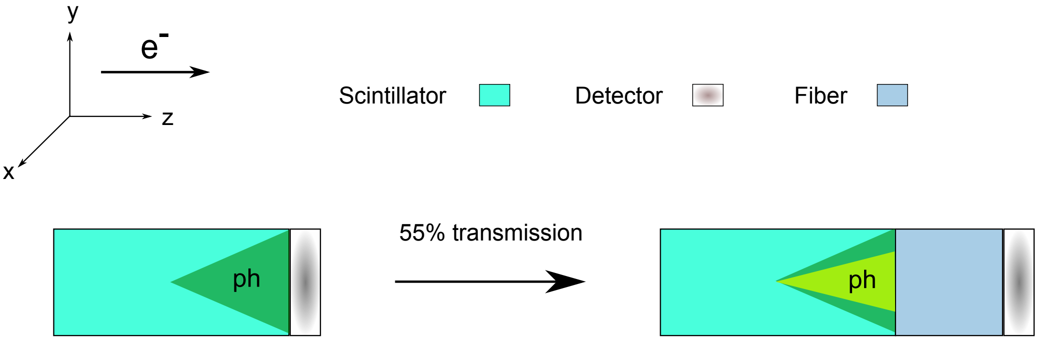

FIGURE 3.11: A cylindrical CsI(I) and a sensitive detector attached to it (left). Similar scintillator and detector, separated by a fiber optic (right). The cross sections of the scintillator, detector and fiber optic are equal. In the FOS, the length of the FOP is 3 mm, but in the simulation it is reduced to 0.05 mm to shorten the tracking length. Indeed, because of the low absorption, the difference in the result is negligible. The transmission efficiency is estimated to be 55%.

During the measurement with the LYSO crystal, a very slow decay component of the scintillator, which contributed significantly to the signal of the scintillation was noticed. Removing the particle source, the cause of the secondary emission should be known. We assumed that the decay can be either related to the scintillator afterglow or excited phosphorescence due to the room light illumination or both of them. In order to characterize the light-induced phosphorescence, the scintillator was moved away from the beta source for a long enough time. Thereafter, it was exposed by light of the room for quiet a long time. Later, in a dark condition, many consecutive shots recorded the corresponding decay behavior of LYSO. The main component of the decay is measured to be around 3 hours. To examine the afterglow of the scintillator, it was moved into a light-tight box besides the beta source and kept there for more than a day to irradiate the scintillator and eliminate the light-induced phosphorescence. Afterwards, its radiation induced decay was monitored in multiple shots, in absence of the beta source. The decay of this process is relatively fast and about less than an hour. The total dose of the radiation source reached to 1 nC and for a more reliable measurement, one needs a source with a higher dose. Apart from radiation-induced emissions, because of the radioactive isotope ^{176}Lu contained in luthetium [62], LYSO is intrinsically radioactive. Eventually, for long exposures of 100 sec the desired fast luminescence of LYSO is strongly dominated by

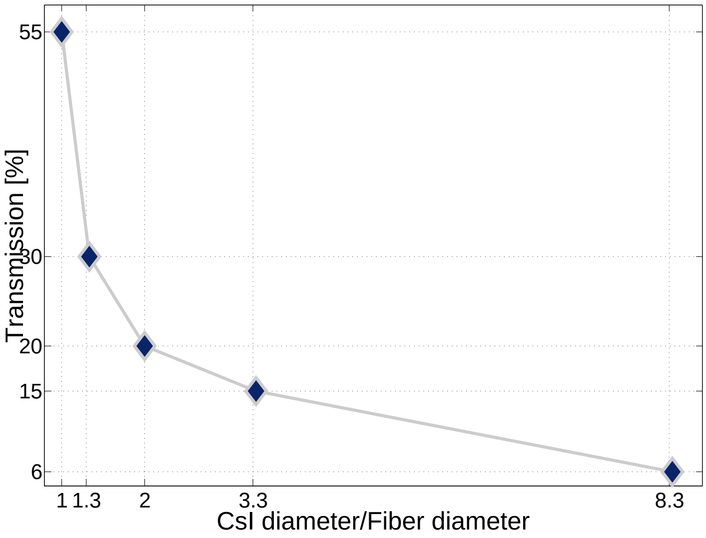

FIGURE 3.12: Transmittance variation versus ratio of the scintillator diameter to the fiber diameter. The result shows that the columns of the scintillator as extension of each individual fiber in FOS, can significantly improve the transmission efficiency.

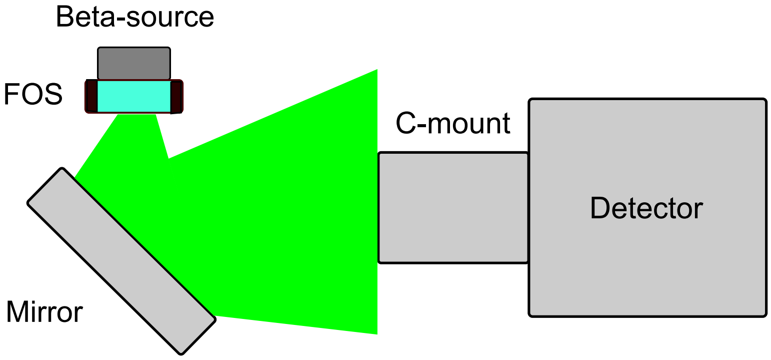

FIGURE 3.13: Schematic of the experiment for evaluating the profile of emissions from FOS and LYSO.

the mentioned slow components and on the other hand, with shorter integration time, the signal is too weak. Due to the mentioned complications, the elimination of the slow emission has not been accomplished so far and the measured emission profile of FOS is compared to the simulated profile of LYSO in Fig. 3.14. It is shown that the intensity assigned to the FOS is higher than the one from LYSO for smaller angles.

3.6 Simulation of the laser beam profile monitor

At REGAE, before the UV laser beam couples to the cathode, it is split and the sideway beam is directed towards a BGO scintillator ($Bi_4Ge_3O_{12}$) taped on top of a CCD sensor.

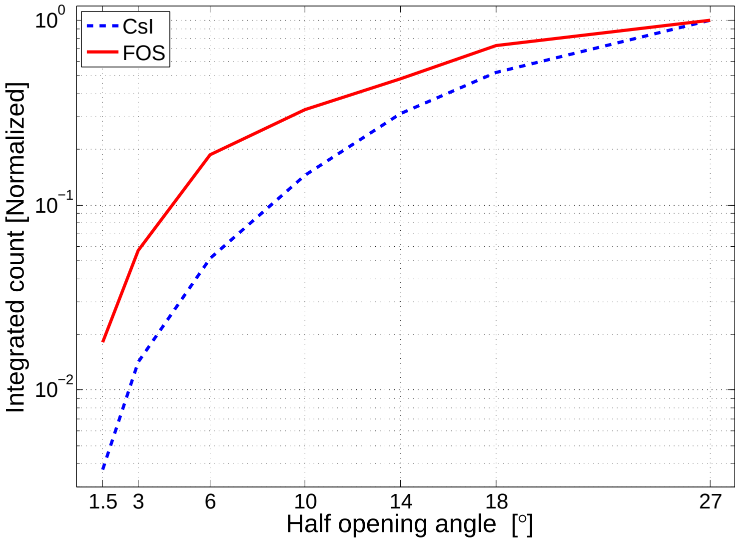

Figure 3.14: Total intensity of scintillation emission from LYSO and FOS as a function of half opening angle. The emission profiles show superiority of FOS over LYSO specially in small angles.

This monitor resembles the position of the real cathode and is called ”virtual cathode”. One can characterize the beam transverse shape and control its position on the cathode, using this setup. BGO crystal is a high density material ($\rho = 7.13$ g/cm^3) and its peak of emission occurs at about 480 nm. Its light yield is three times lower than LYSO's and the decay constant is around 300 ns. Thus, this material is slower and a less bright scintillator with respect to LYSO [63]. Therefore, for electron beam diagnostics LYSO is considered a better choice, rather than BGO. However, BGO shows a better response to UV light through fluorescence process. In the fluorescence or wavelength shifting process the fluorophore (fluorescent substance) is in an excited state after the absorption of an optical photon provided by an external source (here the UV laser). The life time of the excited state is of order of 1–10 ns, during which the fluorophore interacts with its environment and ends-up in a relaxed-excited state. The last step is the emission of a photon with an energy/wavelength smaller/larger than the one of the excitation optical photon. The wavelength shifting process can be included in the Geant4 physics processes. The user needs to define the fluorescent emission spectrum and absorption length, which is the average distance traveled by a photon before it is absorbed by the fluorophore. The absorption length spectrum is inversely proportional to the photo-excitation spectrum.

In the simulation geometry, a scintillator screen, with dimension of (20×20) mm^2 and a varying thickness, is defined either with material properties of LYSO or BGO. A sensitive detector with an identical surface area is attached to the back surface of the scintillator. 10^6 mono-energetic photons of 5 eV, arranged in a Gaussian beam of ($\sigma_{RMS} = 0.57$ mm) hit the scintillator perpendicularly. Results of this simulation for LYSO and BGO are presented in Fig. 3.15, where the RMS size of the beam profile and the photon yield are plotted as a function of the thickness of the scintillator. The absorption coefficient of

BGO at $\lambda = 266$ nm is higher and consequently the fluorescence intensity is enhanced, but at the price of a degraded resolution. For a thickness above 400 μm, there is no gain in the intensity and the emitted photons are mostly absorbed by the medium.

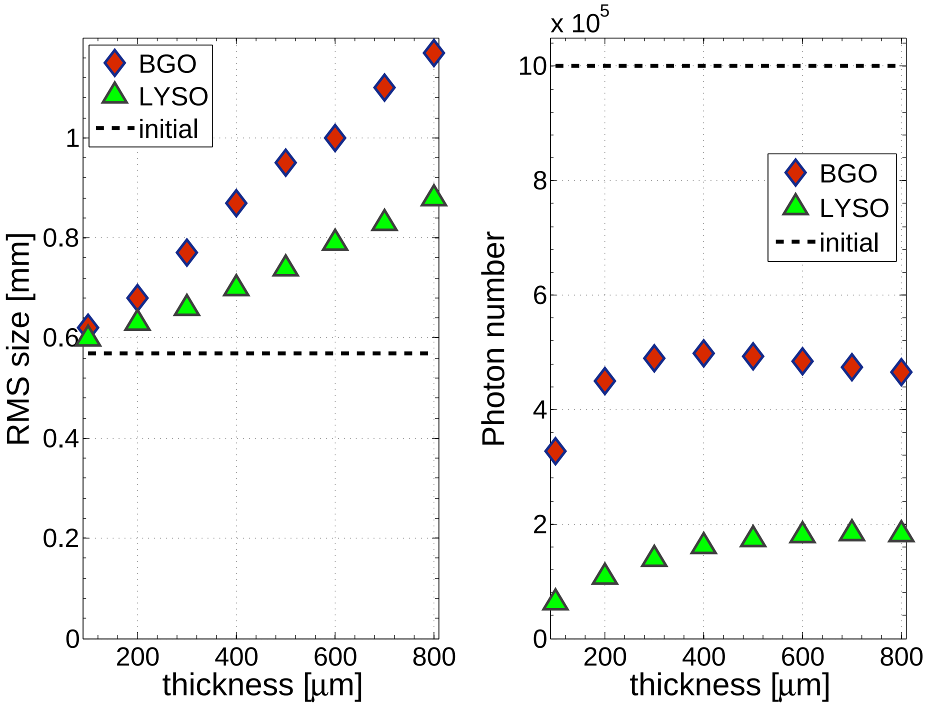

Figure 3.15: The simulated UV beam profile size and intensity of fluorescent emission on LYSO and BGO crystals.

Chapter 4

Diagnostics of electron bunches at REGAE

Electron beam diagnostics is an important aspect for the operation of an electron accelerator, involving the measurement and preservation of the beam parameters. The eligible highly coherent, ultra-low charge, ultra-short relativistic electron bunches at REGAE enable a profound insight of the fast atomic processes of the specimen under study through electron diffraction experiments. Therefore, sophisticated diagnostics tools are required to characterize the beam and maintain its parameters in order to accomplish femtosecond electron diffraction experiment.

Reducing the bunch charge for the pump-probe experiment at the interaction point is an efficient solution to overcome space charge broadening and provide a short bunch. That causes major challenges for the beam diagnostics. As a consequence, the charge and beam profile measurements are influenced by this characteristic intensity and the relevant diagnostics equipments should be modified and empowered for this purpose. The beam profile monitors are established based on light emission from a scintillator, intercepted by the electron beam. A high photon yield of the scintillator, a proper imaging optics and sensitive detectors provide an efficient system for transverse beam profile measurements. A Faraday cup as well as a cavity monitor, so called DaMon [64], are the existing charge monitors at REGAE. While the Faraday cups can read the charge down to 30 fC destructively, the sensitivity of DaMon is boosted down to 10 fC and can measure the charge non-destructively with higher precision. This cavity with resonance frequency of 1.3 GHz has been designed for dark current measurement at FLASH and PITZ. Since the cavity is not resonant at 3 GHz, it is insensitive for the dark current at REGAE, but it is a very sensitive charge monitor. Dark charge issues are very essential in ultra-low charge operation. A Faraday cup that is equipped with an additional amplifier provides an ultra sensitive mean to measure dark charge, which in turn can be used to further optimize the machine settings [65].

Frequently, it is desirable to determine experimentally the particle energy and energy spread to evaluate the quality of the beam and characterize some beam parameters such as normalized emittance and coherence length. For this purpose a dispersive magnet bends the electrons onto a beam profile monitor.

Compression of the electron bunch below the characteristic length of atomic evolution, is necessary for the dynamic diffraction experiment. Consequently, bunch length diagnostics is essential to find out whether the required temporal resolution is achieved. Since the desired resolution falls within very tough limits of several femtoseconds, conventional tools like streak cameras don't provide that fast response and accordingly they cannot be considered. One can solve this problem using the laser Ponderomotive effect to spatially deflect electrons. This scattering process provides a mechanism to cross-correlate an unknown electron pulse with a known laser pulse to determine the electron pulse duration and t=0 position [7, 66]. The t=0 position is the time, in which the overlap between the centroids of the electron probe and the optical excitation pulse occurs. This new technology advanced the temporal resolution by more than an order of magnitude over streak cameras and enabled pulse duration characterization with high precision of 10 fs. There have been some efforts to prepare the Ponderomotive setup at REGAE. The main idea was to firstly determine t=0 position independently through a time-resolved diffraction of an ablation process, and then perform Ponderomotive bunch length measurement. Currently in parallel to the Ponderomotive technique, design and development of an RF transverse deflecting cavity for accurate measurement of ultra-short bunch length are ongoing. A high frequency RF field gives a time-dependent transverse kick to the electrons that are monitored by transverse diagnostics [67].

In this chapter the transverse beam profile monitors, their basic design, performance and applications are entirely described. Other diagnostics systems, which are currently in operation are explained as well.

Depending on the case of study, different methods of measuring the transverse beam profile can be applied. Scintillator screens, Optical Transition Radiation (OTR) screens and wire scanners are the most conventional tools, being used for this purpose.

Scintillator screens: An incoming charged particle on the scintillator medium, deposits fraction of its energy to create electrons and holes. They move to the luminescence centers, transfer the energy to these centers, which then they radiate in the visible range. The deposited energy and the emission distribution depend on the energy of the particle, the material and its geometry. A comprehensive description of the scintillation process is given in chapter 3.

OTR screens: When a relativistic charged particle crosses the interface of two media with different dielectric constants, the sudden change in the electromagnetic field causes the emission of light. This radiation, within the visible spectrum, is called optical transition radiation (OTR). The transition radiation was theoretically proposed by Ginzburg and Frank [68] in 1945 and was observed for the first time by Goldsmith and Jelleya in 1959 [69]. The radiation is directed forward and backward with respect to the intercepting point of the beam at the medium. At $\theta = 1/\gamma$ the intensity of the radiation attains its maximum value, which γ is the Lorentz factor. The higher the energy of the particle is, the higher the peak of the intensity moves. The OTR-based diagnostics is a widespread technique to monitor the transverse distribution of the electron beam.

Wire scanners: Unlike the aforementioned techniques, this is a non-destructive way to measure the transverse beam profile. The method is based on the scattering of the impinging particles from a single wire. The wire can be swept through the beam in the transverse plane, in horizontal and vertical directions. In order to guarantee a good resolution, the transverse momentum of the secondary particles should not differ much from that of the primaries. Therefore, a low energy deposition in the wire is needed and consequently the thickness of the material should be limited to several tens of micrometers. The wire material is often carbon or tungsten due to the good thermal and mechanical properties of these elements [70]. The scattered electrons are detected by a scintillator and PMT.

At REGAE, the diagnostics has to cope with low-charge bunches of 2–5 MeV electrons. Excess of charge within a bunch would degrade the beam quality in terms of emittance and coherence length and influences temporal and spatial resolution of the time-resolved study (see chapter 1). With repetition rate of <50 Hz, the specimen is exposed by both the electron and the laser excitation pulses in every corresponding cycle. Each cycle is moved with small steps in time to monitor the dynamic of the fast phenomenon through varying diffraction patterns. Besides, in the static diffraction experiment, the beam instability in terms of intensity and position should be decoupled from the beam quality. Hence, necessity of developing a shot-to-shot basis diagnostics becomes more prominent and the consequent challenges of transverse beam profile measurements should be dealt with. Scintillator screens, which are identified as high-light output materials are the best candidates for such diagnostics. Although the ionization loss of many scintillators within this energy range falls to a minimum value, a bright scintillator like LYSO (Cerium-doped Lutetium Yttrium Orthosilicate) can compensate for that. With OTR screens the photon intensity is enhanced considerably by boosting the Lorentz factor in relativistic energies. Additionally, the angular spread of the emission is increased at low energies, restricting the resolution and collection efficiency for the imaging. For the range of energies used at REGAE, the usable light of an OTR screen is orders of magnitude lower than from a scintillator screen. OTR screens are mainly used for electron energies higher than 100 MeV. One of the main disadvantages of the scintillator-based monitors, is the relatively low resolution, which also depends on the particle energy. Hence, there is a trade-off between the resolution and light yield of a scintillator, with respect to the thickness of the scintillator screen. For OTR screens, the photon intensity and distribution do not depend on the material's thickness. Therefore, very thin foils with thickness of fractions of micrometers can be used to minimize the influence of scattering on the primary beam. The scintillator screens undergo saturation when they are exposed to high beam densities. At REGAE, the normal operation is performed at sub-pC beam charge. For a beam as small as 200 μm RMS, the LYSO screen does not show any saturation for the entire range of operation (10 fC–1 pC) and the scintillator's response is decently linear. At high energies, the OTR screens are preferred over the fluorescent screens for diagnostics. However, once the longitudinal structures in the bunch are comparable to the radiated wavelength, the radiation is emitted coherently

at that wavelength and is called coherent optical transition radiation (COTR). This has become a challenging issue in FEL-linac, since the COTR in the visible range does not represent the transverse profile of the beam correctly. For further details see [71]. In order to resolve this issue, scintillator screens can be utilized. Although the COTR still exists, it can be separated from the fluorescent component spectrally, spatially and temporally. The latter is accomplished using a gated image intensifier to bypass the COTR [72].
In conclusion, remarking the specific design parameters of REGAE beam, such as ultra-low charge and MeV energies, the scintillator-based diagnostics is the most appropriate tool to monitor the beam profile.

4.1 Transverse beam profile monitors

As previously mentioned, in order to monitor and maintain the quality of the electron beam in transverse plane along the accelerator, scintillator screens are employed. Together with a sensitive detector and the optics in between, they form the transversal profile monitors. The LYSO scintillator crystal can move into the beam line and is oriented at 45 degrees with respect to the electron beam path. The impinging electrons on the LYSO crystal cause scintillation emission in the visible range, which can be interpreted as an indirect transverse distribution of the electrons. There are three transversal diagnostic stations located at the accelerator. Another station for beam profile measurement is located downstream at the interception of the beam and the diffraction samples. The layout of the transversal diagnostics is depicted in Figure 4.1. The detector can be selected to be either a normal CCD or an intensified CCD (ICCD), depending on the study: for monitoring of ultra-low charge beams, the use of an intensified CCD becomes necessary, while electron bunches of higher charge in the range of several tens of fC to a few pC can be well diagnosed by the introduced below CCD.

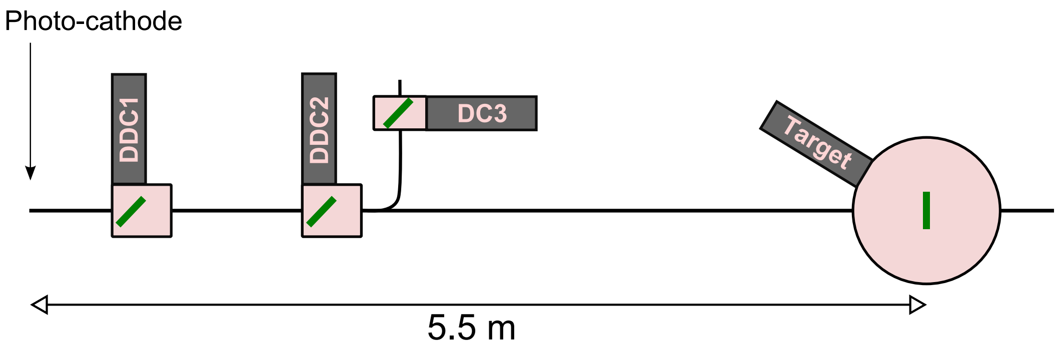

FIGURE 4.1: Layout of the transversal diagnostics at DDC1, DDC2, DC3 and the target chamber. The initial point corresponds to the photocathode longitudinal position. The spacings between the stations are scaled to the real distances, but the size of the elements is exaggerated.

4.1.1 CCD camera

The CCD camera model is JAI BM-141 with a monochrome chip, ICX285AL. The pixel size and the number of active pixel are 6.45 μm and 1392(h)$\times$1040(v), respectively. In the full frame operation, the camera's frame rate can reach 32 frames per second. However, within the communication through the video server, the frame rate is limited to 12.5 Hz, which is the current repetition rate of REGAE. This allows for the transversal diagnostics to be performed on a shot-to-shot basis. The minimum exposure time of the camera is 60 μs, which is already much longer than the RF window (6 μs). The exposure start can be pushed to the end of the RF gate to reduce the dark current background as much as possible. The camera exposure delay can be controlled via a timing module that is triggered by the master oscillator. In chapter 5, the main considerations in selecting the diagnostics CCD camera and some evaluation process will be extensively explained.

4.1.2 Image intensifier

In the ultra-low charge diagnostics scheme, a high-light output monitor like scintillator was introduced as a solution. An approach, which considers amplifying the incoming optical signal is of interest to be applied in the transverse beam profile setup. The image intensifier is a unit that enhances the detection sensitivity and is also able to suppress the dark current background (section. 5.2 and section. 6.4). Intensifiers are used in many applications ranging from night time viewing to various fields including industrial product inspection and scientific research. Gate operation models are also useful for the observation of high-speed phenomena. As an example, the scintillator emission has been characterized using a gated-intensifier coupled to a CCD (see section 6.3). The operation principle of an MCP-based image intensifier is described in section 5.2.

The amplified signal from the ICCD is coupled to a CCD either by a fiber optic coupler or by means of a lens. The employed ICCDs at REGAE are home-made and exploit lens coupling between an intensifier and the JAI BM-141 CCD. This provides the advantage of moving the intensifier unit and using the stand-alone CCD for those non-intensified applications. This is also counted as a cost-effective and more spacious method rather than fiber coupling approach. Fiber-coupled ICCD provides a better light collection efficiency.

4.1.3 The beam profile monitor optics

During normal operation at REGAE, the beam charge ranges between tens of fC up to 1 pC. Having the option to switch between the ICCD and the CCD in the diagnostic setup, the transversal diagnostics can monitor electron bunches over a wide range of charge, while achieving a sufficient quality of the signal. There are two distinct optical setups, which can image the beam profile on the detector planes. The CCD camera is fixed at the end of the setup and is used for both detection modes. Once a desired mode is chosen, the image intensifier and the relevant optics are moved into or out of the main optical axis. In Figure 4.2, the layout of the transverse beam profile monitor is shown. The scintillator screen, collecting lens (a) and CCD are aligned to the main beam line, which is labeled as (1); combinations of b and c create pairs of lenses that are mounted on a filter wheel and introduce zoom stages to adjust the image magnification and consequently the field of view. Overall, there are three levels of magnification. The image intensifier (f) and the lenses labeled g and e can move into the main axis and replace d, when the use of an intensified camera is needed for the diagnostics. A doublet achromate behind the intensifier couples the amplified light onto the CCD chip. In this way, a setup that is equipped with an ICCD is created. Six configurations corresponding to different combinations of the mentioned elements are considered, as shown in table 4.1. Each configuration was determined to satisfy different diagnostics demands. Table 4.2, presents some imaging properties of the optical configurations.

The optical setups are located inside black light-tight boxes, in order to protect the optics from the background light and environmental dust. Two motorized filter wheel and linear stage move the optical elements to create all the possible combinations in table 4.2. The filter wheel adjusts magnification of the optics and the linear stage exchanges the detection configuration between CCD and ICCD. The motors are integrated into the REGAE control system and they are operable via stand-alone Matlab and Java DOOCS Data Display (jddd) panels.

Table 4.1: The optical elements can be moved in/out the optical axis to create the following arrangements. For better understanding of each configuration see Fig. 4.2.

Configuration #	**elements**
1	a, b, c, d
2	a, d
3	a, c, b, d
4	a, b, c, e, f, g
5	a, e, f, g
6	a, c, b, e, f, g

Table 4.2: Imaging properties of diagnostics optical system for all the configurations shown in table 4.1.

Configuration #	**1**	**2**	**3**	**4**	**5**	**6**
Magnification	0.4	0.8	1.6	0.2	0.4	0.8
Scaling factor[μm/pixel]	16	8	4	32	16	8
Field of view–H [mm]	22.4	11.2	5.6	44.8	22.4	11.2
Field of view–V [mm]	16.8	8.4	4.2	33.5	16.8	8.4
Airy radius [μm] @430 nm	1.4	2.7	5.4	0.7	1.4	2.7

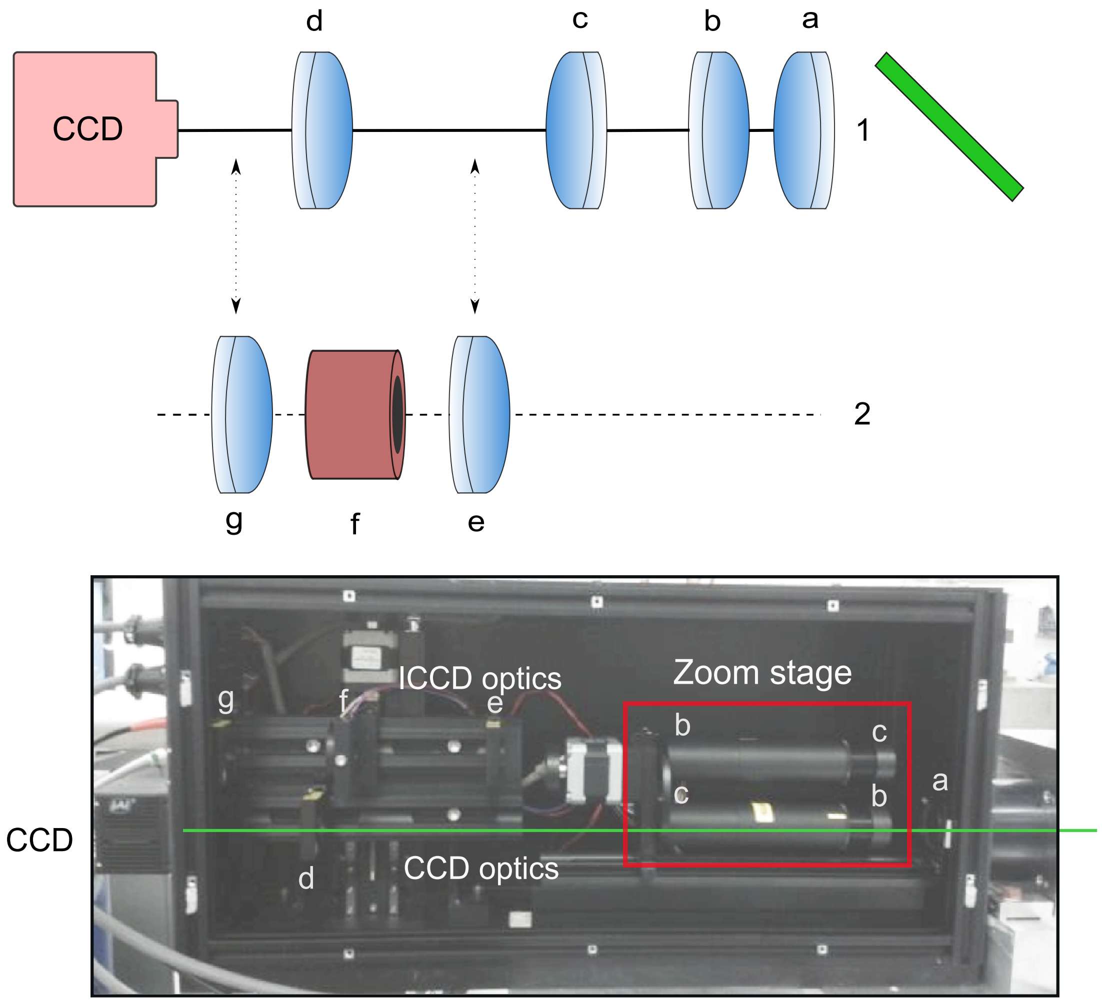

FIGURE 4.2: Layout of the beam profile monitor system (see text for details). It consists of two levels for detecting the electron beam profile: one with a normal CCD at higher beam intensity and the other with an ICCD in order to diagnose the beam at low charges. The focal lengths of the lenses are $f_a = 125$ mm, $f_b = 50$ mm, $f_c = 100$ mm, $f_d = 100$ mm and $f_e = 100$ mm.

4.1.4 Evaluation of the beam profile monitor resolution

In the beam profile monitor setup at REGAE, the resolution is defined as the response of the system to a point source, which in this case is a single electron. The width of the resulting light profile from the single electron describes the response of the system. There are different factors, which influence the resolution:

1. **Scintillator emission spread function:** Due to the deposited energy of an electron, scintillation light is emitted along its passage inside the material. The emission distribution on the exit surface of the scintillator is viewed by the monitor and the RMS size of the distribution is taken as the scintillator resolution.

2. Imperfection of the optical system: They can be caused by

   (a) Point spread function: Diffraction pattern from the optical apertures is known as the Airy pattern, named after George Biddell Airy [73]. The central spot of this pattern is known as the Airy disk. Assuming a perfect and focused imaging system, the Airy disk is the smallest size that the system returns as image of a point source. It is also known as point spread function (PSF).
   (b) Optical aberrations: The imperfection of the image, caused by the optical elements and their positions, is divided into chromatic and monochromatic aberrations (see Appendix B).
   (c) Depth of field (DOF): Since the scintillator is tilted by 45 degrees around the vertical axis, the distance from the object to the image plane in the horizontal direction varies and if it exceeds the DOF, then the sharp focusing along this axis vanishes. Therefore, the beam size in the vertical direction is more reliable.

3. **Angular acceptance of the optics:** The scintillator emits in $\Omega = 4\pi$, thus the optical aperture size and also the propagation distance to the optics determine the accepted portion of the emission through the optics. An optical parameter, F-number, qualifies the optical resolution and acceptance angle (see Appendix B). The lower the acceptance angle, the better the resolution is.

4. **Pixel size:** According to the Nyquist-Shannon sampling theorem [74], in the case of a band limited signal, the sampling frequency must be twice the bandwidth of the input signal to reconstruct the original spatial frequency component. Generalizing the statement to the image sampling case, the pixel size should be half the optical resolution to achieve the maximum resolution.

In order to characterize the total resolution, all the aforementioned aspects are taken into account as explained in the following.

The visible light is emitted as a result of the interaction of the electron with the scintillator crystal. The spread function of the radiated photons can be simulated using Geant4 [75], using the proper geometry and physics properties of the material. A description of this simulation tool and its application in characterizing the scintillators is given in chapter 3. In order to find out the inherent extension caused by the scintillator, a single electron hits the scintillator medium and the distribution of the visible photons is monitored up to the first optical aperture. The electrons cross the crystal in the center and the scintillator is tilted 45 degrees with respect to the incoming electrons. The backward emission from the scintillator that enters the optics is selected. The detector (as the optical aperture) is rotated by 90 degrees with respect to the electron path, as shown in Fig. 4.3. Two main geometries are studied. In the first geometry, a sensitive detector with the same size as the collecting optics is placed perpendicular to the beam. The detector is defined to be ideal (quantum efficiency of 100%). The angular distribution of the incident electrons on the detector shows that the photons with half opening angles of less than $\sim 7^\circ$ around the beam axis are allowed to pass through the optics. In addition to the angular distribution, the spatial distribution of the photons on the scintillator surface is of interest. Within the described geometry, the initial position of the photons inside the medium is extracted. For the second geometry, the sensitive detector is attached to the front surface of the scintillator. The backward component of the scintillation is collected by the detector. Among all detected photons on the scintillator's surface, only those that satisfy the angular conditions in the former geometry, are selected.

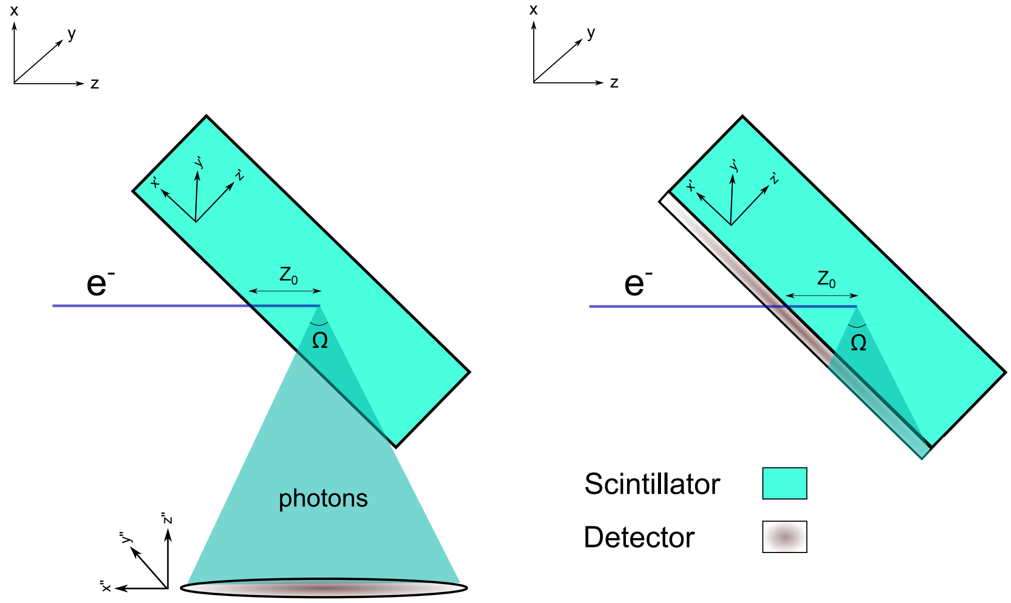

FIGURE 4.3: Two different simulated geometries. In the left image (x, y, z) are the coordinates with respect to the world volume. The scintillator and detector coordinates (x', y', z') and (x'', y'', z'') are rotated by 45° and 90°, respectively. The electrons strike the scintillator along the z-axis. At the interaction points, the photons are produced (Z_0) and emitted in all directions. The illustrated cone, encompasses the photons that are captured by the detector. The distance from the center of the scintillator to center of the detector is 125 mm, equal to the focal length of the collecting lens. In the second configuration (right), the detector is attached behind the scintillator. The thickness of the scintillator is 300 μm.

In order to be able to study the influence of the optics on the resolution, the selected photons on the surface of the crystal can be considered as a light source, which travels through optical components of the profile monitor setup. ZEMAX [76], an optical design program, is used to simulate the setup for propagation of the rays through the optical system. The angular and spatial distribution of simulated photons on the scintillator surface determine the coordinates of a user-defined source in ZEMAX. The rays are traced through the optical elements of the setup, accordingly reflected, refracted or absorbed by each lens medium. Thereafter, they continue along a new path towards the detector's (equivalent to the CCD camera) surface. The photon emission, initiated from single incident electron on the scintillator, passes through the optics and is imaged on a detector plane (see Fig. 4.4). In Fig. 4.4 the beam spots for configurations 3, 2 and 1 are shown from left to right. The main cause for the existing inconsistency in the beam size is the diversity of the transmission factor and the collection efficiency for each individual setup. The collection efficiency of the optical system influences the spot size

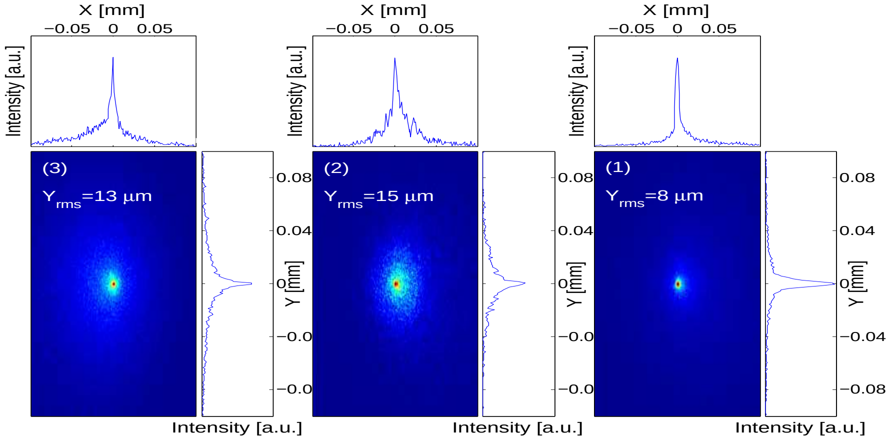

FIGURE 4.4: Photon beam spots initiated from single electrons, on the detector surface for configurations 3, 2 and 1 (keeping the order from left to right), obtained from ZEMAX simulations. The RMS size along the y-axis is shown on the figures and is the reference for the beam size measurement. For the calculation of the RMS size, the region of interest is an area where the signal-to-noise ratio varies between 1 to 10.

and consequently the resolution. Figure 4.5 shows that the beam size and transmittance variations are compatible. The spot size is reduced, when the transmission and coupling efficiency of the light through the setup is lowered.

A second ZEMAX simulation, with an identical setup, was performed in order to characterize the wave-related behavior of the rays during their propagation. For instance, the PSF is calculated. The PSF value represents the resolution, provided that the imaging resolution is diffraction limited. In this case, the total resolution of the diagnostics system is derived when the optics PSF and the propagated scintillator emission spread are convolved. Nevertheless, one should notice that the camera pixel size influences the entire resolution of the system. In summary, according to the ZEMAX simulation results, in order to determine the optical resolution of the system, the following complications should be dealt with:

- In the second simulation, we consider three field points across an object, at the top, in the middle and on the side of it. Each of the field points is equivalent to a point source. Rays are traced from these points to the image plane. By default, ZEMAX plots the spot diagram for each field point, which is an indication of the image of a point object. The system's optical imperfections can be judged by comparing the spot diagrams associated to the three different field points and wavelengths. The spot size variation as a function of wavelength demonstrates the chromatic aberration, while the uniformity of the spots of the different field points indicates the monochromatic aberrations. Figure 4.6 depicts the image of the three field points. The spot sizes are optimized for the peak wavelength of the scintillator's emission. If the spot size is smaller or equal to the size of the Airy disk, the optical resolution is diffraction limited, otherwise, the system's imperfections add

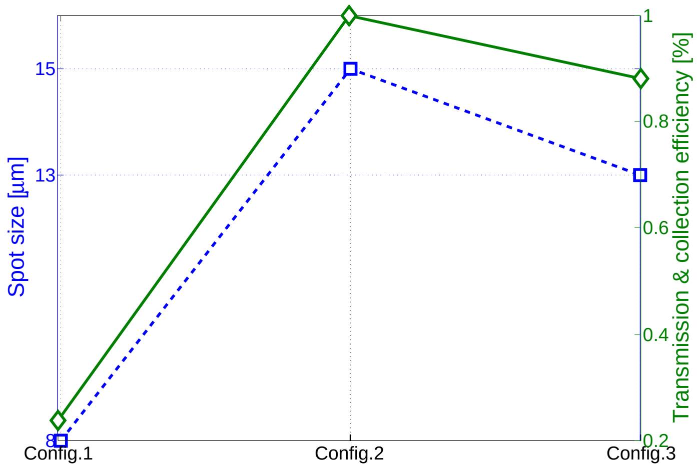

FIGURE 4.5: Transmission and spot size for three optical configurations. The transmittance and collection efficiency affect the beam resolution. Therefore, the spot sizes are different from each other. The change in coupling efficiency is caused by the optical aperture. For example, in Configuration 1, the zoom stage aperture constraints the light collection efficiency. Part of the change is related to the light transmission. When more lenses are applied in the setup, the dispersion increases and the transmission factor lowers. The transmission and collection efficiencies of Configuration 1 and 3 are scaled to the ones obtained with Configuration 2.

further limitations in resolving the image. The Airy radius is calculated by ZEMAX. According to the illustrated diagrams in Fig. 4.6, the Airy radii are larger, but comparable to the size of the spots. Thus, the resolution can be estimated by the image PSFs. The PSF values and scintillator spread function can be used to obtain the entire resolution of the monitor system. In the spot diagrams of Fig. 4.6, only one wavelength is taken into consideration. After including the emission spectrum of the scintillator in the simulation, chromatic aberrations appear. Consequently, the spot size increases significantly. In Fig. 4.7, the spot size variation for three different wavelengths is shown, for the three different configurations. The total spot size is obtained when the spot diagrams of the three colors are combined. The imaging resolution is limited more due to the resulting spot size than due to PSF. The chromatic spot size values are given in Table 4.3.

- As previously mentioned, the CCD pixel size plays an important role in resolving images. So far, the image resolution investigations have been done up to the camera surface. Therefore, the spatial sampling rate of the camera has to be included into the related evaluations. Assuming that the optical system is free of chromatic aberration and the optical resolution is equivalent to the image spot size, the camera's pixel size should be larger than half of the optical resolution. However, the condition of the Nyquist-Shannon theorem is not satisfied for all the configurations (see Table 4.3).

Laboratory measurements: Due to the aforementioned complications, an experimental approach can also be considered to determine the optical resolution and then convolve

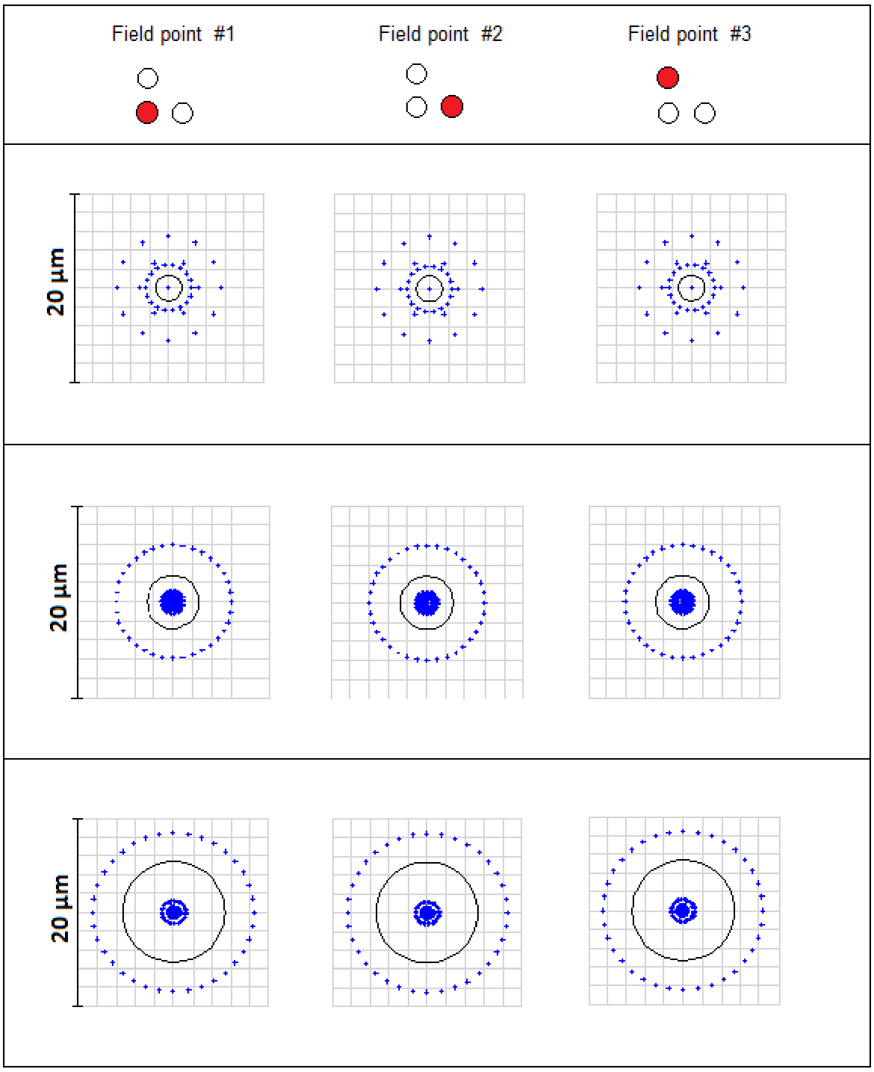

Figure 4.6: The standard spot diagrams and Airy radii for configuration 1 (top), configuration 2 (middle) and configuration 3 (bottom) are shown. The spots are representing three different points on an extended object. The solid circle in each digram defines the Airy region. The wavelength is set to 430 nm. The points on the spot diagrams show positions of the traced rays, originating from the field points.

it with the scintillator resolution. Before the diagnostics stations were installed in the machine, all the configurations were examined in the laboratory. If a light source, whose profile resembles to the scintillator emission profile (Lambertian), can be produced, then both setups in the machine and in the laboratory are comparable in terms of optical resolution. The scintillation profile almost matches a Lambertian profile [77, 78], therefore we should be able to create a similar source. Figure 4.8 shows an experimental layout to produce such a source. Different configurations are introduced within this experiment, as shown in Table 4.4.

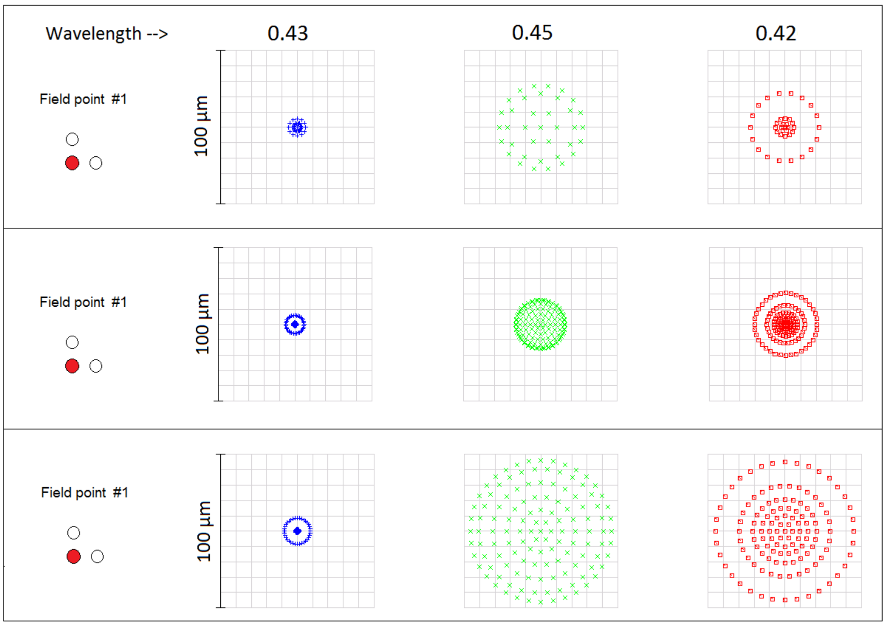

FIGURE 4.7: The matrix spot diagrams of all existing source fields are illustrated. The wavelength dependence of the spot sizes is an indication of chromatic aberrations. The emission peaks at 430 nm and the neighboring wavelengths have significant contribution in the spectrum of the emission.

TABLE 4.3: The image magnification, scaling factor and PSF at all wavelengths are given in this table. The camera real pixel size is 6.45 μm. The spot size values have been calculated after including the chromatic effects.

Configuration #	Magnification ×	Pixel size [μm/pixel]	PSF [μm]	Spot size [μm]
1	0.4	6.45	1.8	17
2	0.8	6.45	2.3	9
3	1.6	6.45	4.6	21

For a system with a Lambertian source in use, the coupling efficiency is [79],

$$g = \frac{T}{4F^2(M+1)^2+1}, \tag{4.1}$$

where T is the bulk transmission, F is the F-number and M is the magnification (object/image). In the laboratory, the source is built by a green laser, which hits a plastic diffuser. In order to inspect the profile of the produced light, three configurations are arranged (see Fig. 4.8 and Table 4.4). One can compare their coupling efficiencies, by

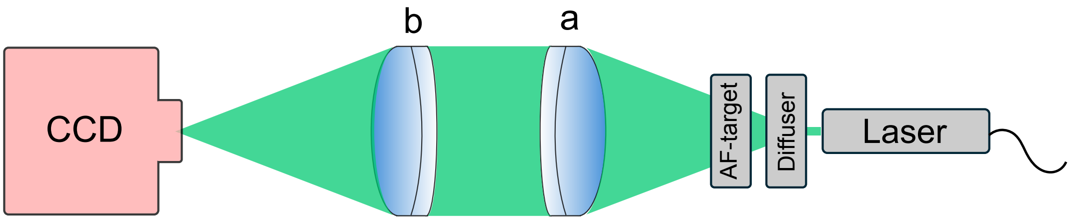

Figure 4.8: Layout of the experiment, which is arranged to produce a Lambertian-like source. A laser beam is diffused by plastic layers. Lens (a) has a distance equal to its focal length from the target screen.

Table 4.4: Three configurations have been arranged to examine the light source characteristic profile. The focal lengths and F-numbers of the lens pairs are given.

Configuration #	f_a **[mm]**	f_b **[mm]**	F_a**/No.**
1	100	100	4
2	200	100	4
3	125	100	4.2

measuring the transmitted intensity through all the configurations,

$$\frac{g_1}{g_2} = \frac{\frac{T_1}{4F_1^2(M_1+1)^2+1}}{\frac{T_2}{4F_2^2(M_2+1)^2+1}}. \tag{4.2}$$

Assuming that the bulk transmissions are the same, we obtain,

$$\frac{g_1}{g_2} = \frac{4F_2^2(M_2+1)^2+1}{4F_1^2(M_1+1)^2+1}. \tag{4.3}$$

The ratio is calculated for each configuration pair using equation 4.3. Figure 4.9 shows the ratios obtained experimentally and theoretically, which are in good agreement. In other words, the light source is approximately a Lambertian one and can be fed into the diagnostics setup to evaluate the optical resolution in the laboratory. The illuminated object by the source is an AF-target [80]. In Fig. 4.11, the target slits are imaged, for three configurations of the diagnostics, when the image intensifier is not employed. The sharp edge of the slits can be used to measure the image resolution. The intensity growth rate in transition from the background to the signal intensity over the sharp edge of a slit represents the optical resolution. The edge of the slit is projected and the projected profile is fitted by a sigmoid Richard's function [81],

$$y = A + \frac{B-A}{(1+Ce^{-\beta x})^{1/\alpha}}, \tag{4.4}$$

where β is a measure of the growth rate and therefore the resolution. In the diagnostics stations, the scintillator is tilted with respect to the vertical axis by 45 degrees. Thus, the more realistic condition would be created when the AF-target is tilted in the same

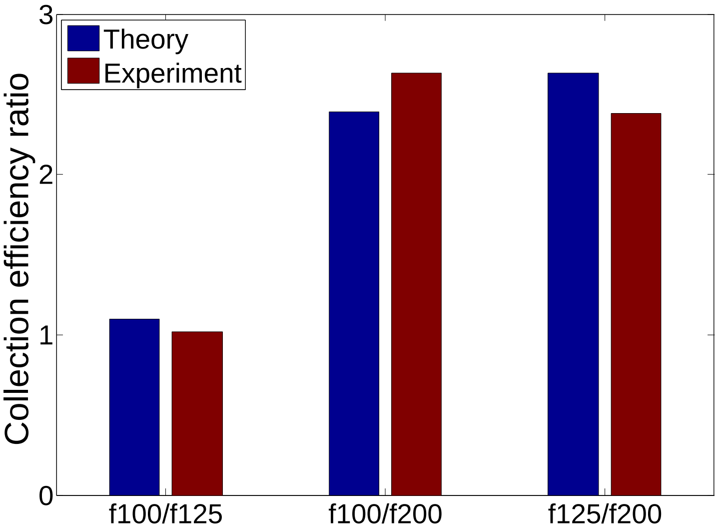

FIGURE 4.9: The coupling efficiency of the three configurations are compared in pairs. The results that are obtained experimentally and theoretically are in agreement, indicating that the diffused light is almost Lambertian.

way. Figure 4.10 shows the optical resolution as a function of the distance from the focusing point. For each configuration, the lowest value of the resolution corresponds to the image on the focused area. In order to obtain the entire resolution of the profile monitors, the scintillator and optical resolutions should be convolved. The result is shown in Fig. 4.12.

Conclusion: Combining all the simulation and measurement results, the so called "total resolution" is better than 20 μm for an electron beam of 5 MeV and scintillator thickness of 300 μm (see also. 3.4.1). However, it degrades as the energy reduces or as the thickness increases. In the above explained experimental approach, a monochromatic laser beam served as the light source. Therefore, the chromatic effects are not fully taken into account and the resolution is underestimated, accordingly. The chromatic effect of the optics can be deduced from the ZEMAX simulations and applied to the "total resolution". Therefore, as a result of chromatic aberration, the total resolution value increases as shown in Fig. 4.13. It can be concluded that the entire resolution is known to be better than 30 μm.

4.2 Further diagnostics

4.2.1 Charge diagnostics

Faraday cup: REGAE benefits from the Faraday cup concept for charge diagnostics. In the Faraday cup design a copper block is used, which also serves as the scintillator holder. Therefore, the beam charge and transverse profile are measured at the same station. The charge collected on the copper block is transferred via a

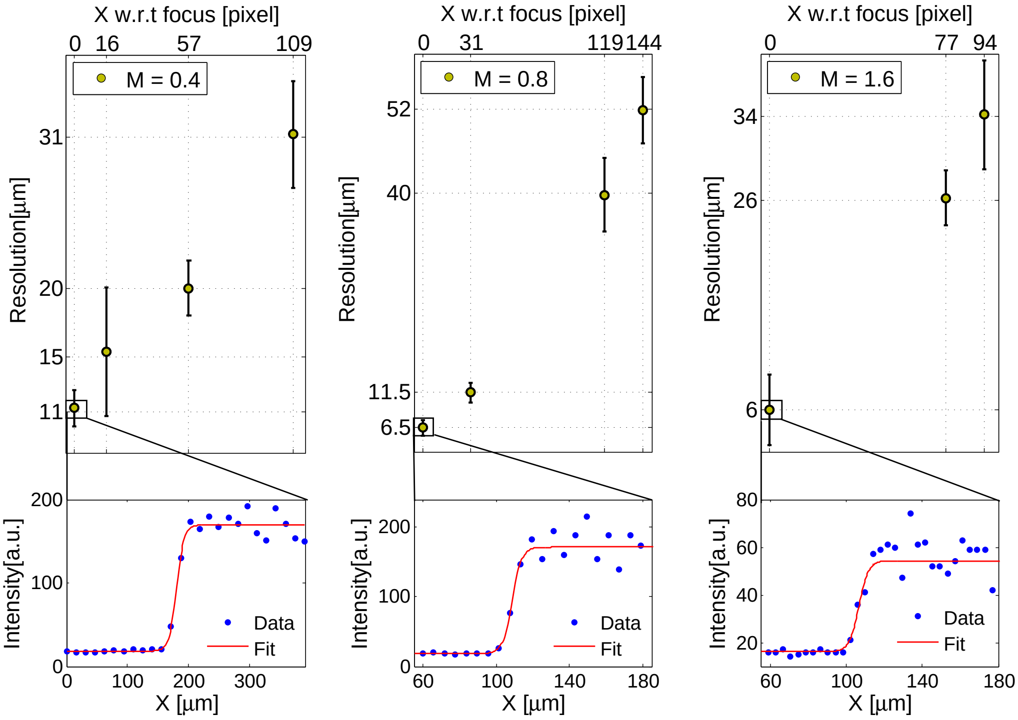

FIGURE 4.10: The resolution changes as a function of the distance from the focusing point on the tilted surface. The focused point coincides with the machine axis and scintillator center. The best measure of the beam size in the horizontal direction is performed in the middle of the screen. In case of an offset from the middle, the variation in size is derived from above. The slits located at the focusing points are projected, then the sigmoid curves are fitted to the data and the resolution is obtained.

50 Ω resistor to ground. The voltage pulse over the resistor is measured with a fast ADC. There are four Faraday cups at REGAE that are used to measure the beam charge. For these measurements, the cups give voltage pulses of about 5 ns length and a height of 33 mV/pC. Once the cup is equipped with an amplifier, the dark current charge can be measured as well. In this operation mode, a trace of 10 μs can be recorded, in total, at each RF pulse, which is fairly longer than the RF pulse duration of 4 μs. For beam charge measurement, charge ranging from tens of fC to 100 pC can be measured. More comprehensive explanations and related dark charge measurements can be found at [65].

Cavity monitor: A cavity resonator is used to measure the charge at REGAE non-destructively. The frequency of the first monopole mode occurs at 1.3 GHz, which is the RF operation frequency at FLASH and European XFEL. This device has been designed by the Machine Diagnostics and Instrumentation group (MDI) at DESY to measure the dark current at FLASH and European XFEL facilities. Since the fundamental RF frequency at these facilities are 1.3 GHz, the dark current is in resonance with the first mode of the cavity and can be measured by the so called Dark current Monitor (DaMon). At REGAE, the operating frequency is 3 GHz and consequently the dark current cannot be measured. However, the charge of

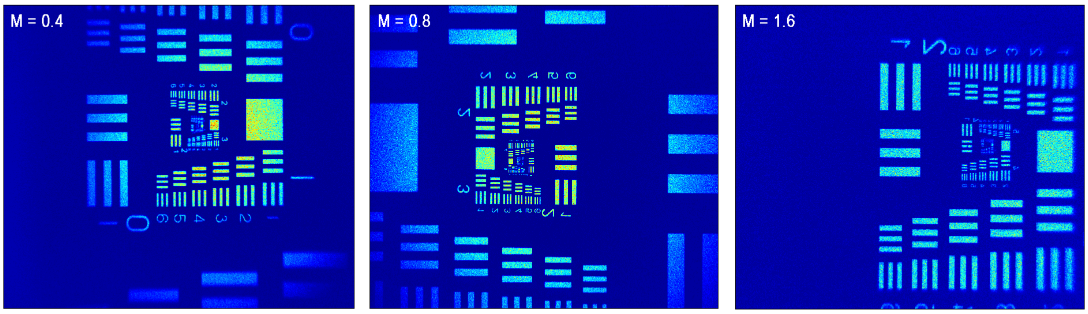

FIGURE 4.11: An AF-target is illuminated by a diffused source and then imaged by the REGAE diagnostics optical system with three different magnification modes. The detector is a stand-alone CCD. It should be noted that for the shown shots, the target is not tilted by 45 degrees and is perpendicular to the optical axis.

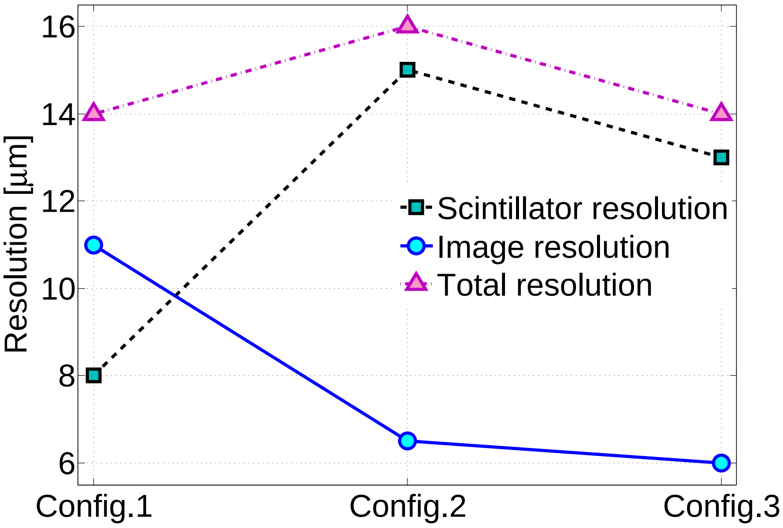

FIGURE 4.12: The image and scintillator resolution versus the diagnostics configurations are shown. The total resolution is obtained when the distributions, related to the resolutions, are convolved. The chromatic effects are excluded.

the electron beam can be monitored. The traversing bunch of electrons induces a voltage corresponding to the amount of charge. The monitor provides high sensitivity and wide dynamic range of charge measurement, such that electrons bunches of 10 fC to 50 pC can be diagnosed. For more information, see [64].

4.2.2 Energy and energy spread measurement

In chapter 2, it is mentioned that a dipole magnet is used to measure the energy and energy spread of the beam. The beam is dispersed under the influence of the magnet

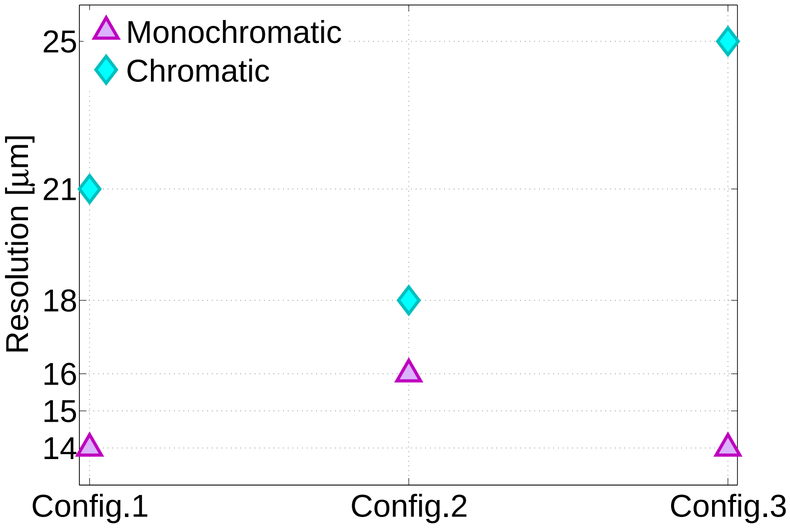

FIGURE 4.13: The monochromatic and chromatic resolutions as a function of different configurations. The chromatic resolution is a realistic measure of the entire resolution of the system. In Config.1 and Config.3, where more lenses are used, the chromatic aberration affects the resolution more.

by 90 degrees and is monitored by the diagnostics setup at DC3. The momentum of the beam can be derived using Eq. 2.6. An online measurement of the beam momentum is implemented in a control panel, the so called DC3 panel. Adjusting the current of the magnet, the beam should be located in the middle of the scintillator screen for a fine energy measurement. The traversing beam after the dipole magnet is stretched in the x-direction as a result of the existing momentum spread. The extension of the beam in this direction can be measured, once the magnification of the setup is known. In table 4.5, calibration factors, return the energy spread based on number of occupied pixels of camera, are given.

TABLE 4.5: The camera pixel has been calibrated to measure the beam momentum spread. The calibration factors are given in this table.

Configuration #	**Calib.value[pixel/keV]**
1	5.7
2	12
3	23
4	2.7
5	5.7
6	11

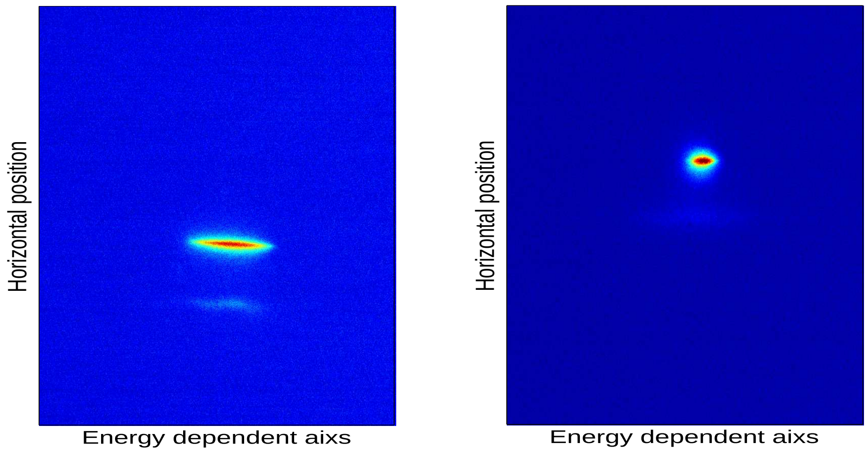

FIGURE 4.14: Electron beam profile at DC3 for configuration 1 (left) and configuration 5 (right). In configuration 1 the beam spread is much larger than for configuration 2. The alignment of the beam in the vertical direction can be done by the steerers. Since the center of the camera chip is almost aligned with the center of the scintillator screen, the beam needs to be brought almost to the center. The measured extensions in the x-direction for configurations 1 and 2 have been measured to be 25.43±0.09 keV and 6.13±0.24 keV, respectively. The tilt of the screen by 45° was taken into account for this calculation. The two measurements have been done with different machine settings.

4.2.3 Laser diagnostics

The generation of the photoelectrons is assured when the photocathode is illuminated by the UV laser beam. Hence, aligning the laser beam with the photocathode is important. A scintillator cathode which has a BGO scintillator coating in the cathode area is used for this purpose. If the laser beam strikes the cathode region, the visible emission of the scintillator is detected by a color camera (JAI BB-141), which is equipped with a macro zoom lens. The setup is located at one of the crosses in DDC2. The beam size on the cathode can be estimated. In case of any damage or unexpected feature on the cathode region, the color camera can discover it. After the alignment, the scintillator cathode is switched back to the real cathode for the operation. For the layout see Fig. 4.16. Figure 4.15 illustrates the cathode area and UV laser on it.

Before coupling the laser into the vacuum, the beam is split into two arms. The main fraction of laser power goes to the cathode and the rest is directed towards a sideway camera. The camera is located outside the beam pipe on the laser table. The distances from the splitter to both the cathode and the sideway camera are equal. The sideway setup is called "virtual cathode". Indeed, the transverse beam profile on the virtual cathode resembles the profile on the real cathode. Therefore, the beam position and shape are viewed during the operation (see Fig. 4.15). A BGO crystal is placed on top of the camera chip, which converts UV into visible light, to make it detectable with the optical camera.

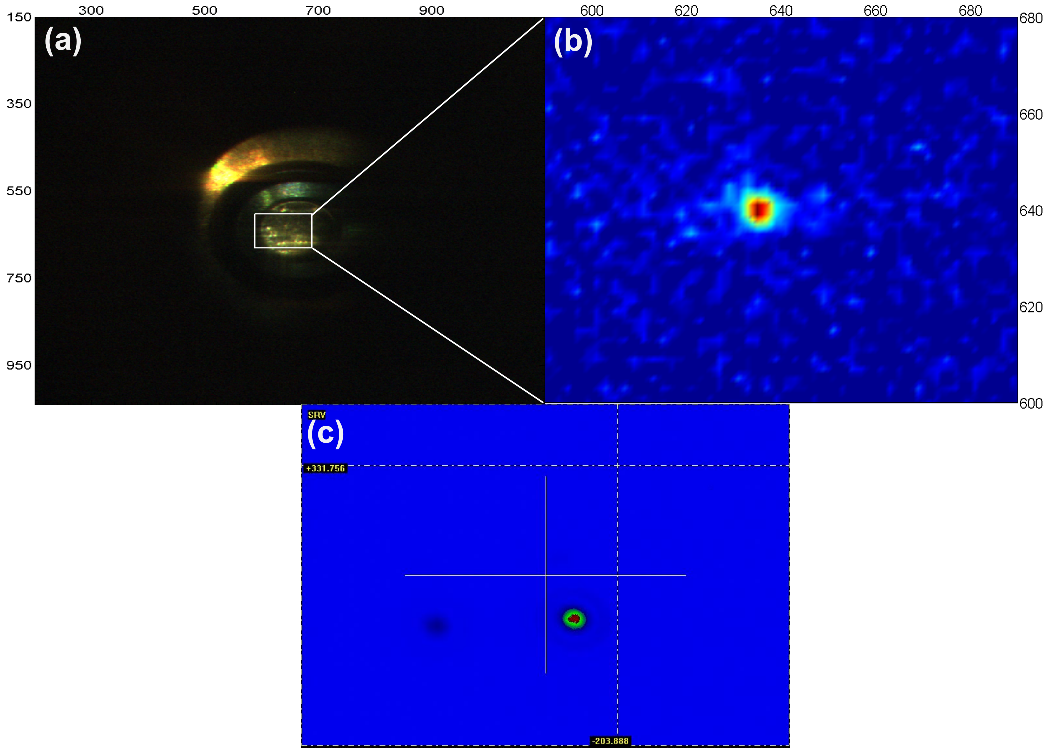

FIGURE 4.15: The laser beam transverse profile measurement at REGAE. (a) The cathode surface (inner circle) and outer region is illuminated by an LED. This shot was taken by a color camera at DDC2, hence the colors are real and any defect on the cathode area can be distinguished. The rectangle shows the area that the laser beam falls within. (b) The zoomed rectangular region, when the LED is off and laser hits the cathode area. Here the beam size is estimated to be around 100 μm. (c) The UV laser beam on the virtual cathode. This view is accessible during the operation.

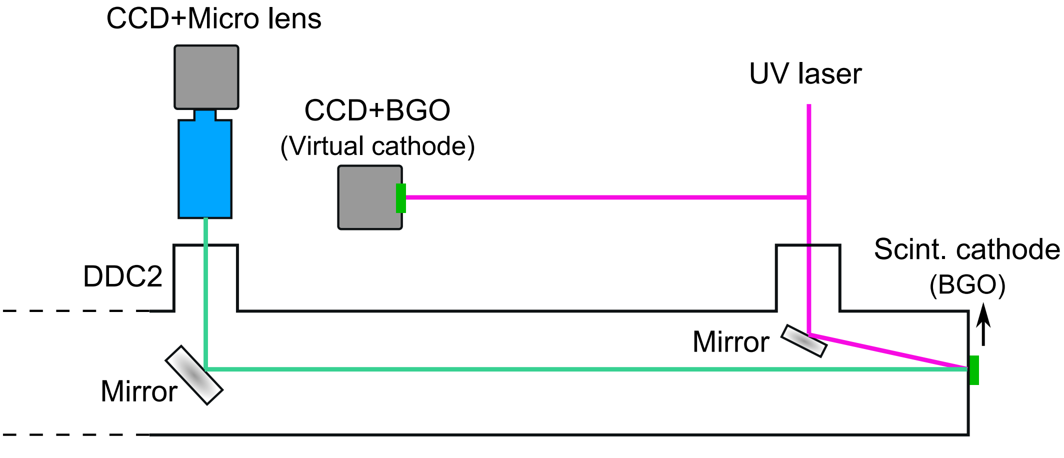

FIGURE 4.16: Layout of the laser beam in-coupling, using the scintillator cathode. The laser beam transverse monitor and its position are monitored on the virtual cathode. For the explanations see the text.

Chapter 5

Characterization of the detector

The choice of a proper detector for both the diagnostics and the diffraction detection systems is among others one of the most important tasks at REGAE. Photon imaging technology is growing very fast and it possesses a huge market, which provides various options for the users. Despite all the care spent on evaluating the suitable options, there is always room for further optimization and improvement in the post-development phases. Depending on the experiment, different approaches for detection can be considered. For instance, the camera sensitivity plays a major role in the detection of low-charge electron bunches at REGAE. The desired detector should be capable of displaying the image through the communication server, synchronous to every arrival of the electron beam, therefore a good compatibility between the machine operating rate and the detector frame rate is required. This guaranties the ability to perform diagnostics and image detection on a shot-to-shot basis, which is of great importance for the dynamic diffraction experiment. Three different detection techniques are employed in developing the beam profile monitors and diffraction detector, all based on charged-coupled device (CCD) technology [82, 83]. However, as the beam line extends for the TEM experiment (see chapter 2.8.1), another detector is needed. A scientific Complementary Metal-Oxide-Semiconductor (sCMOS) technology [84, 85] is utilized for this purpose. In this chapter, the operating principles of those CCD based detectors, normal CCD, intensified CCD (ICCD), Electron-multiplying CCD (EMCCD) and also sCMOS are explained. Moreover, evaluation results, as well as advantages and disadvantages associated to these types of detector for specific studies at REGAE are presented. Possible alternatives are also discussed.

5.1 CCD

5.1.1 Operation principle

Due to the illumination of a silicon substrate with light (300 nm–1100 nm), electrons are generated through the photoelectric effect. The absorbed energy lifts an electron from the valence band to the conduction band. The CCD consists of a large number of small, light-sensitive areas, known as pixels. They are arranged horizontally in rows and vertically in columns and can be used to form a two-dimensional image of an object. Due to the applied voltage to the structure of each pixel, free electrons can be generated and held in a potential well until the end of the light exposure. By manipulating the voltage, the stored charge in the pixels is electrically shifted in the vertical direction from one pixel to another, until it reaches to the last row of pixels, i.e. the shift register output. These pixels are not part of the CCD active area. Subsequently, the charge is shifted along the shift register and transferred to the output amplifier (gain unit). The collected charge within each pixel is measured as a voltage. The associated analog signal is converted to a digital number (DN) via an analog to digital converter (ADC) and then stored in computer memory. After the generation of charge during the exposure time of the camera, the process of vertical and horizontal charge transfer and the conversion of each pixel's voltage to a digital signal is known as the readout procedure of the CCD camera (see Fig. 5.1). The shorter time the readout takes, the faster the camera is. One major feature of a CCD, that affects the image visibility, is the gain of the detector. The gain of a CCD represents the conversion factor from number of photoelectrons to ADC units. A CCD gain of 10 (e^-/ADC) means that 10 photoelectrons correspond to one unit of digital number. If the same unit is specified for lower (higher) number of electrons, it means that the camera gain is increased (reduced). The gain value usually can be set through the CCD software. The ability to discriminate between different pixel counts, depends on the resolution of the digitizer and the gain of the device. A digitizer with higher bit depth, provides a better resolution.

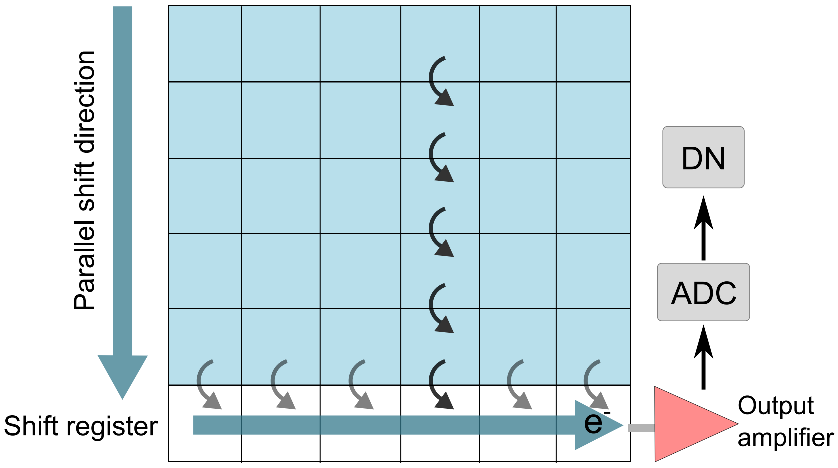

FIGURE 5.1: Schematic of CCD operation principle.

5.1.2 CCDs at REGAE

The currently operating CCD detector for diagnostics at REGAE is a normal monochrome CCD, JAI-BM141. This camera was selected among three available options that were integrable to the DESY control system. Prosilica GC655 and Prosilica GC1380 [86] were the first available cameras to be examined. The GC1380 is characterized by a higher sensitivity. In order to have an idea about the noise component, dark frames (closed camera cap) for both cameras were recorded. The frames are depicted in Fig. 5.2. A columnar pattern located at the left side of the Prosilica GC1380 is easily resolvable. The company, Allied vision, claimed that this feature is a general failure of the cameras equipped with a Sony ICX 285 sensor. Referring to the Sony sensor data sheet, it was concluded that the columnar pattern could be related to a voltage variation caused by the vertical register high speed transfer [87]. The company could not offer a GC1380 without this failure. In Fig. 5.3, two shots of the same signal are illustrated with both Prosilica GC655 and Prosilica GC1380. In order to avoid the inherent unwanted feature of the Prosilica GC1380's chip, a region of interest free of that was defined. From the shots, one can conclude that the detection performance of Prosilica GC1380 is superior.

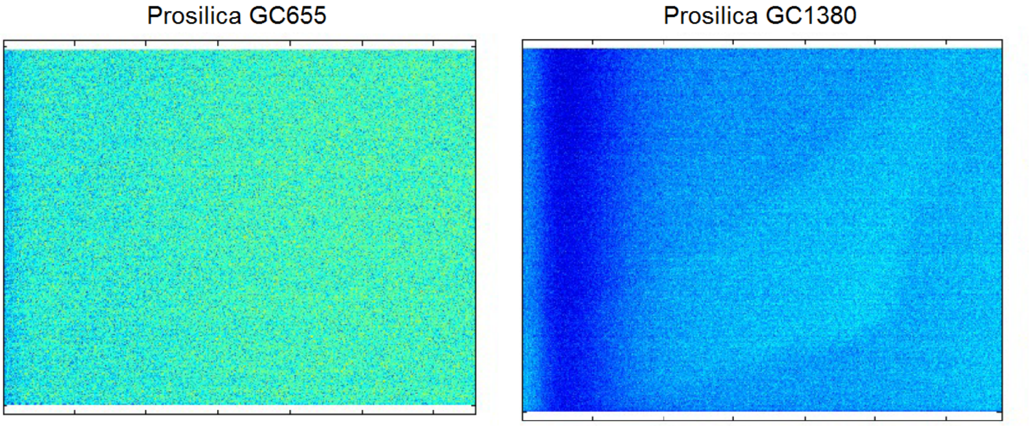

FIGURE 5.2: Dark frames of Prosilica GC655 (left) and Prosilica GC1380 (right).

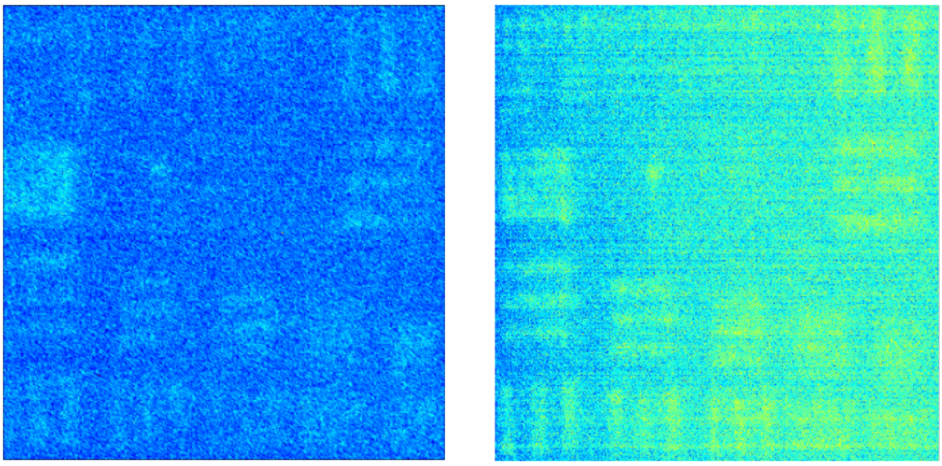

FIGURE 5.3: Signal frames of Prosilica GC655 (left) and Prosilica GC1380 (right).

JAI BM-141 was also examined for the purpose of diagnostics at REGAE. The same sensor, ICX 285, is used in the camera, but the permanent columnar structure was not observed on it. Consequently, they were installed and are used for REGAE diagnostics up to present. The proper choice of the sensor guaranties the excellent sensitivity and spectral response of the detector. Later, another promising option, Sony XCG-H280E [88], became available to be inspected and compared to JAI BM-141. The XCG-H280E incorporates a 2/3-type EXview HAD II CCD Sensor, providing great capability of capturing clear images in low-light environments [89]. Properties of the examines CCDs are presented in table 5.1.

Table 5.1: Specifications of the four different CCD types.

Type	**Prosilica GC655**	**Prosilica GC1380**	**JAI BM-141**	**Sony XCG-H280E**
Image sensor	Sony ICX414	Sony ICX285	2/3-type ICX285AL	2/3-type IT PS CCD
Active pixels (H×V)	659×493	1360×1024	1392×1040	1920×1440
Pixel size [μm]	9.9	6.45	6.45	4.53
Standard frame rate [fps]	90	20.2	30.12	32
Exposure time	10 μs–116.8 s	10 μs–116.8 s	63 μs–2 s	10 μs–2 s
Gain [dB]	0–22	0–27	-6–24	0–18
Operating temperature [$^{\circ}C$]	0–50	0–50	-50–50	-10–50
Image output	8-bit, 12-bit	8-bit, 12-bit	8-bit, 10-bit, 12-bit	8-bit, 10-bit, 12-bit

The standard frame rate is the maximum achievable rate in normal operation, in which all pixels of the chip are involved in the readout procedure. One can increase the frame rate by defining a specific region on the chip for reading the charge, or by binning, i.e. by enlarging the pixel area. In the case of Sony, according to our experience, the frame rate can be increased up to 50 frames per second, once an external rectangular pulse triggers the camera and controls the shutter, in full resolution mode and continuous operation.

The exposure time of JAI can be manipulated via the detector software from 63 μs to 33 ms. However, when the trigger pulse width regulates the shutter (pulse width trigger mode), the exposure time can change from 63 μs to 2 s.

5.2 ICCD

The technology of ICCD has offered an excellent sensitivity for low light level detection and also a remarkable shutter speed to capture images of fast transient phenomena. An image intensifier unit is responsible for amplifying the signal much higher than the noise level. They were initially developed for night vision applications in the military, but later their application extended to various scientific fields. The amplified image is coupled to a CCD either by a fiber optic coupler or by means of lens coupling.

The operation principle of an MCP-based image intensifier is illustrated in Fig. 5.4. It consists of a photocathode, MCP plate and a phosphor screen, whose properties affect the performance of the image intensifier. The incident photons are converted to photoelectrons upon the photocathode area. A potential gradient (V_C) between the cathode and the input surface of a multichannel plate (MCP) causes the electrons to be accelerated and drawn towards the MCP by an electric field. Due to high potential difference, across the MCP, (V_{MCP}), the electrons are accelerated and collide with the MCP channels' walls. Subsequently, secondary electrons are produced resulting in an overall multiplication of the electrons in each channel. The degree of multiplication is regulated by the gain voltage across the MCP unit. The multiplied electrons reach a phosphorescence material under a potential gradient of (V_A) at the output of the MCP and are converted to visible photons. The image intensifier can be gated to open and close the optical shutter by varying the voltage between the cathode and the input of the MCP (V_C). Whenever the MCP input voltage is higher than the cathode voltage, the gate is on and the electrons are accelerated towards the MCP stage. In the opposite case, the photoelectrons move back to the photocathode surface and there is no output light during the gate-off condition. The described 18 mm MCP-based Image Intensifier tube belongs to the second generation of image intensifiers. It exploits the photocathode Super-S25, behind the input window glass, and P43 phosphorescent material on the output glass window (Bk7). The high voltage power supply provides individual voltages to control the external gain (MCP-in and MCP-out gradient voltage, V_{MCP}) and the gating (cathode and MCP-in gradient voltage). According to the intensifier's specifications, it can be gated down to 100 ns. In order to examine the gating of the intensifier tube, a high voltage probe with a bandwidth of 75 MHz was used to monitor the gating voltage from the power supply, as the TTL trigger pulse width was varied. It was demonstrated that if the trigger width is reduced to 50 ns, the gating pulse on the cathode is still appropriate to gate the unit (see Fig. 5.5).

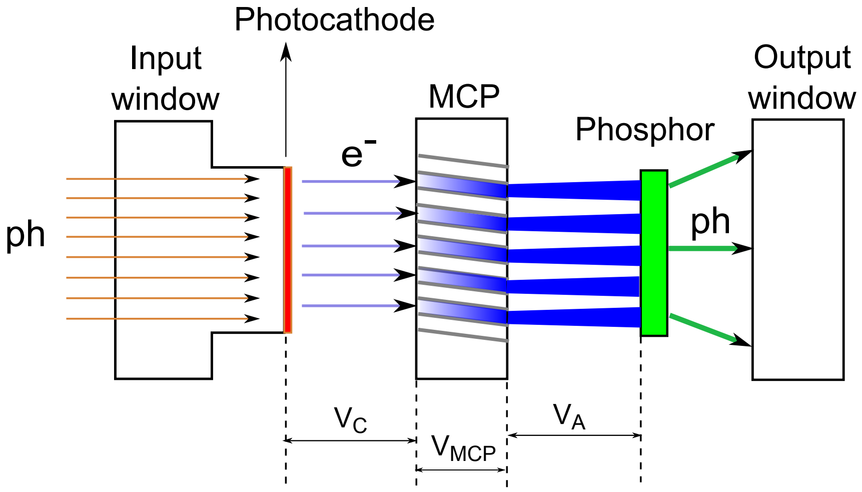

FIGURE 5.4: Schematic view of an image intensifier. In case of intensification or gate ON, the photocathode voltage is set to -200 V and the MCP-in is grounded. The positive voltage difference V_C accelerates the photoelectrons towards the MCP stage to be multiplied under the potential difference of V_{MCP}. After the MCP stage, the electrons undergo acceleration as a result of positive voltage difference, V_A, reach to the phosphor and are converted to visible photons.

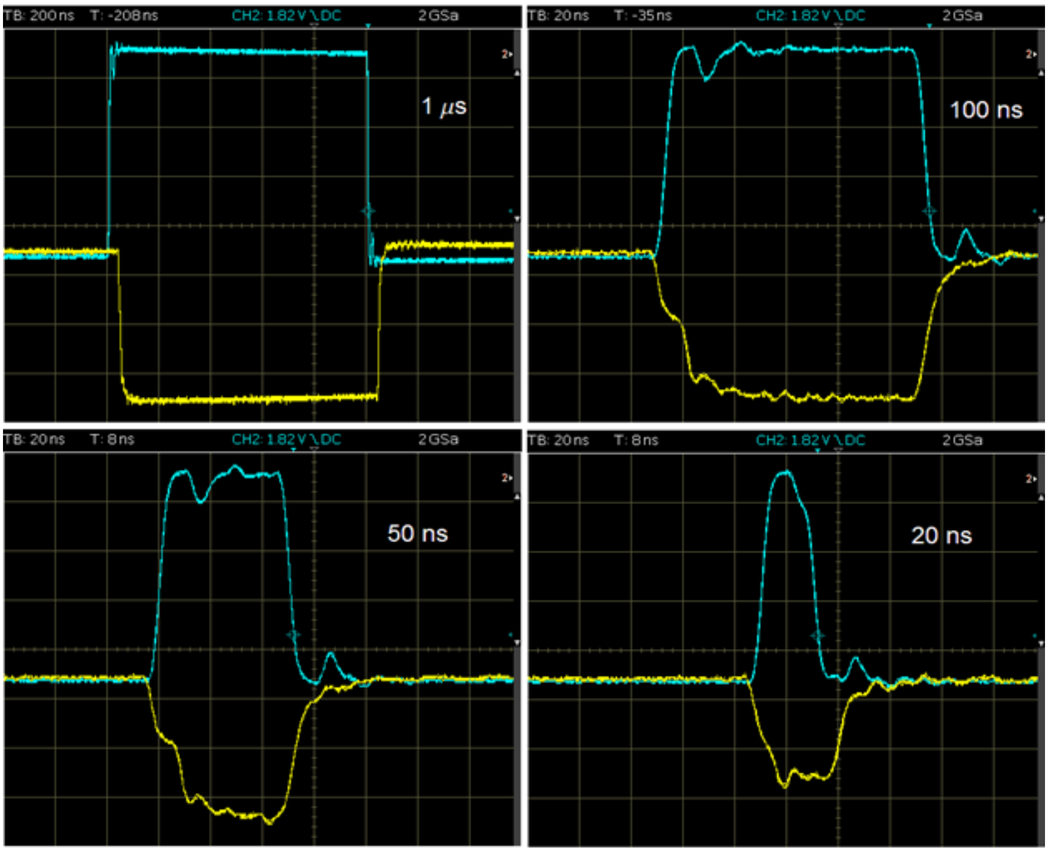

FIGURE 5.5: Traces of external trigger pulse (positive) and the intensifier cathode voltage, V_C (negative). The trigger pulse introduces the gating window of the intensifier. According to the specifications, 100 ns is the minimum timing shutter, but the oscilloscope trace shows that with 50 ns the gate window follows the trigger pulse satisfactorily. This is not the case for 20 ns.

5.3 EMCCD

EMCCD technology is a digital scientific detector innovation, first introduced to the imaging community by Andor [90] in early 2000 [91]. EMCCD shares an almost similar sensor architecture with normal CCD. Unlike conventional CCDs, the shift register of an EMCCD is extended by a so-called multiplication register unit. It consists of hundreds of stages, in which electrons are multiplied due to charge transfer. Subsequently, secondary electrons are generated (EM gain) as a result of impact ionization. The voltage applied on these stages and consequently the EM gain can be adjusted via the detector software. A simplified sketch of an EMCCD sensor is depicted in Fig. 5.6. With the introduced technology, a high quantum efficiency (QE) is achieved and the readout noise (see chapter 5.5) is significantly overcome by the amplification of the weak signal. Moreover, with an enhanced thermoelectric cooling system [92], the dark current noise (see chapter 5.5) can be suppressed to negligible levels. Accordingly, an EMCCD offers an excellent level of sensitivity, which suffices for single photon detection. At REGAE, an ANDOR EMCCD, iXon3-888 (DU888-DC-BV), has been selected as the diffraction detector. Besides an outstanding performance at low-light level, it provides a large dynamic range, sufficient for both accumulative and single shot studies. Some specifications of this detector are presented in Table 5.2.

TABLE 5.2: Properties of ANDOR iXon3-888 EMCCD.

QE	93%
Active pixels (H×V)	1024×1024
Pixel size [μm]	13×13 (W×H)
Standard frame rate [fps]	8 @14-bit, 1 @16-bit
External exposure	down to 1 μs
Read noise (e^-)	<1
Max. readout rate [MHz]	10
Cooling	-70°C air-cooled, -90°C water-cooled
Image output	14-bit, 16-bit

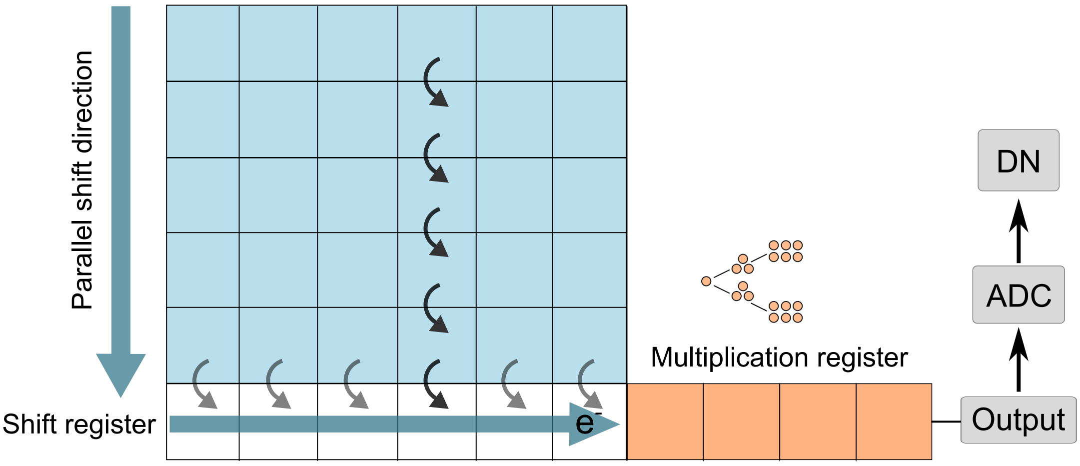

FIGURE 5.6: An electron multiplying built structure, added to the shift register to create the EMCCD chip.

5.4 sCMOS

The existing camera of this type at the REGAE laboratory is one of the most promising photon detectors, being capable of combining the features of ultra-low noise, extremely rapid frame rates, wide dynamic range, large field of view and high-resolution. Neo sCMOS from ANDOR exploits the CMOS sensor technology. In contrast to the CCD chips, CMOS contains conversion electronic built into every pixel. In general, this system benefits from a faster readout, less power consumption and lower readout noise. When light strikes the photosensitive arrays of the pixels, electrons are released. The photoelectrons are converted to analog signals inside each pixel's amplifier. The pixel's voltage is then transferred to the row of ADC units, in which they are converted to digital signals. Figure 5.7 shows the layout of a CMOS chip. Finally, the digitized numbers are read out. Since the readout noise is significantly reduced, the main attention is drawn towards the dark noise. A thermoelectric cooling system suppresses the dark current noise remarkably. The Neo camera offers two types of readout mode: Rolling Shutter and Global Shutter [93]. In Rolling Shutter mode, the charge transfer happens on a per row basis while in Global Shutter, charge transfer happens for the whole sensor or globally. The case of study determines which of the two options is applied. While Rolling Shutter offers a lower readout noise, it results in some limitations of short exposure times. In Table 5.3, the specifications of Neo sCMOS are given.

TABLE 5.3: Specifications of the ANDOR sCMOS, Neo.

QE	57%
Active pixels (H×V)	2560×2160 (H×V)
Pixel size [μm]	6.5×6.5 (W×H)
Standard frame rate [fps]	Sustained: 30, Burst: 100
External exposure	down to 1 μs
Read noise (e^-)	1
Max. readout rate [MHz]	560
Cooling	-30°C air-cooled, -40°C water-cooled
Image output	11-bit, 16-bit

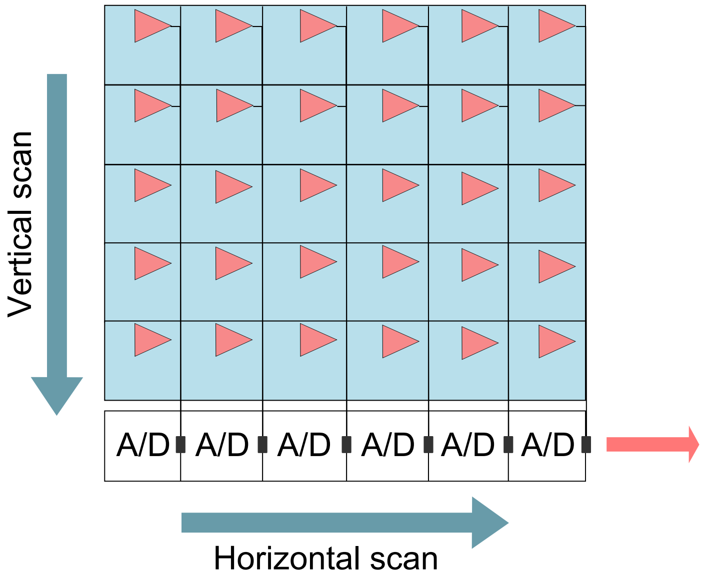

FIGURE 5.7: Schematic of CMOS sensor describing the operation of the structure.

5.5 Comparison of the detectors

The silicon-based detectors are expected to have three different noise contributions: shot noise (photon noise), dark noise and read noise. The shot noise is the inherent variation of the incident photons flux. The interval between photon arrivals follows Poisson statistics and the corresponding photon noise is equivalent to the square-root of the signal. Due to a high temperature, electrons gain sufficient energy to leave the valence band and become free. They are then collected by the potential well of a pixel and create the dark current. Since the contribution follows Poisson statistics, the dark noise is equivalent to the square-root of the number of thermally generated electrons during the exposure time. The read noise consists of two independent noise components: the first is induced by the electronics, which introduce spurious electrons into the process, and the second contribution originates from the analog to digital conversion process [94]. In low-light level detection, shot noise is expected to impose a negligible influence in the overall noise. Therefore, the dark noise and the read noise, which are considered the systematic noises, have the major contribution. The ability of a detector to suppress these noise components, partly qualifies the device for low-intensity detection purpose.

By means of a thermoelectric cooling system, the dark current noise in the EMCCD and sCMOS detectors is significantly suppressed, while in the Intensified CCD and the CCD, the operating temperature can reach up to 50°C. Since each pixel has its own individual readout structure, the overall read noise in the CMOS sensors is lower than in the CCD sensor. In the EMCCD and the ICCD, which exploit the CCD architecture, the weak signal is multiplied above the detector read noise. Although the degree of multiplication depends on the introduced gain value, the amplified signal dominates the read noise. However, fluctuations of the multiplication process in ICCD and EMCCD, introduce an extra factor of noise or uncertainty.

The detection sensitivity is another important issue, when a low-light level needs to be dealt with. The iXon EMCCD is the most sensitive detector at REGAE because of its excellent QE, as well as the on-chip electron multiplying feature. The home-made ICCD, which employs an MCP-based intensifier unit, yields a high degree of sensitivity. One criterion to evaluate the image quality or the detector performance is signal-to-noise ratio (SNR). It describes the average signal strength relative to the pixel-to-pixel variations in the selected signal region,

$$SNR = S/\sigma_{sig}. \tag{5.1}$$

A high signal strength, as well as small contribution of the overall noise (shot noise, dark noise and read noise), result in a good SNR value. The performance and sensitivity of JAI BM-141, Sony XCG-H280E and ANDOR Neo have been compared to each other, by measuring the related SNR (see section 5.6).

At REGAE, the electron beam with a maximum length of 1 ps lies within the 6 μs-long RF pulse. It is desirable to shorten the window of the detection as much as possible, to avoid the undesired contribution of the dark current, which is caused by the high RF acceleration field. Among all the detectors, the shortest detection window is achieved by the home-made ICCD. Indeed, in the ICCD structure the image intensifier is gated down to 50 ns, while the CCD exposure is extended to 2 ms to be able to capture the entire decay component from the intensifier phosphor. In case of the other detectors, the exposure times are set to the respective minimum value.

The necessity of performing shot-to-shot measurements for diagnostics and detection at REGAE has been already pointed out (see chapter 4). This machine operates with maximum rate of 50 Hz. Hence, the detector frame rates should become compatible to the machine repetition rate, specifically for the time-resolved experiment. ANDOR Neo is the only available camera, which is capable of accomplishing the maximum rep-rate. After communicating with the video server, the JAI BM-141 has reached a frame rate of 12 Hz, which is in good agreement with the current machine operating rate. According to the ANDOR EMCCD specifications, not the detection of every shot but the selective single shots detection can be achieved with this detector.

5.6 Camera evaluation

The used cameras at REGAE have been inspected separately in the laboratory to create an opportunity for a more rigorous characterization. The main idea for this experiment is to use a light source with a known flux for two main purposes. First, calibrating the cameras to find a relation between the integrated camera counts and the photon intensity and as a second step to compare the performance of detector pairs in terms of sensitivity. The layout of the experiment is shown in Fig. 5.8. A diode laser, supplies the required source of light in the experiment. In order to couple a parallel beam directly to the camera chips, the laser beam is attenuated and also enlarged in the transverse plane. A telescope structure (inside the tube) along the beam path, increases the beam diameter and consequently reduces its intensity. Further attenuation can be done with neutral density filters. One set of filters is placed inside the lens tube for permanent attenuation. The intensity of the overall system can vary by means of adjustable filters in front of the laser. The beam is brought to a splitter, divided into two arms, specified for two different detectors. It is then directly coupled to the camera chips. An iris at the end of the tube adjusts the beam diameter to fit it to the camera chips. Although the beam splitter is supposed to split the beam equally into two paths, the intensity of the transmission arm is slightly higher than the reflective arm. That adds more complication to these comparative experiments. However, the power and consequently the photon flux of each path is measured and a correction is applied to the results, accounting for the difference in the intensity of the two arms. Since the measurement deals with low-light intensity, the isolation of the setup from the background light was essential. As shown in Fig. 5.8, three light-tight boxes enclose the entire setup to prevent penetration of the undesired background component. Figure 5.9 demonstrates the elimination of the background light. The intensity of a selected area as a function of the amplifier gain is measured with and without the laser beam. The laser signal intensity increases with gain. If the dark noise is negligible, the background intensity (laser OFF) remains almost steady as the gain value changes. Then it is indicated that the background shots do not contain any signal from the environment and the setup is well isolated. Due to technical problems, the EMCCD iXon885 could not be installed and examined at the time of this experiment.

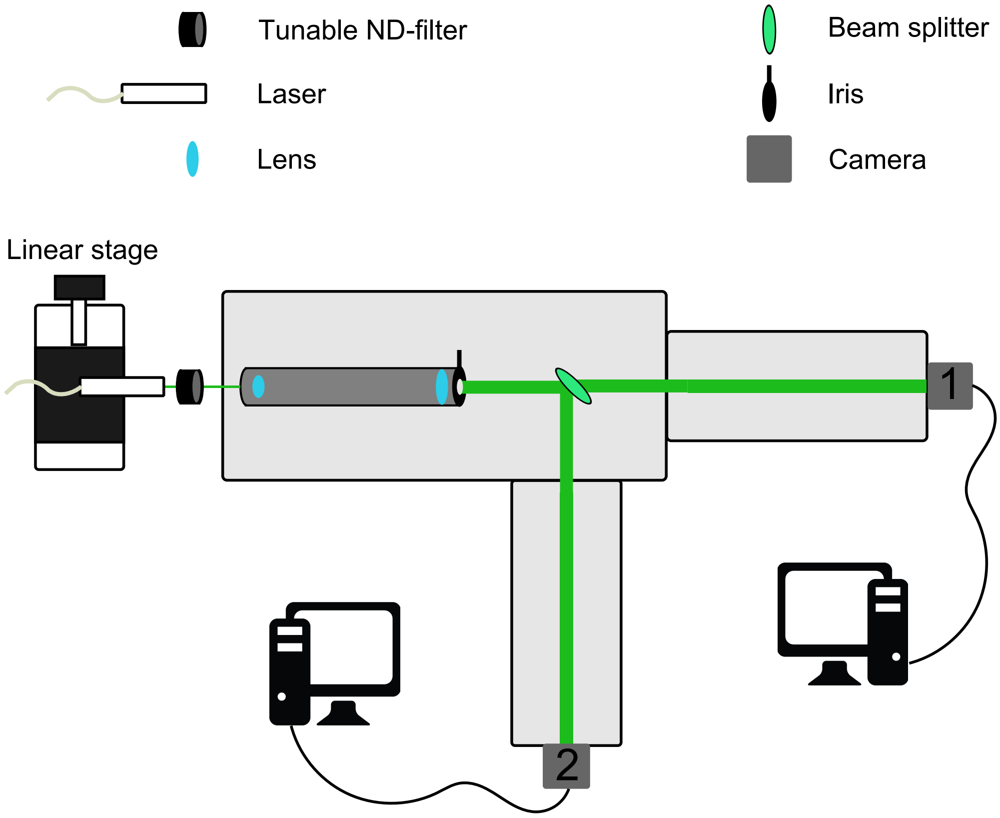

FIGURE 5.8: Experimental layout of the setup for camera calibration and evaluation.

5.6.1 Camera calibration

The camera calibration gives a conversion factor between the digitized signal value and the number of photons obtained. The number of photons hitting the camera chips is obtained from the measured power in each arm. The intensity varies when different attenuation filters are applied to the beam path. Subsequently, a relation between the number of photons and camera counts is obtained, which follows a linear behavior. The slope of the linear fit is defined as the calibration factor. This factor differs for various gain settings. The bit depth of the digitizer also affects this calibration factor.

In the JAI BM-141 software, the associated gain value is in the range of -170–700. The equivalent range in logarithmic unit is -6–24 dB. Each integer step within the entire range (870) is equal to 0.0364 dB. If an amplification of one is assigned to zero gain, the amplification factor with respect to this state is written as,

$$amp = 10^{\frac{G \times s}{20}}, \tag{5.2}$$

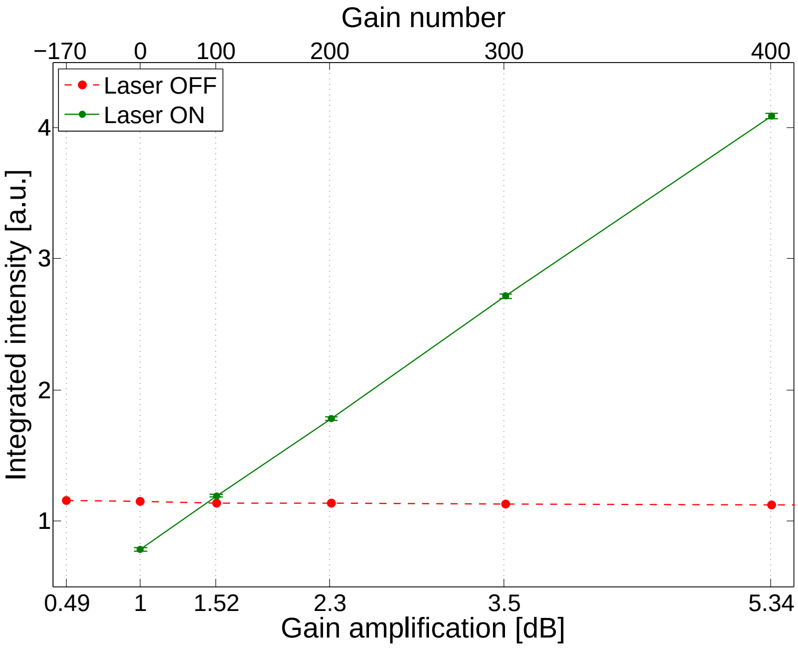

FIGURE 5.9: Intensity as a function of the JAI BM-141 amplifier gain for two states of Laser "OFF" and Laser "ON". The background is subtracted at the laser "ON" state.

where G stands for the gain value (-170–700) and s=0.0364 dB. If A (e^{-}/ADC) is the number of photoelectrons for each unit of DN at G=0, for the maximum gain value G=700, the conversion factor changes to $\sim$ A/18.8 (e^{-}/ADC), where 18.8 is the amplification factor obtained from Eq. 5.2. Subsequently, once the calibration factor at zero gain is obtained, the result can be generalized to other gain settings as follows,

$$ppp = \frac{CF}{amp} cpp, \tag{5.3}$$

where ppp is number of photons within a detector pixel, CF is the calibration factor and cpp is the count number per pixel.

With the Sony XCG-H280E, the gain value varies between 0–18 dB. The adjustable gain through the software alters in the same range, thus Eq. 5.2 can be written as,

$$amp = 10^{\frac{G}{20}}. \tag{5.4}$$

The JAI BM-141 output with pixel depth of 8-bit has been calibrated. The photon number versus the digitized count number is shown in Fig. 5.10. A linear fit gives the calibration relation to be $ppp = (97.8 \pm 1.2) \times cpp$. The errors are related to the fluctuation of the laser intensity. According to the calibration factor at G=0, the calibration relation for the whole range of gain value can be obtained using Eq. 5.3. Figure 5.11 shows the calibration plots within this range.

The Sony XCG-H280E has been calibrated separately for the two different output modes of 8-bit and 12-bit. According to the fit results, the photon number and the count

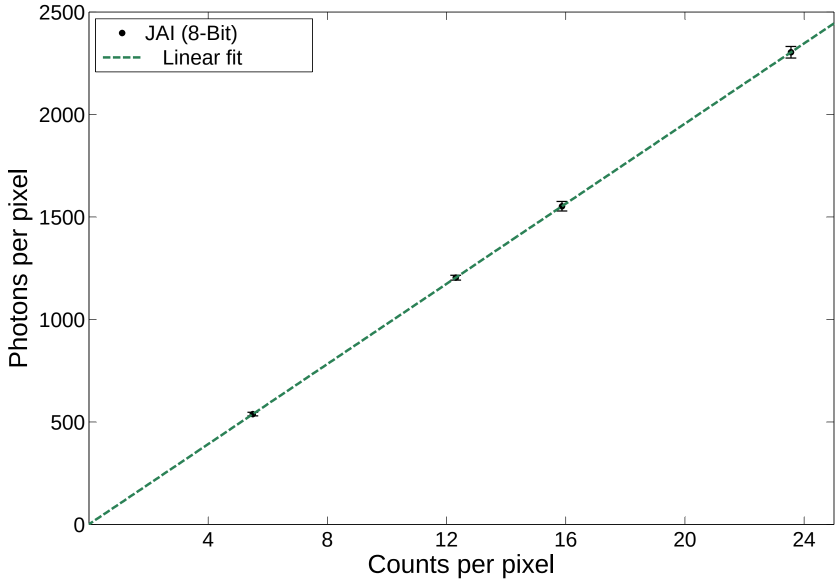

FIGURE 5.10: JAI BM-141 calibration plot at zero gain. The bit depth of the output is set to 8-bit.

in 8-bit and 12-bit are related to each other as $ppp = (89.3 \pm 1.0) \times cpp$ and $ppp = (5.55 \pm 0.07) \times cpp$, respectively. The calibration plots are shown in Fig. 5.12, Fig. 5.13 and Fig. 5.14.

The same method was applied to calibrate the ANDOR Neo. The camera does not have a variable gain and the calibration result is presented for an output mode of 16-bit (see Fig. 5.15).

The calibration of the ICCD is more complicated. Apart from the CCD gain, the intensifier gain (I-gain) should also be taken into account in this procedure. The intensifier gain is related to the multiplication factor within the MCP channels of the intensifier. The idea is to find a relation between the I-gain and the variation of the intensity, while the detector is exposed to a certain amount of light. The image intensity and the CCD gain have been already related through CCD calibrations. Therefore, if the camera gain setting and I-gain value are known, the digital number leads to the absolute number of photons. The maximum I-gain value is reached when the adjustable input gain voltage is set to 0 V. The multiplication is degraded by increasing the voltage, so that at 5 V the ICCD becomes "blind". Figure 5.16 shows the intensity of the image as a function of the intensifier gain. A logarithmic fit indicates how the intensity varies with the input gain voltage and the index of the fit function gives the rate of the change. During the experiment it was noticed that the index of the fit or in other words the relation between the intensity and the I-gain is not persistent and it is affected by the number of the incoming photons, as illustrated in Fig. 5.17. The index values are not reproducible when the measurement is repeated or when the intensifier tube is substituted by an identical one. Apart from that, for a fixed I-gain, the relation between the number of incoming photons and the intensity of the signal, is not linear, especially at larger gain factors. According

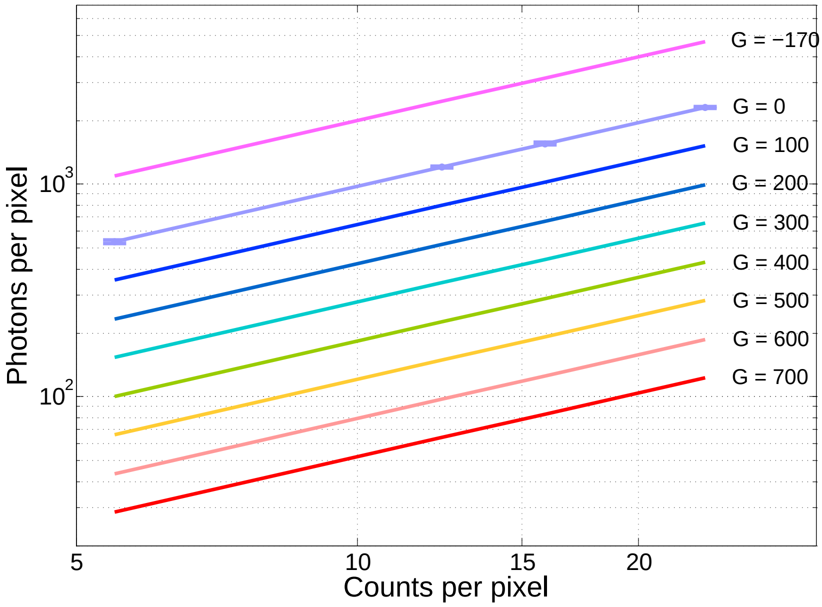

FIGURE 5.11: Calibration of JAI BM-141 extended to the entire range of gain values, -170–700. The bit depth of the output is set to 8-bit. The calibration at zero gain is obtained from the measurement and the result is extended to the entire range of the CCD gain, using Eq. 5.3. It makes it possible for the camera user to convert the digital count to photon number for a desired gain value.

to Fig. 5.18, increasing the gain factor results in a non-linear variation of the photon flux and the detected intensity with respect to each other. The observed non-linearity and inconsistency is likely to be caused by the space charge effects within the MCP channels of the intensifier. The repulsive force between the newly generated secondary electrons from the channel's wall diminishes the electric field and consequently the multiplication efficiency is affected. To this effect, we need to add the fluctuations of the multiplication and the photocathode quantum efficiency, which result in the inconsistent response of the ICCD. Because of all these reasons, the calibration of the ICCD is complicated and contains some ambiguity. Despite all complexities, for a narrow range of low intensities, the calibration appears to be possible.

5.6.2 Detection quality and sensitivity

As previously discussed, the image quality is characterized by the SNR (see Eq. 5.1). In order to obtain this quantity, it is important to select a uniform region of the image, in terms of intensity. Hence, inhomogeneities of the imaging has a negligible contribution to the denominator of Eq. 5.1. Due to the existing apertures along the beam path, the image contains some diffraction structures, which spoils the desired uniformity of the image. In the cross-comparison experiment, a good care must be taken to select the most homogeneous and uniform regions of the detected images and then obtain the

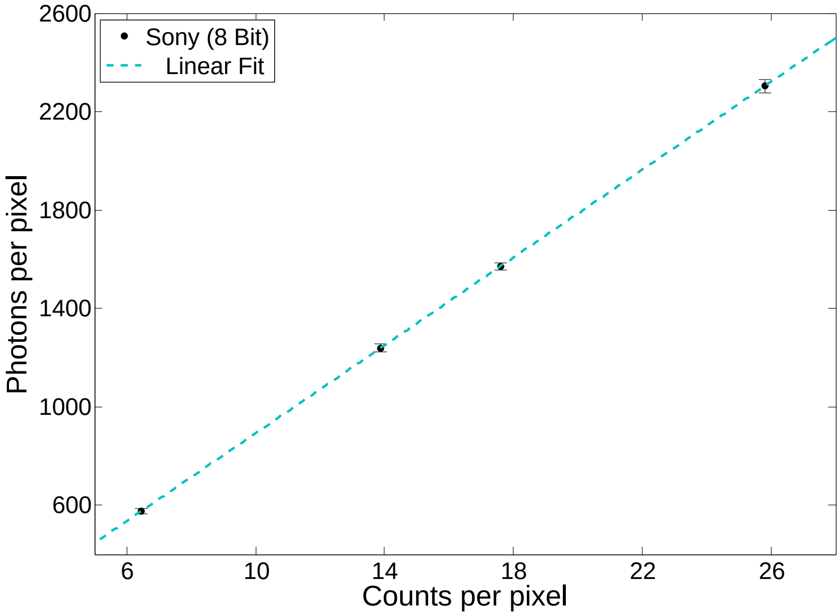

FIGURE 5.12: Photons per pixel versus counts per pixel and a linear fit, which gives the calibration factor for 8-bit output image from Sony XCG-H280E.

SNR values for each area. The JAI BM-141 has been compared against Sony XCG-H280E and also ANDOR Neo. The SNR value is the reference of the evaluation. The higher the SNR number, the better are the image quality and detector sensitivity. In the evaluating process of the JAI and the SONY CCDs, the gain is adjusted to zero. Figure 5.19 demonstrates that the SNR values associated to the SONY CCD are higher than that of JAI's. In the next evaluation, the SNR of the image for the Neo and the JAI have been obtained and the superiority of the Neo over the JAI is easily concluded from Fig. 5.20. The Neo doesn't have a gain, hence the JAI gain is set to the maximum value and the measurement covers a wide range of intensities starting from the very low light level. At this level of intensity, the contribution of the shot noise, compared to the read out and the dark current noises, becomes smaller and it has a smaller influence on the total noise and the SNR value. It can be inferred that the better performance of the sCMOS Neo is due to the suppression of the systematic noise components in the detection procedure. The SNR values at low photon intensity indicate the good sensitivity and performance of both detectors and especially of the sCMOS Neo.

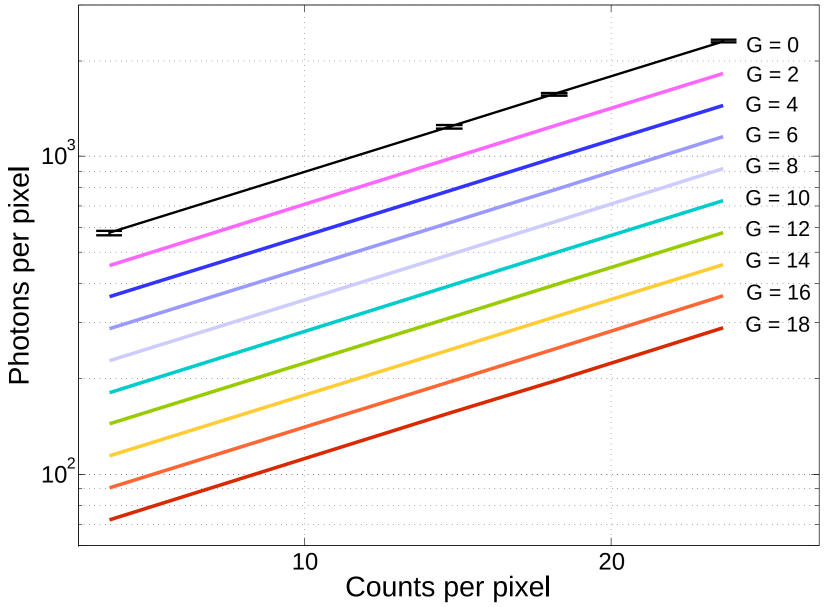

FIGURE 5.13: Applying Eq. 5.3 on the measured calibration result at G=0, the calibration factors within the gain range of 0–18 is obtained.

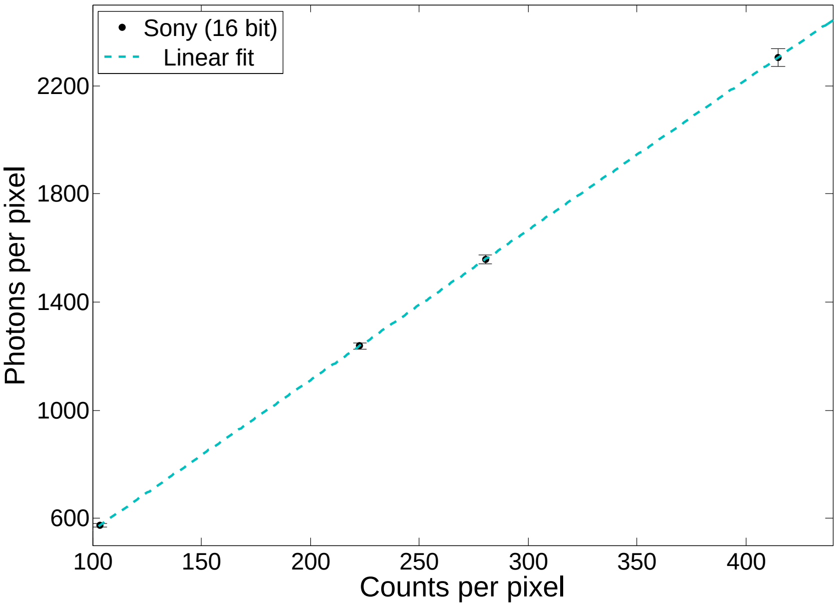

FIGURE 5.14: Photons per pixel versus counts per pixel and a linear fit, which gives the calibration factor for the 12-bit output image from Sony XCG-H280E.

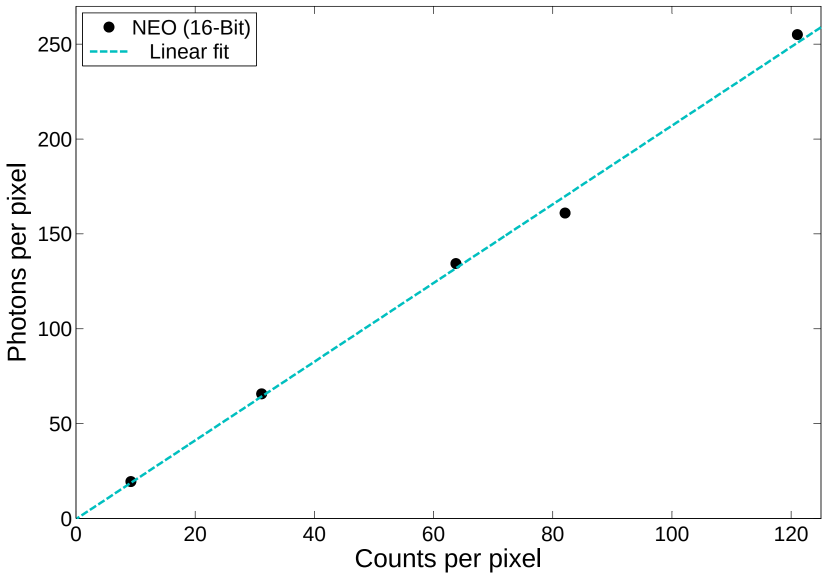

FIGURE 5.15: Photons per pixel versus counts per pixel and a linear fit, which gives the calibration factor for the 16-bit output image from ANDOR Neo. The calibration relation is derived to be $cpp = 2.1ppp$.

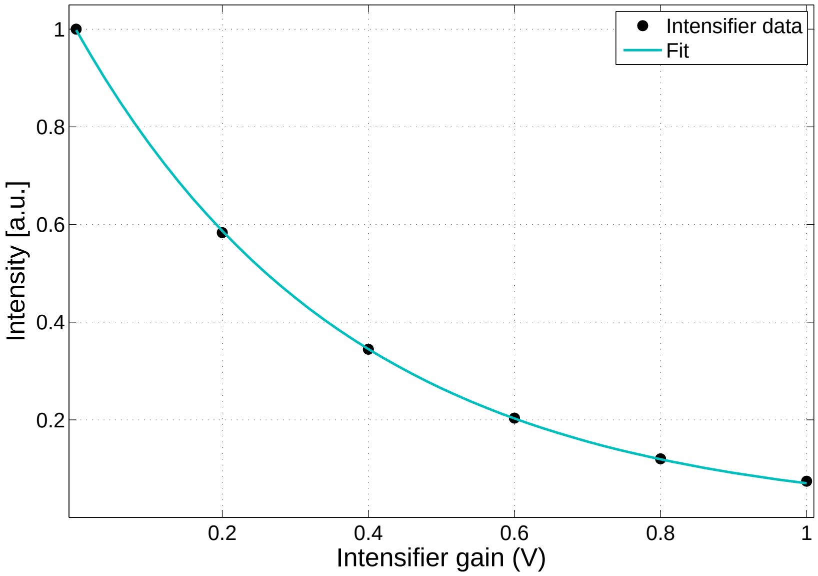

FIGURE 5.16: Integrated intensity of a selected area versus the Intensifier gain in the ICCD composition. The intensity is normalized. The CCD gain and the photon flux are constant during this measurement.

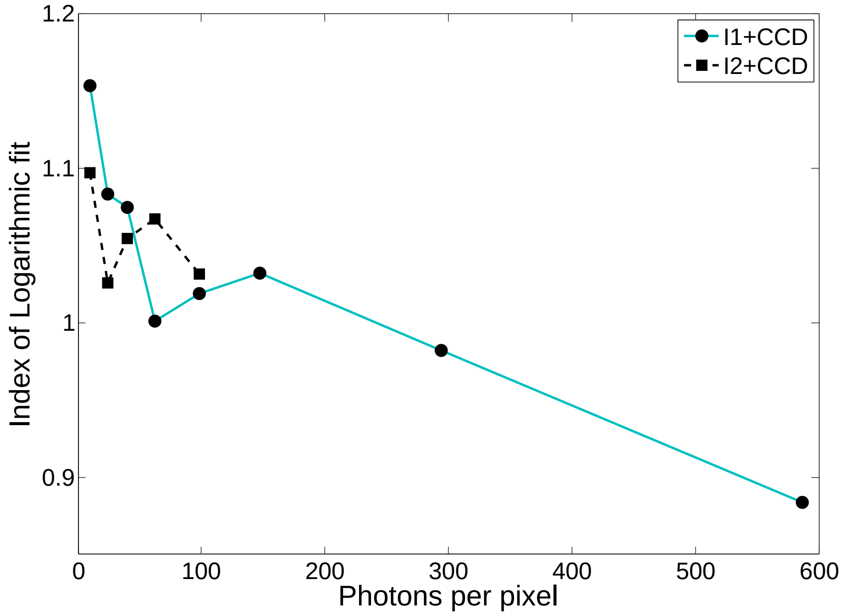

FIGURE 5.17: Variation of logarithmic fit index as a function of the photon flux. Two identical intensifier units have been used for this test and the behavior of the variation differs. Even if the measurement is repeated with the same intensifier tube, it has been observed that it does not vary consistently.

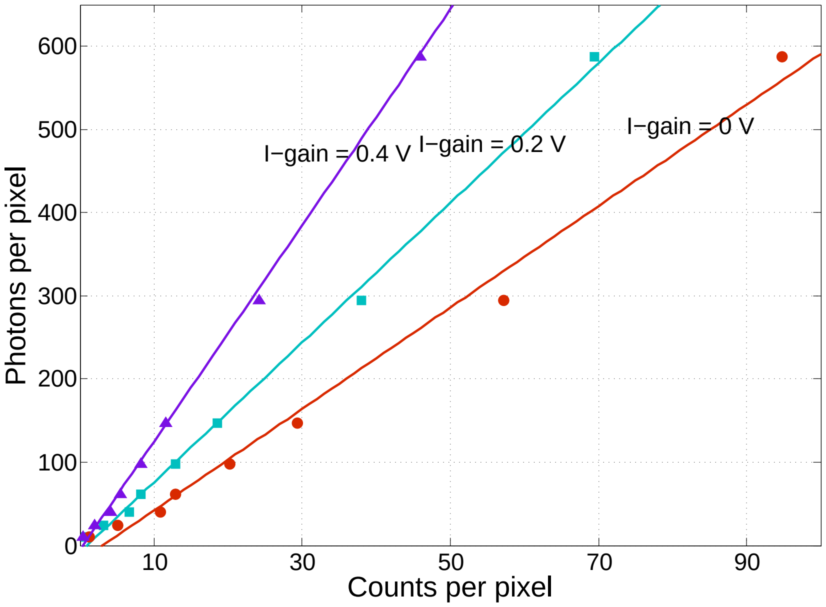

FIGURE 5.18: Photon flux versus the image intensity on the ICCD detector for three different input gain voltages and the fitted linear functions on each distribution. I-gain=0 V corresponds to the maximum intensification. Due to space charge effects, the multiplication factor degrades at higher gains and the non-linear behavior appears.

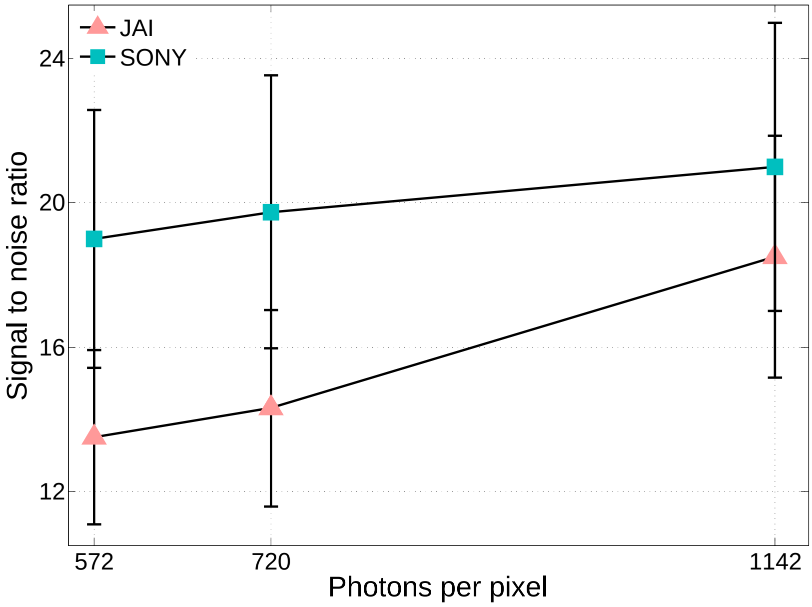

Figure 5.19: SNR versus number of photons for two JAI and SONY CCDs. The uncertainty in the SNR value from different regions on the image is shown as error bars.

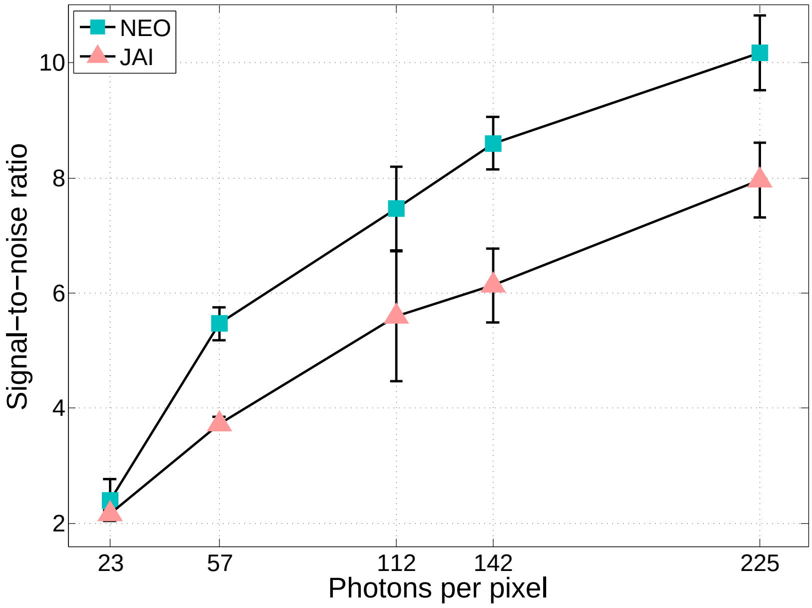

Figure 5.20: Cross-comparison of the Neo sCMOS and JAI CCD. The corresponding SNR values are shown as a function of photon intensity. The uncertainty in the SNR value from different regions on the image is shown as error bars.

Chapter 6

Measurement results

6.1 Beam profile measurements at low-charge level

During normal operation at REGAE, the charge needs to be preserved low enough to avoid space charge effects. According to the design parameters, significant compression of the electron beam to ~7 fs is feasible for the Ultra-fast electron diffraction (UED) experiment, when the beam charge is lowered to 80 fC. With proper optics and a good scintillator, any bunch of more than 5 electrons/μm^2 can be diagnosed by a stand-alone CCD achieving a reasonable signal strength. However, for the required ultra-low charge bunches at REGAE, an ICCD can be used to monitor the beam profile with an excellent sensitivity. The most sensitive existing charge monitor at REGAE is the cavity monitor (DaMon) (see chapter 3) that measures charges down to 10 fC. This sensitivity is already beyond the requirement of REGAE. As shown in Fig. 6.1, at 10 fC the ICCD monitors the beam with signal-to-background ratio (SBR) of ~16 in a single shot. The SBR is defined as the ratio of averaged signal to averaged background and describes the visibility of the signal on the detector. For the background shot the laser shutter is closed, such that the only remaining component is the RF-induced dark current. The beam profile measured by CCD and ICCD are shown in Fig. 6.1. The RMS size of the beam profile is around 150 μm. Considering a charge of 10 fC measured by Damon, one can calculate the corresponding charge in each pixel of the detector. For the CCD pixel size of 6.45 μm, the obtained value is about 40 electrons per pixel. The electron beam transverse distribution is broadened due to the scintillator and imaging resolutions, through the beam profile monitor. The overall resolution of the monitor has been measured and calculated to be better than 30 μm (see chapter 4). As a result of broadening of the profile of the beam, the quoted number of detected electrons per pixel might change. By de-convolving the spread function (resolution) from the monitored beam distribution, the broadening of the initial electron distribution is found to be negligible compared to the beam size. In other words, the measured size of the beam profile, 150 μm, represents the actual size of the electron beam. Therefore, the estimated number of detected electrons per pixel area remains unchanged.

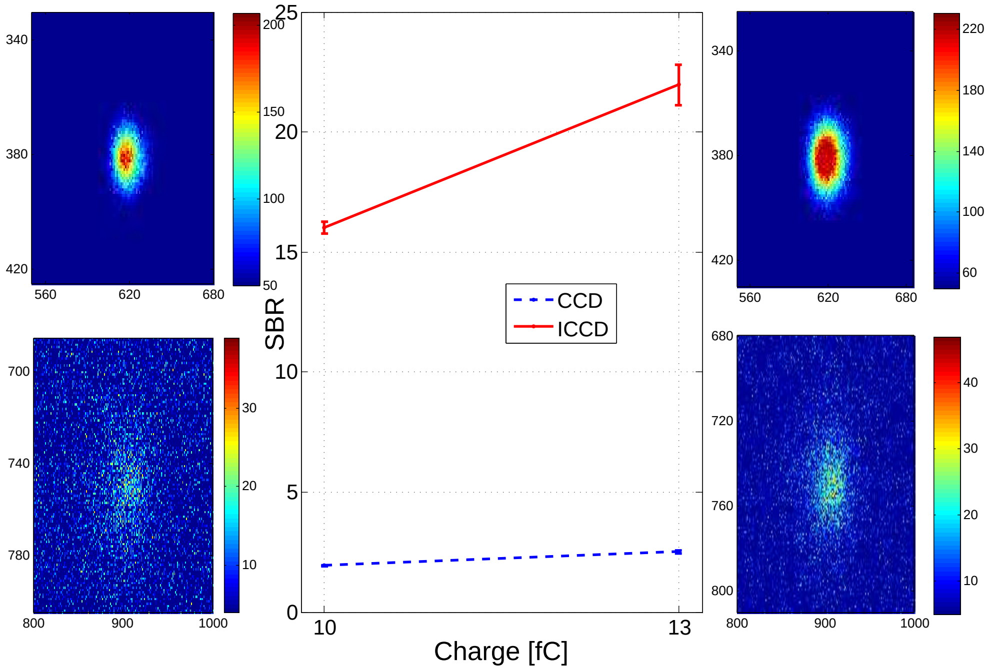

Figure 6.1: Signal-to-background ratio of the monitored beam on a CCD (bottom) and on an ICCD (top), starting from the minimum charge readout by DaMon. The remarkable performance of the ICCD in amplifying the image, makes it a suitable detector for low-charge diagnostics. Colors are not real and represents signal intensity in arbitrary units.

6.2 Beam profile monitor as a sensitive charge distribution monitor

The prominent performance of the beam profile monitor at low charges raised the idea of employing them as charge monitors. They are remarkably sensitive for monitoring low charge bunches, to which the charge monitors are "blind". Thus, the charge of each electron bunch and the projected distribution of the same bunch can be monitored at every transversal diagnostic station.

The existing charge monitors in the accelerator, DaMon and Faraday cups, are used as references to calibrate the screen monitors for charge measurements. Both the integrated intensity over the signal on the CCD and the charge as a function of the laser power behave linearly. Therefore, a linear relation between the integrated counts on the beam profile monitor and the corresponding charge measured by a charge monitor is acquired as a charge calibration. Figure 6.2 shows the charge calibration of one of the profile monitors, located at DDC2. The configuration, which applies a CCD camera as the detector has been chosen for this measurement (see Fig. 4.2). Although the charge values are high, but the calibration can be extrapolated to the very low charges, using the fit function. The most sensitive charge monitor, DaMon, is located close to the diagnostics station and is used as the calibration reference. If the detector is calibrated for the number of photons per area, an absolute charge calibration of the profile monitor is derived, in which the number of photons in a confined area of the detector represents the electron beam charge in the same area. Apart from the charge value, the calibrated beam profile monitors return the charge distribution of the electron beam.

Previously it has been shown that the scintillator emission, coupling and propagation through the optics are characterized (see chapter 4). Moreover, the normal CCD is also calibrated relative to the number of photons, using a source with a known photon distribution (see chapter 5). Accordingly, if an electron strikes the LYSO scintillator, about 100 photons enter the optics, from which 40% are transmitted through the optics of the second configuration in the profile monitor setup. If the number of photons from this estimation wants to agree with the number of photons, obtained from the direct calibration in Fig. 6.2 (e.g. @0.8 pC, the photon number value is $\sim 23\times10^6$), the quantum efficiency of the camera is around 10%. This number is close to the quantum efficiency of a typical front-illuminated CCD camera at blue wavelengths, which the peak of LYSO emission occurs [95, 96].

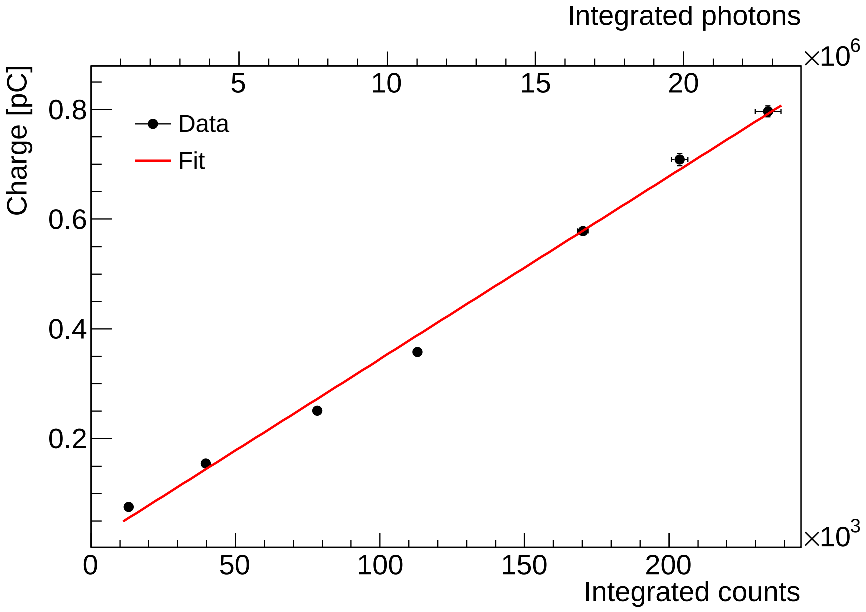

FIGURE 6.2: Charge calibration of the DDC2 beam profile monitor. The data points are fitted to a first degree polynomial $y = a + bx$, with parameters a=0.012 and b=3.33×10^{-6}. The upper horizontal axis shows the corresponding number of photons within the area of the beam.

When the diagnostics station is switched to ICCD mode, it functions more efficiently in terms of sensitivity to low intensity, however calibrating this setup as a charge monitor is not straightforward. The intensifier unit response to the charge value changes, and the integral of intensity versus laser intensity is not linear (see section 5.6.1). Figure 6.3 shows the charge growth as a function of the laser intensity measured by DaMon and the ICCD monitor. Due to saturation of the ICCD for higher charges (more than 40 fC), the charge values measured by the monitors are not in very good agreement. Thus, a calibration of the ICCD monitor should be performed for low charges.

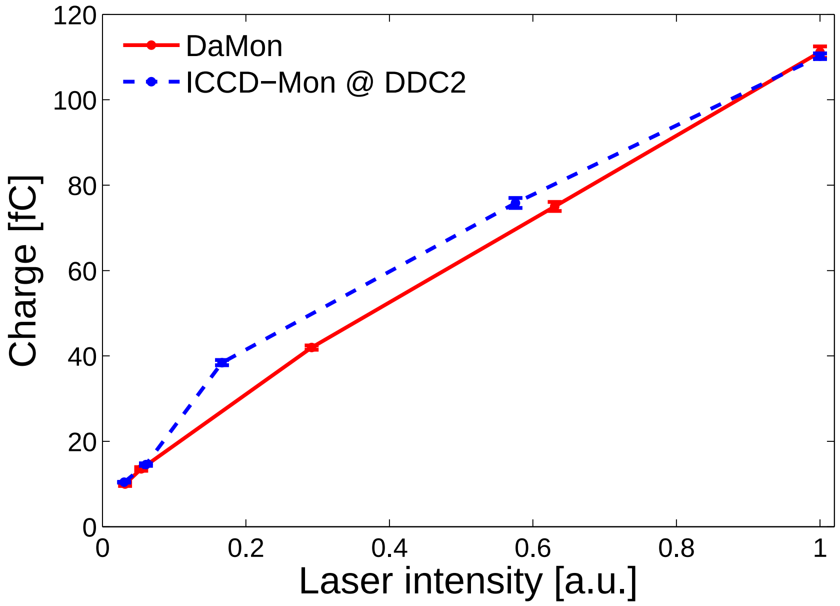

FIGURE 6.3: Charge as a function of the laser intensity, measured by the ICCD (dashed line) and DaMon (solid line) monitors located at DDC2. The error bars are related to fluctuation of the intensity from one shot to the nest one. 10 shots have been analyzed.

The profile monitors at REGAE use very sensitive photon detectors giving the possibility to resolve bunches that have a few tens of electrons per a moderate pixel size of a CCD. When this sensitivity is combined with a careful calibration, as done for REGAE, the transverse distribution recorded with the profile monitors yield a precision of several electrons per pixel, which contains more valuable information than a charge integral. For all cases that are foreseen at REGAE, this monitor gives the charge distribution with a precision down to a total charge of 10 fC or below.

6.3 Scintillator decay time measurement

The decay time of the scintillator, defined as the time interval between excitation and $1/e$ decay of the emission, is a property of the crystal that should be investigated in order to adjust a proper timing for diagnostics. The LYSO crystal decay time is quoted to be $<$50 ns, but depending on the method of crystal growth and impurities of the material, some scintillator features, including the decay time, vary significantly [97]. Therefore, the decay time of each crystal needs to be measured. REGAE operates with a maximum repetition rate of 50 Hz. The electron bunch length is below a picosecond, while dark current is emitted over a large fraction of $\sim 6\mu$s-long RF pulse. In order to remove this component from the beam profile, a fast gated image intensifier is employed, with a timing window that can be reduced down to 50 ns. Although this interval is still much longer than the sub-ps electron beam, the scintillator emission is used to monitor the transversal beam profile lasts longer than the scintillator decay time.

The decay time of LYSO was measured as follows. The image intensifier gating window, which is set to 50 ns, was shifted in steps of 10 ns from the beginning until the end of the emission. The measured variation in the intensity of the monitored beam, forms an exponential profile of the decay, shown in Fig. 6.4. From an exponential fit of the data, the decay time was found to be 45 ± 5 (syst.) ± 1 (stat.) ns. The precision of the scan steps is limited to 10 ns, adding to the systematic uncertainty in the measurement. The obtained decay time is very close to the one quoted in the literature. The analysis procedure was cross checked with a hypothetical exponential distribution corresponding to a typical LYSO emission spectrum. The integrated intensity over a time window of 50 ns, calculated in steps of 10 ns, follows an exponential distribution, which is identical to the original spectrum. Therefore, there is no overestimation of the decay time in the measurement.

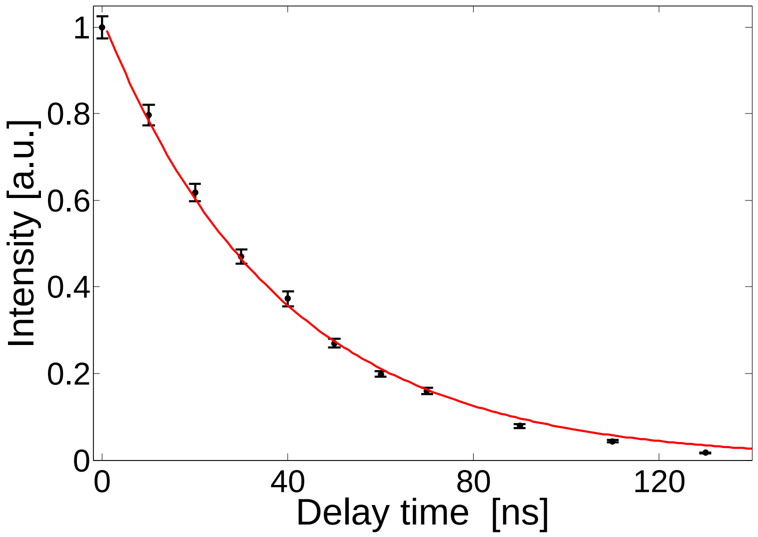

FIGURE 6.4: Decay time of LYSO scintillator. The onset time corresponds to the time where the maximum intensity starts to drop.

6.4 Suppression of dark current signal on the beam profile monitor

After characterizing the temporal behavior of the scintillator emission in the previous section, the steps toward maximal suppression of the dark current signal on the transversal profile monitors can be taken. The presence of the dark current emission is inevitable when cavities are operated at high gradients. The designed gradient to create high brightness electron source for diffraction experiment at REGAE is 110 MV/m, which is already high enough to generate an enormous amount of dark current emission. The issue becomes more sever in case of operation in low charge regime. According to the beam optics simulation, the bunch charge at the interaction point for pump-probe experiment reaches to 80 fC. Already at the normal operating charge of <1 pC, the dark current emission can dominate (depending on position and focusing condition) the beam signal and influences precise measurements, like transverse RMS beam size measurement. In case of a strong contribution from the dark current, the measured beam profile is significantly distorted. Background subtraction is one of the main approaches to overcome this problem to some extent, however suppression of the dark current before the image is digitized is preferable.

The ICCD at REGAE encompasses a fast-gated image intensifier, which can be gated down to 50 ns. Such short characteristic width of the detection window can potentially contribute significantly to the elimination of the dark current background on the profile monitor. However, one should keep in mind that the scintillation is not an instant emission process and that the rate of emission is characterized by the scintillator decay time. For the LYSO screen, the decay time was measured to be about 45 ± 5 (syst.) ± 1 (stat.) ns. This means that although the bunch length is much shorter than the decay time, the emission extends over multiples of the decay time and the optimal detection window should be chosen such that the ratio of the beam signal to the dark current background is maximal.

A bunch of electrons traveling through a scintillator medium generates a light pulse as,

$$I_s(t, t_0) = I_0 \exp(-\frac{t - t_0}{\tau}) \qquad t > t_0, \tag{6.1}$$

I_0 is the maximum of light after the emission starts and is proportional to the number of incident electrons and depends on the type of the scintillator material. τ here denotes the decay time of the scintillator, which is also a material dependent property. The entire emission is then given as,

$$S = \int_{t_0}^{\infty} I_s(t, t_0) dt = I_0 \tau. \tag{6.2}$$

The dark current emission creates a constant contribution within the duration of the RF pulse. If we approximate the RF pulse with a rectangular pulse with an interval of t_1 to t_2, the light pulse from dark current as a function of time, t, can be derived after convolution of the exponential decay with the gate pulse intensity (I_m),

$$I_{DC}(t) = \begin{cases} I_m \tau \Big(1 - \exp\big(-\frac{t - t_1}{\tau}\big)\Big) & \text{for } t_1 \leq t \leq t_2 \\ I_m \tau \Big(1 - \exp\big(-\frac{t_2 - t_1}{\tau}\big)\Big) \exp\big(-\frac{t - t_2}{\tau}\big) & \text{for } t_2 < t. \end{cases} \tag{6.3}$$

For a full flat-top RF pulse, I_m is proportional to the intensity of the dark current and scales with the emission yield of the scintillator material. If $t - t_1 > \tau$, the maximum intensity of $I_m \tau$ is achieved. Integrating for the entire emission of dark current one can write,

$$B_{DC} = \int_{t_1}^{\infty} I_{DC}(t) dt = I_m (t_2 - t_1) \tau. \tag{6.4}$$

With a fast-gated ICCD unlike a CCD, the detection time window can be considerably shorter than the dark current and with an integration time of Δt, the total dark current is written as $I_m \Delta t \tau$. In reality, the RF gate is not rectangular shaped, but the electron bunch is pushed to the flat top, which means that the dark current contribution remains constant within the exposure window. According to Eq. 6.2 and Eq. 6.4, if the exposure window is long enough (to fully contain the scintillator emission) the ratio of the charge contained in the bunch to the integrated dark current contained in the interval Δt is,

$$\frac{S}{B_{DC}} = \frac{I_0}{I_m \Delta t}. \tag{6.5}$$

For a smaller integration window, the ratio is given by,

$$\frac{S}{B_{DC}} = \frac{\int_0^t I_s dt}{I_m \Delta t}. \tag{6.6}$$

To confirm this behavior, the ratio of the beam signal to the dark current background as a function of the detection time window was investigated experimentally. The accelerating gradient is set to 65 MV/m, which corresponds to an electron beam momentum of 3.3 MeV/c. The integrated intensity of the beam and dark currents was recorded for different lengths of the intensifier gate. The delay and length of the intensifier gate can be adjusted via a timing panel in steps of 10 ns. The onset of the gate is set, such that the maximum intensity in a certain gate window is achieved. This guaranties that the zero time of the intensifier exposure coincides to the start of the scintillation emission. The initial value of the trigger pulse length is set to 30 ns and scanned to 300 ns, where the decay emission almost ends. For each gate value, two series of data are taken with and without electron beam. The images, in which the laser beam is off, contain only the dark current contribution. It is subtracted from the shot, in which the beam is also included, in order to obtain the electron beam profile. As a next step, the electron beam and the dark current signals are separated. The signal of the electron beam profile is integrated within a selected area. The region of interest is defined to be a circle with a diameter equal to the FWHM of the beam. In the shots, where the beam is blocked and only the dark current is present, the total count is obtained in an equivalent area. Each camera has an inherent offset count per pixel, which can be deduced when the camera's cap is closed. The total offset count in the selected area is subtracted from the dark current total intensity in that area. The ratio of the beam intensity to the dark current intensity can be compared within the aforementioned range of the intensifier gate. Figure 6.5 shows the integrated beam signal and the dark current background intensity for different time settings of the intensifier's gate. As expected, the signal intensity continues for a multiple of the decay time of the scintillator and then slowly relaxes. However, the dark current emission changes almost linearly, since it makes a constant contribution to the background. If the integrating widow is increased and equal to the efficient RF gate width of 2.5 μm, according to Fig. 6.5 the signal to dark current ratio converges to one. This means that there is almost no contrast to observe the signal. The total gain in the signal to dark current ratio that is achieved by shortening the gate window amounts to approximately a factor of 50, which is remarkable.

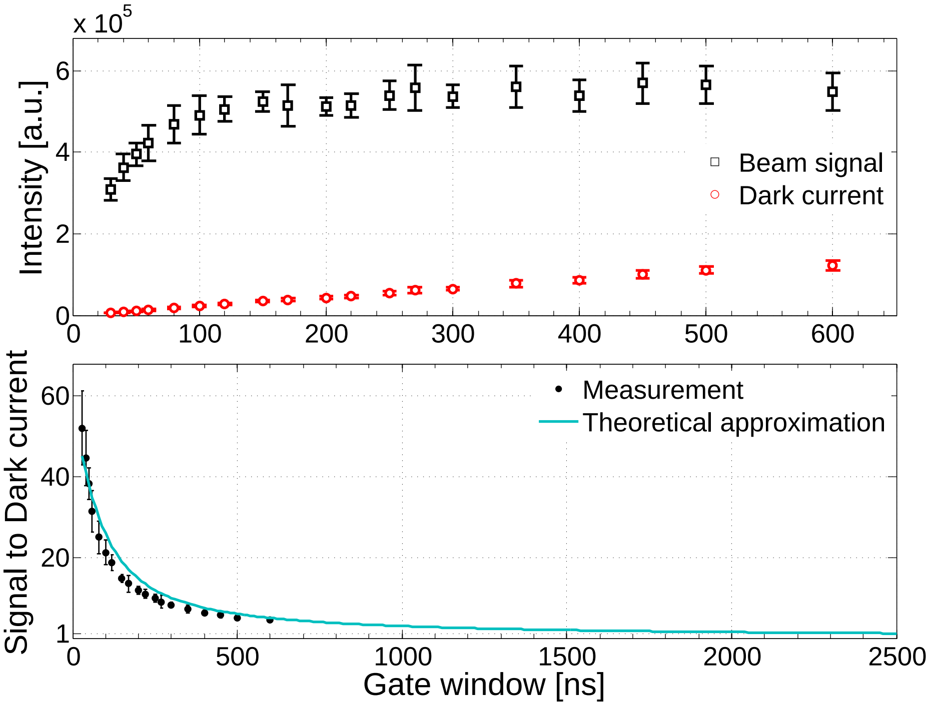

FIGURE 6.5: The electron beam profile and dark current total intensity as a function of the intensifier gate (top). The emission due to the impinging short electron bunch on the scintillator ends after ∼ 3–4 times the decay constant (150–200 ns) and from that point the integrated intensity reaches a plateau. The ratio of the signal to dark current (bottom) shows a maximum at the shortest gating time. The theoretical approximation is derived from Eq. 6.6.

6.5 Preparation for the pump-probe experiment

In a time-resolved experiment, a laser pulse, the so called pump beam, excites the sample and induces structural changes in the specimen. Synchronously, an electron beam probes the evolved spot of the specimen. Electron bunches of several femtoseconds length are required to capture the atomic motions in the transition states occurring within order of 100 fs or less. The pump and probe pulses should coincide temporally with an accuracy that falls in the femtosecond regime. Therefore, when an ultra-fast electron diffraction (UED) experiment is performed, temporal and spatial overlaps between the laser and electron beams are crucial. The main harmonic of REGAE's laser is 800 nm. The laser beam is split into two arms. The third harmonic (266 nm) of one arm is generated to hit the cathode and create the electron probe beam. The other part of the laser beam is directed onto the samples in the target chamber. Depending on the electronic property of the targeting samples, the pump beam can be generated by different nonlinear processes, such as white light generation, SHG, THG, or OPA [30]. As previously described in the diagnostics layout (see Fig. 4.1), a transversal monitor in the target chamber is used to characterize the beam transversally and to optimize it for the diffraction experiment. The transversal planes of the scintillator screen and the samples are analogous, hence the spatial overlap between the pump and probe pulses on the sample can be investigated and controlled with the scintillator monitor. For the pump-probe experiment, the sample plane is rotated by 45 degrees, so that the laser and electron beams arrive at the screen with an angle of 45 and -45 degrees, respectively. The diagnostics view port is almost perpendicular to the screen plane. The femtosecond time resolution is achieved by changing the relative time delay between the pump and probe pulses. Since the pump laser pulse is always ahead of the electron beam, an optical delay stage is used to increase the path of the laser beam line in the range of 612 mm. This is almost equivalent to a 2 ns delay in time. The precision of the motorized stage is 1 μm, which already provides sufficient resolution of the order of few femtoseconds. Another delay stage that can be adjusted manually is located in the pump laser beam line inside the laser room. This provides an extra range of 2 ns.

Due to the large uncertainties of the laser path length, the adjustment of the initial time zero needs to be performed in steps with increasing accuracy. First, the time zero, at which the laser and the electron pulses are temporally overlapped, should be determined in the target. To achieve that, the main idea is to initiate a strong process like melting with the pump laser and adjust the laser delay such that the electron diffraction pattern gets influenced by the changes in the sample. The accuracy of this method strongly depends on the characteristic length of the evolutionary process.

Apart from the transverse overlap, the transverse profile monitor can also facilitate the temporal overlap within a resolution of about 1 ns. When the overlap, with such limited precision is assured, the time zero is determined through the pump-probe experiment with a finer resolution down to picosecond or femtosecond scales. The transverse diagnostics operates in two distinct modes with a CCD and an ICCD, respectively. The image intensifier gate width of the ICCD detector is set to minimum value of 50 ns. The image intensifier gating can be used to locate the laser and electron signal in time. A layout of the experiment is depicted in Fig. 6.6. The machine signal triggers the laser pulse through the master oscillator (MO) and also a delay generator synchronously. The delay generator supplies the intensifier tube and the gating window width is adjusted to the minimum, i.e. 50 ns. There are two beam profiles on the scintillator monitor that belong to the laser pump and the electron probes. By adding an extra delay to the intensifier gate, it moves forward in time and approaches the signals. By going further in this direction, the intensity adds up. The point where the intensity starts to rise, is defined as the onset of the emission. The manual stage is used to introduce the appropriate time delay to the laser beam and adjust the overlap of the onset of the laser and electron induced emissions. Figure 6.7 shows the best possible temporal overlap between the laser and electron beam using this method. The onset of the emissions are not very sharp and can be determined with about 1 ns accuracy. Due to reflections from an obstacle inside the laser beam line, the laser shots have an inherent background, caused by the laser signal, that cannot be avoided. The image intensifier gate width is preferred to be short, but what is important for the required resolution is that the gate signal has the form of a sharp rectangle.

For this method, some points should be taken into consideration. When the electrons hit the scintillator the emission process is scintillation, while in the case of the 400 nm laser beam, the main emission process is fluorescence. Via fluorescence, the photons

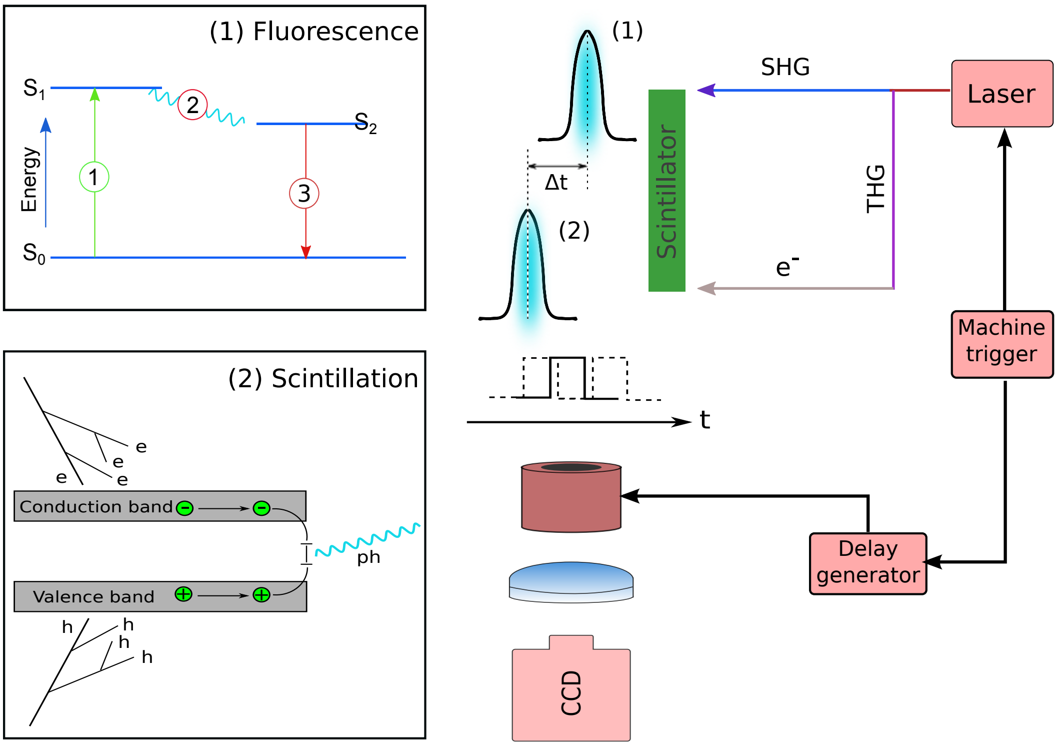

FIGURE 6.6: Layout of the experiment performed for the preparation of the pump-probe experiment. The laser beam is split into two arms. Its third harmonic (THG) is generated to produce photo-electrons and the second harmonic (SHG) is generated to trigger the dynamics in the atomic structure of the matter. The probe electron beam and pump laser pulse strike the scintillator monitor and their transverse profiles appear due to scintillation and fluorescence processes, respectively. By varying the delay of the image intensifier gate, the position of both emissions in time can be determined. The intensifier is triggered by the machine signal, which simultaneously feeds the laser equipments. A motorized optical delay stage in the laser beam line varies the relative time delay between the laser and electron beams. This stage is used to achieve the temporal overlap of high precision within the time-resolved experiment. Another manual stage in the laser beam-line is used to overlap the pulses within 1 ns.

are absorbed by the matter and an excited electronic state is created. To reach the atomic ground state, the photons of longer wavelengths and lower energy are re-emitted afterwards. The life time of the excited state is of the order of 0.5–10 ns. This causes a delay in the emission process, which should be taken into account. In the scintillation process, the incoming electrons deposit part of their energy inside the material to create excited states and produce electrons and holes. The latter move and transfer their energy to the luminescence centers which emit photons in the visible range. The time for the excitation energy to be transferred to the luminescence centers is defined as the scintillator rise time. For LYSO, it is already measured and amounts to several tens of picoseconds [98]. The time delay introduced by the scintillator rise time is small compared to the fluorescence life-time and far below the desired resolution of 1 ns using this method. Once the emission characteristics are well-known, this approach can be employed with a higher confidence. Although there is still room for further improvement, the experiment presents already a straightforward solution to accomplish pump-probe

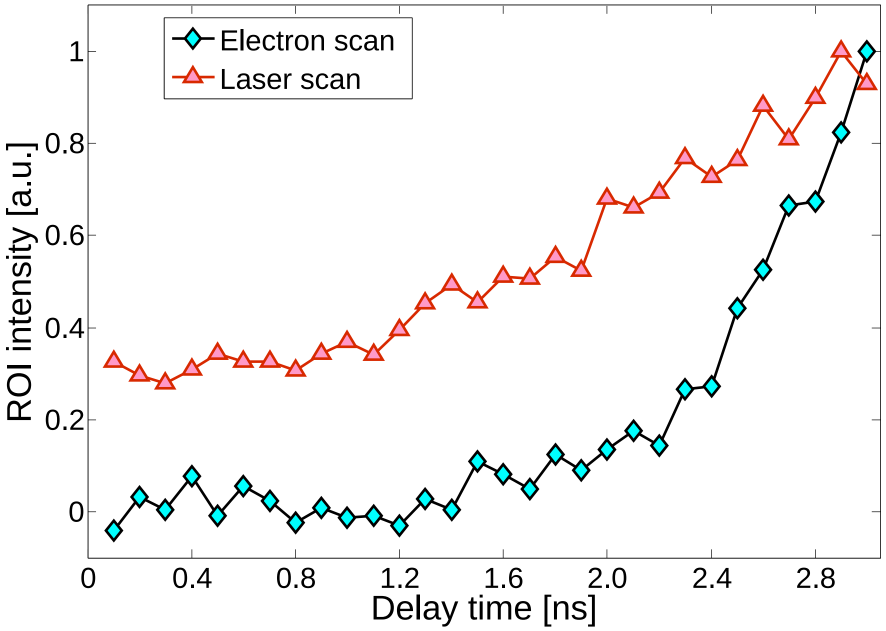

FIGURE 6.7: The intensity variation as a function of the time delay on the intensifier gate. It can be claimed that within 1 ns both signals related to the laser and electron pulses rise simultaneously.

type experiments with a resolution better than 1 ns.

By employing this method, the first time-resolved diffraction experiment was performed at REGAE. During this experiment, the laser-induced solid-liquid phase transition of polycrystalline gold was observed. Due to change in the structure of the gold sample after melting, the diffraction rings disappear. The best resolution that is provided in this way would be limited to the type of this evolutionary process, which in this case is of the order of several picoseconds. Thus, it can be claimed that the time zero is determined within this resolution [30].

6.6 Emittance measurement

All possible states of a particle in a beam can be represented in a 6-dimensional phase space consisting of 3-dimensional position space (x, y, z) and momentum space (p_x, p_y, p_z). The phase space can be decomposed in three orthogonal 2-dimensional position-momentum planes, (x, p_x), (y, p_y) and (z, p_z). The first two pairs describe the transverse plane and the last is considered as the longitudinal plane. The average spread of the particle's coordinates in the phase space is expressed by the emittance of the beam. Preserving a low emittance from the source to the end of an accelerator is of fundamental importance. Since the emittance is a characteristic of the beam, its measurement at different locations along a beam line or a linear accelerator allows to verify and improve the beam quality. At REGAE, for the purposes of ultra-fast relativistic electron diffraction (UED) and microscopy, the required temporal and spatial resolutions are achieved when a low-emittance beam is compressed to the characteristic length of the fast phenomenon under study (Table 2.1). Accordingly, the bunch charge is reduced to < 1 pC, while the existing beam diagnostics are capable of characterizing such low-charge beam. One of the most important UED parameters is the transverse coherence length, which is inversely proportional to the transverse emittance. The coherence length is a characteristic length of the beam propagation, in which the phase of the beam is changed by π radians. The longer the coherence length, the better the coherence of the beam is. The transverse coherence length, L_c, should be at least a few nanometers, or several times the dimension of a unit cell, to ensure high quality diffraction data [21]. Starting with a small beam at the cathode to suppress the thermal emittance (2.2), the beam extension on the transverse plane increases to improve the coherence length (see Eq. 1.4). For the same reason, a beam emittance as small as several nm-rad (Table 2.1) is desired (see Ref. 1.4). In Appendix C, the mathematical definition of the emittance, as well as explanations on the conventional methods that can be applied to measure this quantity at REGAE are given.

The current method for the emittance measurement at REGAE is the solenoid scan [99]. In this approach, in order to determine the beam emittance, a linear transverse space charge is included into the envelope equation. Sol 4-5 and Sol 6-7 are the commonly used focusing magnets and the beam size measurement is performed on the diffraction detection system. For the analyses of the solenoid scan measurements, two fit routines have been developed. Both are based on the least-square method. The first is analytic, while the second is a numerical algorithm. The lowest emittance value that has been measured with this method at REGAE is (74 ± 30) nm rad. Figure 6.8 shows one of his solenoid scans and the agreement between the data and the fit functions. In the following, two further approaches for beam emittance measurements are described.

6.6.1 Emittance measurement: shadow image of a TEM mesh

The technique for measuring the emittance from the shadow image of a TEM (electron microscopy transmission) grid, resembles the Pepper-pot method [100]. Both use a periodic sampling structure to determine the beam divergence in multiple positions in the transverse plane. The Pepper-pot technique enables a two-dimensional beam emittance measurement in the transverse plane. Small drilled holes in the Pepper-pot plate result in cutting the incident beam into small pieces, so called beamlets, each with a very low charge. That makes the Pepper-pot method more appropriate for emittance measurements in a space charge dominated regime. The emittance is determined based on geometrical properties of the beamlets, such as position and size, as well as the beamlet image size on the profile screen.

In order to install the samples under study in the relevant holder holes (Fig. 2.10), commercially available TEM grids can be used to hold them. Such object, with repeating structure, can be dedicated to measure the beam divergence and subsequently the beam emittance. Unlike the Pepper-pot technique, the opening area where the beam

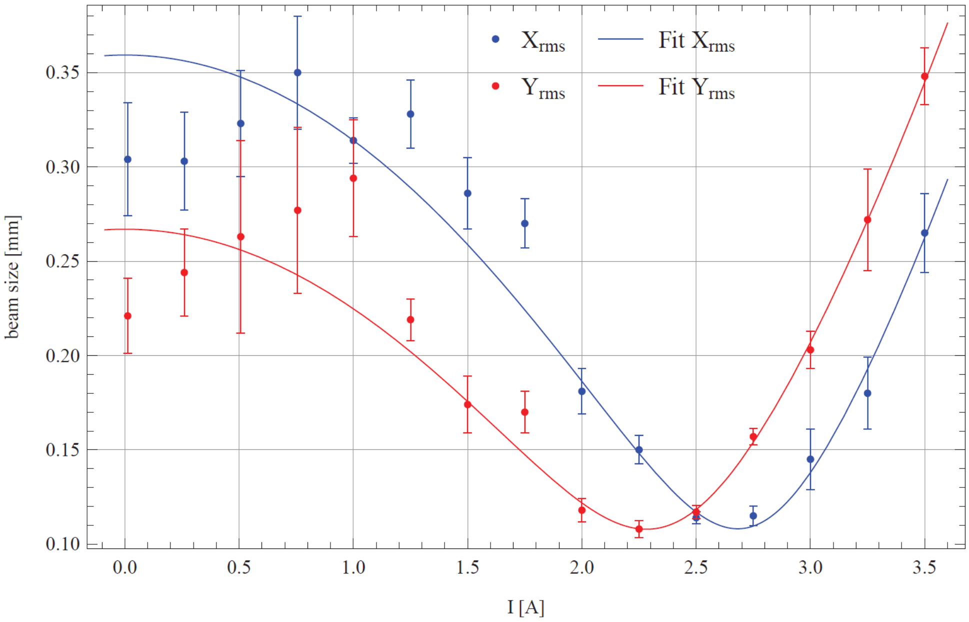

FIGURE 6.8: Solenoid scan data and transverse emittance fits in both x and y directions. The plot was created by M. Hachmann.

is transmitted, is larger. It makes this method more suitable for the low-charge case. This technique has been employed by the Pegasus facility at UCLA to measure order of nanometer emittance of ultra-low charge (<1 pC) beams [101]. These beams are created in RF photoinjectors and the laser is focused on the cathode to very small transverse sizes ($\sim<30$ μm).

If the beam intercepts the TEM mesh, a large fraction of electrons is transmitted through the opening holes. Those electrons that are blocked by the grid bars are scattered into large angles, such that with a high probability, they do not reach the profile monitor. In a Monte Carlo simulation with EGS5 [102], 10^4 electrons with kinetic energy of 2.3 MeV hit a 20 μm of copper plate (grid object) and it was shown that among all scattered electrons none of them was inside the acceptance cone of the beam path with a solid angle of 2.3 μrad. In the simulation, the electron momentum is about 4 MeV/c. The beam passed through the grid object and drifted further up to the FOS (see section 3.3.2), where the shadow image was created. The projection of each grid bar's edge characterizes the beam divergence. Subsequently, the beam distribution in trace-space, at the interaction position, is determined. In case of a fully transverse coherent electron beam, i.e. zero emittance and also ideal optics, which images a point object to a point image, the edge of the grid bar would be imaged very sharply. In practice, if the imaging resolution is good enough, the beam divergence distribution has the main contribution to blemish the edge. Based on the solution to the equation of motion of a charged particle in a drift space, the position distribution changes and the beam trace-space is sheared:

$$x = x_0 + x'L, \quad x' = x'_0, \tag{6.7}$$

where L is the length of the drift section and x' is the beam divergence. It is inferred that during the propagation of the beam along the drift, only the particles position alters and the divergence remains unchanged. If the divergence is characterized by a distribution, the width of the distribution $\sigma_{x\prime}$ represents the spread of the trajectory slope and describes how much the electrons cross over the border of the edge and cause the sharp edge to become curved. Figure 6.9 shows how the beam profile at the edges is influenced by the divergence of the beam. The beam profile at each edge of the bar can be described by an ”error function”. Subsequently, the entire intensity profile of both edges is introduced as [101]:

$$F(x) = erf(\frac{x + Ma/2}{\sqrt{2}L\sigma_{x'}}) - erf(\frac{x - Ma/2}{\sqrt{2}L\sigma_{x'}}), \tag{6.8}$$

where M is the magnification of the image and a is the bar width. One can use the given function to fit the intensity profile of each individual bar, which is characterized by its position and width. By varying $\sigma_{x'}$ as a fit parameter, the best agreement between the measurement and the fit is achieved. Thereafter, the width of the divergence and consequently the beam trace-space is obtained, from which the emittance is determined. One can approximate the contribution of the imaging quality in resolving the bar’s edge.

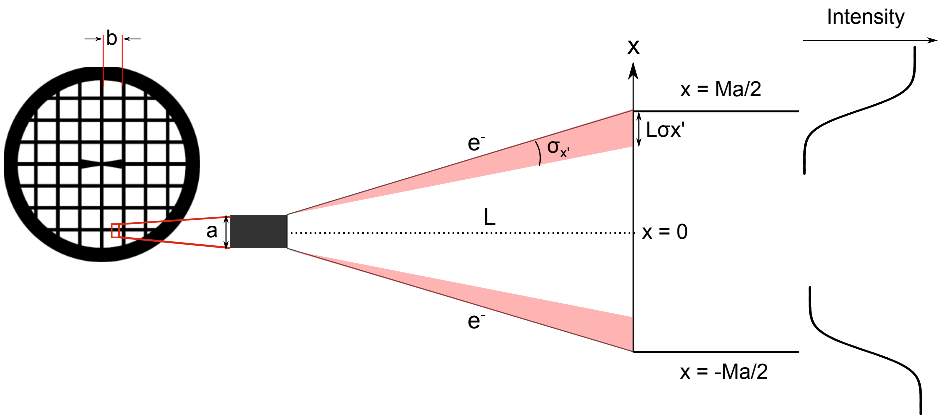

FIGURE 6.9: A zoom into a grid bar region on the left side. Incident electrons on the TEM mesh pass through the opening area of the grid and are blocked and scattered in the bar region. The transmitted beam has an inherent spread of the divergence ($\sigma_{x'}$) that causes the electrons to penetrate into the borders of the blocked area after long drift between the TEM mesh and the diffraction detector. Consequently, the measured intensity profile at both edges of each grid bar is not sharp but rather it resembles a curved edge profile.

The entire resolution of the beam profile monitor is estimated to be around 30 μm (see chapter 3). This is significantly smaller when compared to $L\sigma_{x'}$. L is 4 m and $\sigma_{x'}$ is estimated to be ∼40 μrad. Hence, the contribution of the profile monitor resolution in this analysis is considered to be negligible. Nevertheless, it has been taken into account in the final results.

As already mentioned, TEM grids exist at the sample holder but none of them are dedicated to the emittance measurements and small pieces of sample material lay on top of the grids. However, the empty spaces that are not covered by the specimens are used for this measurement. In the first configuration, the current of the solenoid 2-3 is adjusted so that the beam is brought to the target profile monitor with a small diverging angle, without further focusing in the drift space. The beam momentum is 4.36 MeV/c and the charge is 250 fC. Since the beam is not visible at the target screen, it is concluded that as a result of the large beam size, the intensity of the beam profile is not high enough to be diagnosed by the relevant diagnostics detector. One can move the sample holder transversally and replace the scintillator screen by a hole that contains both the TEM grid and sample. The beam passes through the mesh and drifts further towards the diffraction detector, where the shadow image is created. In order to acquire the beam transverse emittance at the target screen position, the shadow image should be analyzed. Figure 6.10 depicts the first configuration and the resulting images on the detector with and without a TEM mesh. The intensity projection of a single bar and a fit to the distribution, obtained from Eq. 6.8 are also shown. By analyzing different bar spots across the shadow image the averaged spread of the divergence is attained. The related normalized emittance in this experiment is measured to be 171±21 nm rad. The magnification of the shadow image along the drift between the target position and the detector is deduced from a structure in the shadow image, which is significantly larger than the bar width and in this particular case it is equal to the diameter of the sample's hole. From the known specifications, the diameter of the used TEM object is about 3 mm. Accordingly, a magnification of 1.8 was calculated. Although the beam was not visible at the profile monitor, it was detected on the diffraction detector of higher sensitivity. Based on the magnification value, the beam size on the target screen can be deduced. If $L\sigma_{x'}$ is larger than half size of the bar width $Ma/2$, there would be an overlap between the measured intensity profiles of the edges of the same bar. It can be shown that this condition is violated for this measurement. In order to avoid such overlap, either a mesh grid with a larger bar thickness should be used or the shadow image should be enlarged. The latter option is accomplished through a second configuration, in which the solenoid 4-5 is used to apply a sharp focus before the sampling target (see Fig. 6.11). Although the beam envelope is slightly spoiled due to space charge at the focusing point, the shadow image is significantly magnified so that any overlap between nearby edges is avoided. The beam momentum is 2.8 MeV/c and the bunch charge varies between 100–540 fC. The magnification is about M=16.

Figure 6.12 demonstrates the beam normalized emittance as a function of the bunch charge. For each measurement, 10 shots of shadow images were recorded and analyzed in single shot and in accumulation mode. Although this configuration is arranged to eliminate the problem associated with the first one, due to a strong focusing before the sample, the measured values do not correspond to the minimum achievable emittance.

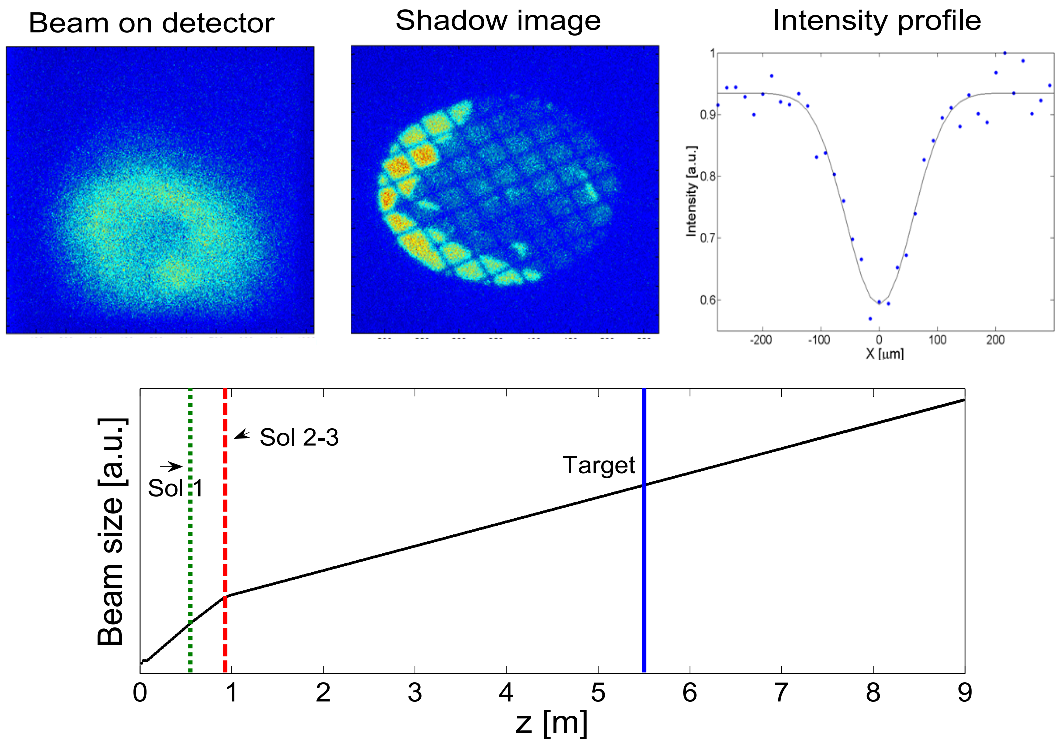

FIGURE 6.10: The first configuration to measure the beam emittance is shown at the bottom. The electron beam is imaged at the detector, when there is no TEM mesh in the beam line (top left). Also shown are the shadow image on the detector surface (top middle) and the intensity profile at the grid bar (top right). By fitting the distribution of the intensity profile, the beam divergence and consequently the beam emittance are obtained.

6.6.2 Emittance measurement: diffraction pattern

Analyzing diffraction patterns is another approach to measure the beam emittance. A criterion to determine the quality of a diffraction pattern is the ratio of the size of the central spot, x_0, to its distance from the diffracted beam spot, x_{diff}, which is represented by the diffraction ratio $R = x_0/x_{diff}$. If the ratio is minimized, the overlap of diffraction spots is avoided and the intensity of the spots is maximized. The position of the diffraction spot or the diffraction offset, follows the ordinary optics of a kicked central ray, if the space charge effects are neglected.

A quantitative comparison of the achievable diffraction ratio is required to optimize the focusing scheme. Three focusing configurations will be discussed.

1. Drift without focusing element, focus on the target

Rephrasing the equation of beam envelope development (see Eq. C.14) in a drift section of length L we have,

$$x_{rms}^2 = x_s^2 + 2x_s x_s' L + (\frac{\epsilon_{rms}^2}{x_s^2} + {x_s'}^2)L^2, \tag{6.9}$$

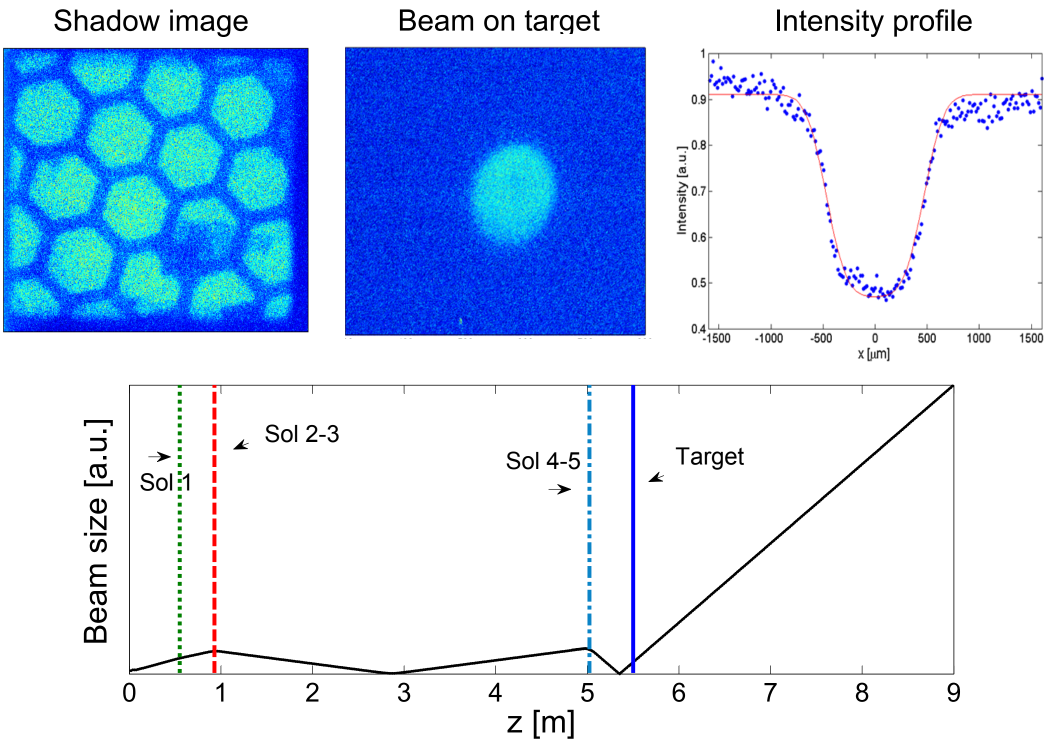

FIGURE 6.11: Second configuration for the measurement of the emittance. In this arrangement, solenoid 4-5 creates a focusing before the grid object. The magnification increases considerably as one can notice from the shadow image on the detector on the top left side. Unlike the previous configuration, the beam is visible at the target scintillator monitor in the middle and the beam size can be determined directly from the monitor. The intensity profile and the fitted function are also shown (top right).

where x_s is the RMS beam size, x'_s is the divergence of the RMS envelope at the entrance of the drift section and ϵ_{rms} denotes the geometrical emittance. Assuming that the incoming beam makes a focus on the target (x'_s=0) and then drifts to the detector screen, the beam envelope development simplifies to,

$$x_0^2 = x_s^2 + \frac{\epsilon_{rms}^2 L^2}{x_s^2}. \tag{6.10}$$

Here, x_0 and x_s represent the beam size on the target and the detector screen, respectively. L is the distance from the target to the detector screen. Subsequently, the diffraction ratio can be written as,

$$R = \frac{\left(x_s^2 + \frac{\epsilon_{rms}^2 L^2}{x_s^2}\right)^{1/2}}{x'_{diff} L}. \tag{6.11}$$

In case of a large distance L, one can ignore the first term of the numerator and the ratio becomes,

$$R = \frac{\epsilon_{rms}}{x_s x'_{diff}}. \tag{6.12}$$

If the beam on the target becomes convergent and $x'_s \leq 0$ in Eq. 6.9, the diffraction

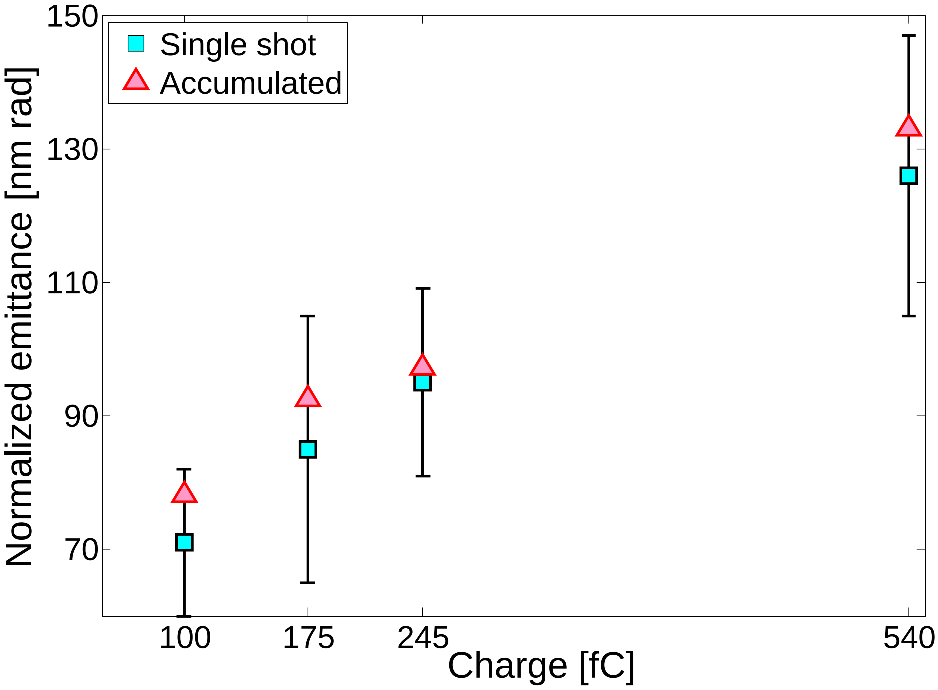

FIGURE 6.12: The normalized emittance as a function of the bunch charge. In total, 10 shots for each measurement were collected. Each individual shot was analyzed to measure the emittance in single shot. The error bars indicate the uncertainty of the single shot analyses. The emittance value was also deduced after averaging over 10 shots.

ratio is even smaller. Therefore, the next arrangement is based on a focused beam on the detector screen.

2. Drift without focusing element, focus on the detector screen

In this scheme, the entrance of the drift section is exchanged from the target to the detector screen, where the focusing takes place. Thus, Eq. 6.9 is given as,

$$x_s = \left(x_0^2 + \frac{\epsilon_{rms}^2 L^2}{x_0^2}\right)^{1/2}. \tag{6.13}$$

Solving for x_0 gives,

$$x_0^2 = \frac{x_s^2}{2} \pm \frac{x_s^2}{2}\sqrt{1 - \frac{4\epsilon_{rms}^2 L^2}{x_s^4}}. \tag{6.14}$$

Taking the negative sign of the solution and expanding the square root by keeping only the first two terms, the solution and consequently the diffraction ratio are given by,

$$x_0 \geq \frac{\epsilon_{rms} L}{x_s^2}, \qquad R \geq \frac{\epsilon_{rms}}{x_s x'_{diff}}. \tag{6.15}$$

The derived diffraction ratio resembles to Eq. 6.12.

3. **Focus on the detector screen, a focusing lens between target and screen**
   By adding a focusing lens between the target and the detector, the beam transfer matrix is given by,

$$M = M_{d2}.M_{sol}.M_{d1} = \begin{pmatrix} 1-\frac{d_2}{f} & d_1+d_2-\frac{d_1 d_2}{f} \\ -1/f & 1-\frac{d_1}{f} \end{pmatrix}. \tag{6.16}$$

If the particle trajectory on the target is transformed as,

$$M \begin{pmatrix} 0 \\ x'_{diff} \end{pmatrix} \Longrightarrow \qquad x_{diff} = x'_{diff} M_{12}, \tag{6.17}$$

then the position of the diffracted spot is determined.

Assuming that the focused plane is located at the entrance of the propagating section, which in this case is the detector screen, one should back-propagate the beam from the detector to the target. Then d_1 and d_2 should be exchanged and the matrix is written as,

$$M' = \begin{pmatrix} 1-\frac{d_1}{f} & d_1+d_2-\frac{d_1 d_2}{f} \\ -1/f & 1-\frac{d_2}{f} \end{pmatrix}, \tag{6.18}$$

where x_0, and x'_0 denote the beam position and the divergence on the detector screen, respectively. Applying the focusing condition at the detector, i.e. $x'_0 = 0$, the envelope equation yields,

$$x_s = \left({M'_{11}}^2 x_0^2 + \left(\frac{\epsilon_{rms}^2 + {M'_{12}}^2}{x_0^2} \right) \right)^{1/2}. \tag{6.19}$$

Similarly to Eq. 6.14, the solution for x_0 gives,

$$x_0^2 = \frac{x_s^2}{2{M'_{11}}^2} \pm \frac{x_s^2}{2{M'_{11}}^2} \sqrt{1 - \frac{4\epsilon_{rms}^2 {M'_{11}}^2 {M'_{12}}^2}{x_s^4}}. \tag{6.20}$$

Again, taking the negative sign and expanding the square root, the solution becomes,

$$x_0 \geq \frac{\epsilon_{rms} M'_{12}}{x_s}, \tag{6.21}$$

and consequently R is given by,

$$R \geq \frac{\epsilon_{rms}}{x_s\ x'_{diff}}. \tag{6.22}$$

For the time resolved electron diffraction experiment, the bunch length should be shortened to several femtoseconds. In order to avoid space charge broadenings, even within a low-charge bunch, the beam is extended transversally at the target position. This also improves the coherence length of the beam. Focusing the beam at the interaction point is not advantageous and therefore the first scheme is not favorable. The common diffraction setup at REGAE corresponds to the third configuration, in which the solenoid 6-7 is the focusing element between the target and the screen. In the case of the second configuration, when the buncher cavity is tuned in, it introduces a focusing on the beam, in a way that at some energies the diffraction pattern is over-focused on the detector screen and the image is not vivid enough. Hence, the normal diffraction setup is arranged to find the minimum diffraction ratio and measure the beam emittance. The focusing configuration is shown in Fig. 6.13.

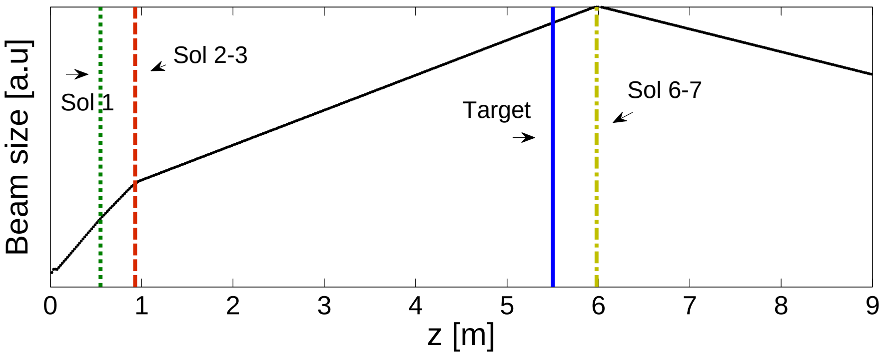

FIGURE 6.13: The focusing scheme chosen for emittance measurement, using diffraction patterns.

The entire procedure of the measurement involves the following steps:

- Measure the beam size on the detector, while the target is out of the beam line.
- Send the target into the beam line in order to create the diffraction pattern.
- Alter the solenoid 6-7 current in small steps, such that a clear pattern of diffraction is still observable. For each step, record the diffraction images in multiple shots.
- Find the minimum diffraction ratio for each magnet setting. The diffraction ratio is the ratio of the beam size, measured in the first step, to the distance between the central spot and the first order diffraction ring or spot, x_{diff}.
- Determine the beam size on the target screen, x_s. For this purpose, the sample should be replaced by the scintillator screen.
- Calculate the diffraction angle; this angle is two times larger than the Bragg angle and the Bragg relation for the first order can be approximated as,

$$2\ d\ \sin\theta = \lambda \quad \Longrightarrow \quad d\ x'_{diff} = \lambda, \tag{6.23}$$

  where d is the atomic plane spacing that can be deduced from the lattice parameter value, using Eq. 1.2 and θ denotes the Bragg angle. Using the relation between energy and wavelength, the diffraction angle is given by,

$$x'_{diff} = \frac{h}{m_0 dc\gamma}, \tag{6.24}$$

where γ is the Lorenz factor.

- Determine the emittance of the electron beam. Using the minimum diffraction ratio, the emittance is obtained from:

  $$\epsilon_{rms} = \frac{R_{min} x_s h}{dm_0 c\gamma}. \tag{6.25}$$

  The calculated value corresponds to the geometrical emittance. The normalized emittance is derived as,

  $$\epsilon_n = \frac{R_{min} x_s h}{dm_0 c}. \tag{6.26}$$

According to the diffraction data that were collected in November 2013, the normalized transverse emittance was measured as $\epsilon_n = (227 \pm 3)$ nm rad. The error is due to the uncertainty in the beam size measurement from shot to shot, on the detector and on the target screen. The beam momentum and charge were p=3.7 MeV/c and Q=270 fC. In Fig. 6.14, variation of x_0, x_{diff} and the diffraction ratio as a function of different solenoid settings is presented.

6.6.3 Simulation results

During the time of the experiments, due to lack of proper knowledge about the laser beam size on the photocathode, the setups were simulated for an uncertain range of the beam size values (0.1–0.3 mm). In all the measurements it was tried to tune the buncher cavity out of the beam line. However, due to cross talk of the cavity fields (see chapter 2), the effects of the buncher on the beam cannot be fully excluded, while the gun cavity is the only accelerating element in the simulations. Hence, the corresponding error is not taken into account in the uncertainty of the simulations.

In the first configuration of the shadow image experiment, the beam is at some points covered by small pieces of samples. Therefore, the analyses cannot be applied across the beam profile and the measured emittance can be underestimated. This problem will be resolved by installing grids fully dedicated to these measurements and free from any samples. The measured and simulated normalized trace-space emittance values are shown in Fig. 6.15.

In the second configuration, the simulations show that due to the steep focusing before the target, the emittance grows within the drift space, while in this method, the space charge induced emittance growth is ignored. Therefore, the emittance can be considerably underestimated (see Fig. 6.16).

According to Eq. 6.26, the normalized emittance is derived from parameters of the diffraction, while no knowledge about the beam energy is required. That points out the

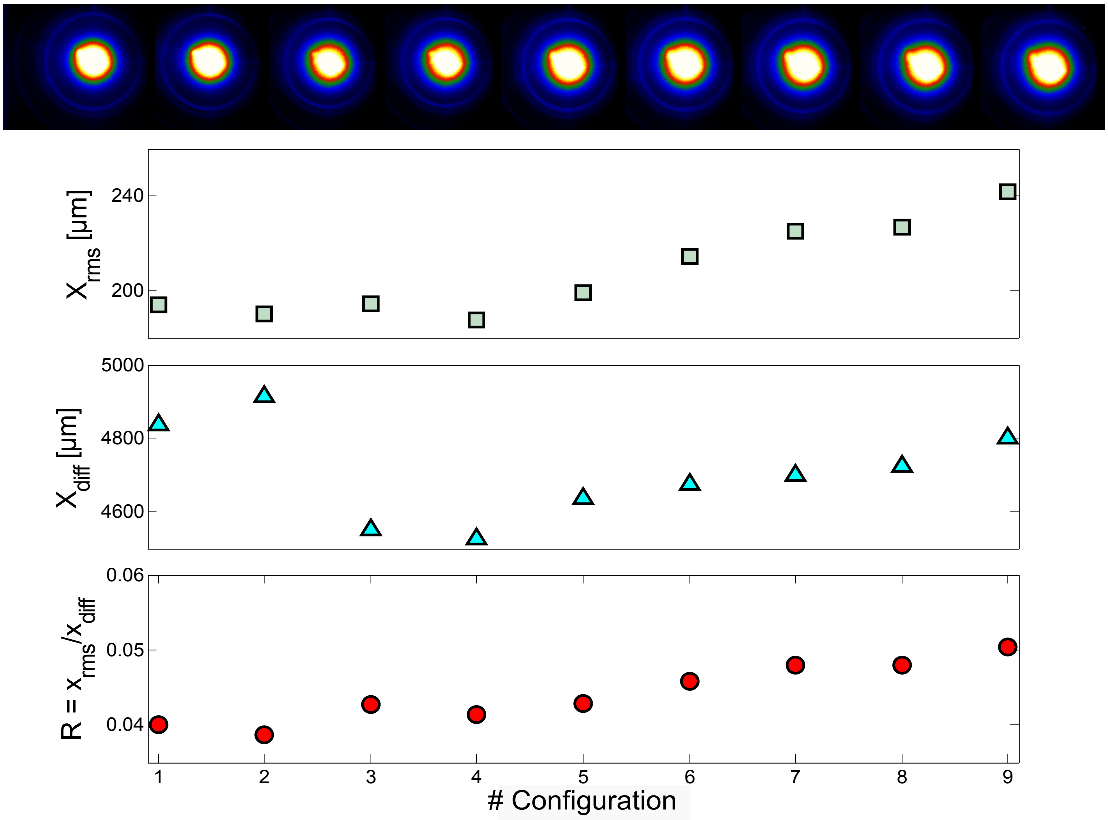

FIGURE 6.14: Beam size (top), offset of the diffracted order respect to the central spot (middle) and diffraction ratio (bottom) as a function of different configurations. The configurations are created based on different settings of solenoid 6-7. The minimum diffraction ratio occurs with the second configuration.

main advantage of this method over the conventional ones, of which uncertainty about the energy value is excluded from. The measurements and simulation results are shown in Fig. 6.17.

In summary, the approach to measure the emittance using the shadow image of a TEM grid was examined through two distinct configurations. The first one introduces a relatively small magnification. In the second configuration, a focusing solenoid introduces a sharp focusing before the target and the image is enlarged more profoundly to skip the overlap of the neighboring edge projections of the grid bars. However, the resulting emittance growth after the focusing is not taken into account in this method. Therefore, a moderate magnification is of interest, such that the space charge effect is minimized and does not affect the evaluation of the emittance. In the last approach, which employs the diffraction pattern to determine the emittance, the space charge effect is not taken into consideration, but these effects are negligible and do not influence the results. The measured emittance values agree with the simulation results within the uncertainties. The errors of the measurements are caused by the shot-to-shot fluctuations and inaccuracy of the measured quantities that are required to calculate the emittance. Both techniques can potentially be developed for performing a single shot, online emittance measurement. Further improvement of the experimental conditions would enhance the accuracy of such measurement.

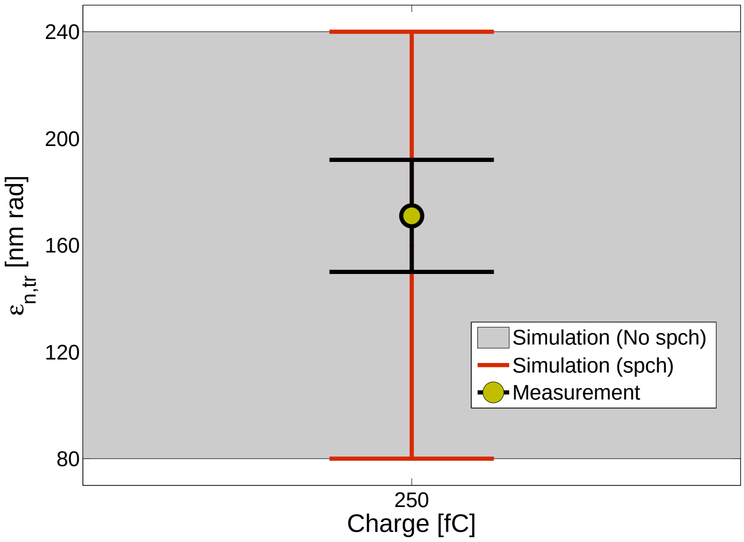

FIGURE 6.15: The measured and simulated emittance, obtained from the first configuration of the shadowgraphy. The grey band and the error bars represent the uncertainties. For the simulated emittance, two values are shown, one excluding the space charge forces (No spch) and the other including them (spch). The charge is Q=250 fC.

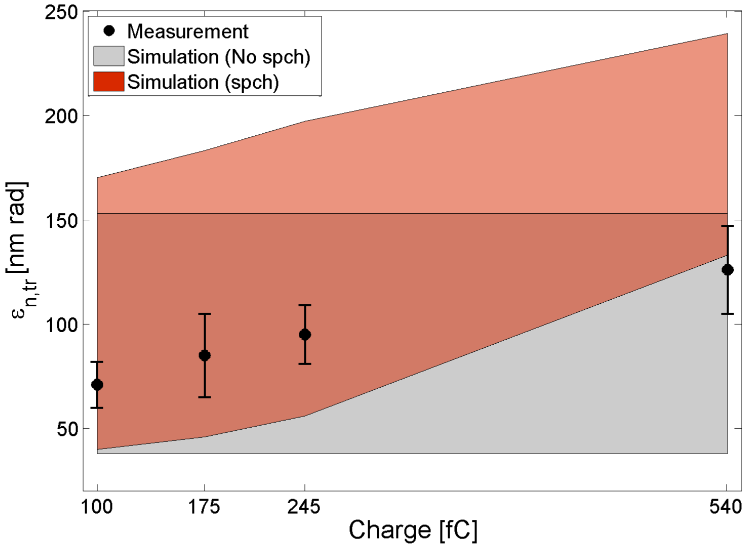

FIGURE 6.16: The measured and simulated emittance, obtained from the second configuration of the shadowgraphy. The bands and the error bars represent the uncertainties. For the simulated emittance, two values are shown, one excluding the space charge forces (No spch) and the other including them (spch).

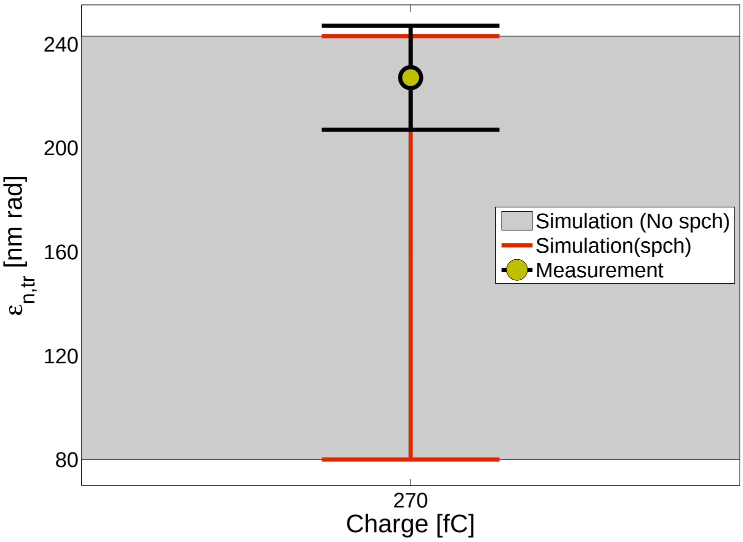

Figure 6.17: Emittance measurement and simulation results using diffraction pattern at Q=270 fC. The grey band and the error bars represent the uncertainties. For the simulated emittance, two values are shown, one excluding the space charge forces (No spch) and the other including them (spch).

Chapter 7

Summary and outlook

Femtosecond Electron Diffraction (FED) is a way to observe the atomic motions in real time. The time scale of atomic motions is of the order of $\sim$ 100 fs. To resolve such fast processes, electron bunches of the same or shorter length are required. The generation of such short electron pulses has become possible by means of femtosecond laser systems. However, the pulse length is influenced by space charge forces and the required resolution is consequently limited. Radio frequency (RF) photo injector facilities, such as REGAE, capable of generating MeV electrons, can be employed to suppress space charge effects in the relativistic regime. REGAE comprises of a photocathode located inside a normal conducting RF cavity, which can accelerate electrons to energies of 2–5 MeV. A buncher cavity is also used to compress the pulses down to several femtoseconds as an ultimate resolution for a time resolved diffraction experiment. Space charge broadening and consequently the temporal resolution are influenced by the beam current. Moreover, for a good quality of the diffraction pattern a high degree of coherence is required. Beam parameters such as a bunch charge of less than 100 fC to few pC, transverse emittance of $\approx$30 nm rad and a bunch length of 7–30 fs are required to fulfill the objective. Sophisticated diagnostics on a shot-to-shot basis is essential to generate and maintain these electron bunches. The main topic of this thesis is the transversal diagnostics, which covers the beam profile, as well as charge, energy and energy spread measurements. An excellent performance of the diagnostics system at very low charges is demonstrated. With the use of a high light yield scintillator material and efficient coupling optics and detection, very sensitive beam profile monitors were developed for the diagnostics system. The monitors, currently operating at REGAE, are based on electron-induced scintillator emission and apart from a superior sensitivity, they offer a wide dynamic range (few fC–few pC) by giving the possibility of switching between a normal and an intensified CCD. The behavior of the scintillator emission in terms of the scintillator material, thickness and geometry are characterized, using a Monte Carlo simulation tool, GEANT4. In addition, the coupling efficiency of the emission to the optics is derived and the collected part of the light is transported through the optical system, using a ray tracing program, ZEMAX. Included in the calculations are optical imperfections, absorption by the lens materials and the aperture limits, which are all causes for degrading the optical resolution and the transmission of light. The efforts on evaluating the CCD detector, resulted in the absolute calibration of the camera. Such calibration factor relates the digital count of the image on the detector to the photon flux, arriving on the detector surface. Eventually, the main elements of the profile monitor structure, such as scintillator emission and its coupling efficiency to the optics, light transmission through the optical system and the detection in the non-intensified mode are well-characterized. According to a direct charge calibration, distribution of an imaged profile returns the bunch charge distribution. Therefore, due to the excellent performance of the profile monitors at an ultra-low charge regime, not even they are introduced as an alternative to the charge monitors at this charge level, but also they cover a range that cannot be reached by any other diagnostics.

Response of the profile monitor to a point source (single electron) is a measure of resolution of the system. Convolution of the scintillator emission spread and imaging resolution, as well as considering the detector pixel size, the resolution of the system is obtained to be better than 30 μm, for the beam energy of 5 MeV and scintillator thickness of 0.3 mm.

A fast-gated image intensifier unit is coupled to a normal CCD by means of lens coupling and creates the intensified detection line. The minimum gating width of 50 ns accommodates the system to perform extra studies. In this direction, the measurement of the decay time of the LYSO scintillator, using the gated ICCD, is demonstrated. The acquired decay time of LYSO is measured to be around 45 ns, which is in agreement with the quoted values. The overlap between the electron probe pulse and the pump laser beam, in time and in position is of great importance in case of the time-resolved experiment. The existing monitor at the interaction point, facilitates the spatial overlap. However, taking advantage of the intensifier gating feature, the temporal overlap within 1 ns can be achieved. Although this precision is not sufficient for the objective femtosecond electron diffraction (FED) experiment, but it narrows the limit of uncertainty. The applications of the gated ICCD also extends to suppression of the dark current signal, induced by high gradient acceleration field. It is shown that the ratio of the signal to the dark current contribution improves significantly at shorter gate windows.

A transverse coherence length of several nanometers guaranties a good quality of the diffraction. The relevance between this diffraction parameter and the transverse emittance, which represents the beam quality, expresses the importance of evaluating the beam by measuring its emittance. At the moment of writing the present thesis, the ongoing emittance measurement at REGAE is performed by the "solenoid scan" technique, using the diffraction detector. In this thesis, Two additional methods for the measurement of the emittance are applied by the author and their results are presented in this thesis. The first one is a variation of the "Pepper-pot" technique and it returns the trace-space emittance from a projection of the transmission electron microscopy (TEM) grids at the target chamber. Through a newly introduced approach, the electron diffraction pattern is applied to determine the emittance. In this method, a knowledge about energy of the beam is not required and the uncertainty, associated with the energy measurement is excluded in evaluation of the beam emittance. Since the space charge effects are not taken into account in any of the methods, a good care must be taken to reduce these effects during the measurements and avoid underestimation of the emittance parameter.

Simulating the experimental model in particle tracking simulation, ASTRA, the measurement results have been examined. Due to the uncertainties about the beam size on the cathode, the simulated values vary within a range, over which the measurement values are placed upon. That exhibits an agreement between the measured and the theoretically expected quantities of the transverse emittance. Although, the measurements were performed with different machine settings, the obtained values (70–230 nm rad) are deviated form the design emittance value of 30 nm rad. Thus, further optimization is required to prepare a beam with the desired quality for the UED experiment. It is concluded that the examined methods could be further improved and finally employed in the machine for future potential transverse emittance measurements. Compared to the "solenoid scan", these techniques offer the advantage that they are significantly less time-consuming for single shot measurements, therefore they could be suitable for an online determination of the emittance. Further efforts are required to optimize the measurements configurations and improve the techniques.

Appendix A

Collision stopping power

The mean rate of energy loss by moderately relativistic charged heavy particles, is well-described by the Bethe equation [42],

$$\left\langle -\frac{dE}{dx} \right\rangle = Kz^2 \frac{Z}{A} \frac{1}{\beta^2} \left[\frac{1}{2} \ln \frac{2m_e c^2 \beta^2 \gamma^2 W_{max}}{I^2} - \beta^2 - \frac{\delta(\beta\gamma)}{2} \right]. \tag{A.1}$$

It describes the mean rate of energy loss in the region 0.1$\leq \beta\gamma \leq$1000 for intermediate-Z materials. The stopping power unit is expressed as MeV g^{-1} cm^2. K is a constant, z is charge of incident particle, Z is its atomic number, A denotes atomic mass of the medium, γ, the lorentz factor, is written as $(1 - \beta^2)^{-1/2}$, where $\beta = v/c$. I and W_{max} represent mean excitation of the medium and maximum energy transfer in a single collision, respectively. For a particle with mass M, the maximum energy transfer is given as [42],

$$W_{max} = \frac{2m_e c^2 \beta^2 \gamma^2}{1 + 2\gamma m_e/M + (m_e/M)^2}. \tag{A.2}$$

At low energies electrons and positrons primarily lose their energy mainly by ionization. While ionization loss increases logarithmically with energy, bremsstrahlung losses rise nearly linearly (fractional loss is nearly independent of energy), and dominates above the critical energy (where the ionization and bremsstrahlung cross sections are equal), a few tens of MeV in most materials. Stopping power differs for electrons and positrons, and both differ from stopping power for heavy particles because of the kinematics, spin, charge, and the identity of the incident electron with the electrons that it ionizes [42, 43].

Collision energy losses by electrons and positrons are given by [42],

$$\begin{aligned} \left\langle -\frac{dE}{dx} \right\rangle &= \frac{1}{2} K \frac{Z}{A} \frac{1}{\beta^2} \Big[\ln \frac{m_e c^2 \beta^2 \gamma^2 (m_e c^2 (1-1)/2)}{I^2} + (1 - \beta^2) \\ &- \frac{2\gamma - 1}{\gamma^2} \ln 2 + \frac{1}{8} (\frac{\gamma - 1}{\gamma})^2 - \delta \Big]. \end{aligned} \tag{A.3}$$

Apart from properties of the incident electron, some properties of the medium such as its density and thickness have a major impact on the amount of the deposited energy or the total stopping power. The total stopping power comprises of collision and radiative stopping powers. Collision stopping power is rate of the energy loss due to Coulomb collisions that result in the ionization and excitation of atoms, while energy loss, which is dominant at higher energies, is due to collisions with atoms and atomic electrons in which bremsstrahlung photons are emitted. Figure. A.1 demonstrates comparative diagrams of the secondary electrons and photons populations, as a result of interacting 1000 electrons with CsI and LYSO plates, with varying thickness (200 μm–500 μm). The deposited energy or equivalently stopping power increases with the thickness of the material. The more frequent number of the secondaries due to interaction with LYSO are produced, which is an indication of the higher stopping power is this medium. The electrons that populate the right side of the axis, have caused excitation and ionization of the medium atoms and loss of their associated primaries is characterized by the collision stopping power. Through the bremsstrahlung process, high energy X-ray photons are created and they populated the left side of the horizontal axis.

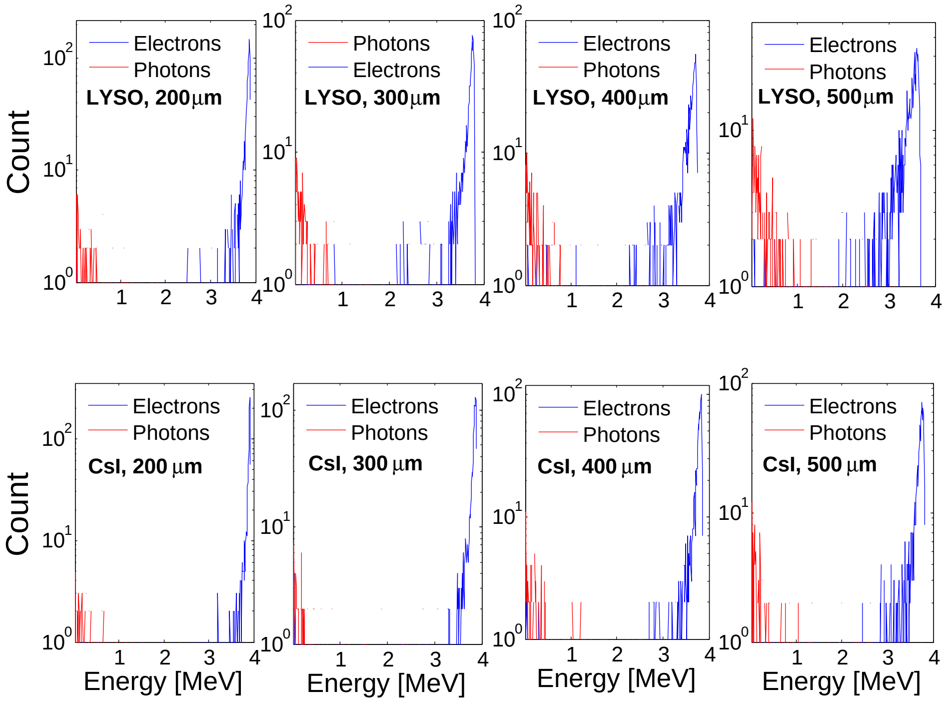

FIGURE A.1: Secondary emission generated from interaction of electrons with scintillator materials of LYSO and CsI.

Appendix B

Optical system, imaging concepts and imperfections

In order to create a complementary information of our disposal about imaging system of the beam profile monitors, some additional definitions of the optical concepts are further explained in this context. The presented material can be found in [103–106]

F-number ($f/\#$) The aperture that limits the amount of light passing through an optical object along its axis, is called the aperture stop. The aperture can be described by a dimensionless value, f-number, which is the ratio of the focal length (f) to the diameter of the aperture (D). A small F-number corresponds to a large aperture, which causes efficient light coupling to the optics.

Numerical aperture (NA) A dimensionless number that describes the range of angles over which the system can accept light, is the numerical aperture. For an optical system such as an objective lens, the NA is given by:

$$NA = n \sin\theta. \tag{B.1}$$

whereas, n specifies the refractive index in the object space. For a small acceptance angle, where $\sin(\theta) \approx \tan(\theta)$, the following relation holds between NA and f-number,

$$NA = \frac{1}{2f/\#}. \tag{B.2}$$

Depth of focus (DOF) The longitudinal distance along the optical axis between the two points where the image of the object can be seen sharply is called depth of focus,

$$DOF = 2.4(f/\#)^2\lambda. \tag{B.3}$$

Airy disk As a result of diffraction at the apertures of the lenses, it is not possible that a point object is imaged into an ideal point and the resolving power is limited by diffraction. A measure on the resolving power of the optics is the diameter of a so called Airy disk. A separation of x, equal to diameter of the Airy disk is required to resolve two distinct objects,

$$x = 1.22(f/\#)\lambda. \tag{B.4}$$

B.1 Ray tracing matrices

Ray tracing describes the propagation of the rays through an optical system. If the optical system is a simple lens, under paraxial approximation (optical aberrations are not taken into account), the position and the angle of the passing ray is changed following the general form of the lens matrix,

$$M = \begin{pmatrix} 1 + \frac{(n_1 - n_2)t}{n_2 R_1} & t/n_2 \\ (n_2 - n_1)\left(\frac{1}{R_2} - \frac{1}{R_1}\right) - \frac{t(n_1 - n_2)^2}{R_1 R_2 n_2} & 1 + \frac{(n_2 - 1)t}{R_2 n_2}, \end{pmatrix} \tag{B.5}$$

with R_1 and R_2 as curvature of the lens surfaces (input and output). t, n_1 and n_2 represent the lens thickness, refractive indices of the surrounding media and the lens material, respectively. If the lens thickness is negligible compared to the radii of curvature, the thin lens approximation can be used ($t \rightarrow 0$),

$$\begin{pmatrix} 1 & 0 \\ (n - 1)\left(\frac{1}{R_2} - \frac{1}{R_2}\right) & 1 \end{pmatrix}, \tag{B.6}$$

where, $n_1 = 1$ and $n = n_2$. The refractive power (D) describes the focusing strength of the lens (f) and is given by the lens maker's equation,

$$D = \frac{1}{f} = -(n - 1)\left(\frac{1}{R_2} - \frac{1}{R_1}\right) = \frac{1}{a} + \frac{1}{b}, \tag{B.7}$$

a and b are the object and the image position with respect to the lens. Using this definition, the Eq. B.6 is simplified to,

$$M = \begin{pmatrix} 1 & 0 \\ -1/f & 1 \end{pmatrix}. \tag{B.8}$$

Transformation matrices of a few important optical elements are given in table B.1.

B.2 Optical aberrations

Optical aberrations are deviations from a perfect, mathematical model. They can be caused by the lens shape itself, or placement of optical elements in a system, due to the wave nature of light. Optical aberrations are divided into two main categories: chromatic aberrations, caused by dispersion of light (multiple wavelengths) from the optical material and monochromatic aberrations, which are functions of the object point position and also depend on the lens parameters.

Table B.1: Transformation matrices of few optical elements. The wave nature of the rays and consequently optical aberrations are neglected.

Operation	**Transformation matrix**
Translation (along d)	$\begin{pmatrix} 1 & d \\ 0 & 1 \end{pmatrix}$
Refraction from a planar surface	$\begin{pmatrix} 1 & 0 \\ 0 & n_1/n_2 \end{pmatrix}$
Refraction from a curved surface	$\begin{pmatrix} 1 & 0 \\ \frac{n_1-n_2}{n_2 R} & n_1/n_2 \end{pmatrix}$
Lenses and curved mirrors	$\begin{pmatrix} 1 & 0 \\ -1/f & 1 \end{pmatrix}$

Monochromatic aberration Monochromatic aberrations are labeled with wavefront coefficients in addition to names. For example, the spherical aberration has a wavefront coefficient of W040. This wavefront coefficient arises from the mathematical summation that describes the actual difference between the perfect and aberrated wavefronts,

$$W = \sum_{l+k+m=0} W_{klm} H^k \rho^l \left(\cos(\theta)\right)^m , \tag{B.9}$$

W_{klm} is the wavefront coefficient and H is the normalized image height. The coordinate in the exit pupil is denoted by (ρ,θ). Some of the monochromatic aberrations, such as spherical aberration, coma, astigmatism, describe the blurring of the image point, Others describe the deviation of the best image point from its expected position. In table B.2, the wavefront coefficients related to each aberration are presented. Figure. B.1 shows images of a point source, which is aberrated in different ways.

Table B.2: Wavefront coefficients of different types of monochromatic aberrations.

Aberration type	Coefficient	Equation
Tilt	W_{111}	$W_{111} H \rho \cos\theta$
Defocus	W_{020}	$W_{020} \rho^2$
Spherical	W_{040}	$W_{040} \rho^4$
Coma	W_{131}	$W_{131} H \rho^3 \cos\theta$
Astigmatism	W_{222}	$W_{222} H \rho \cos\theta$
Field curvature	W_{220}	$W_{220} H^2 \rho^2$
Distorsion	W_{311}	$W_{311} H^3 \rho \cos\theta$

Chromatic aberration The effect of the dispersion can be described by Eq. B.7. While the object distance is fixed, the image distance changes with the index

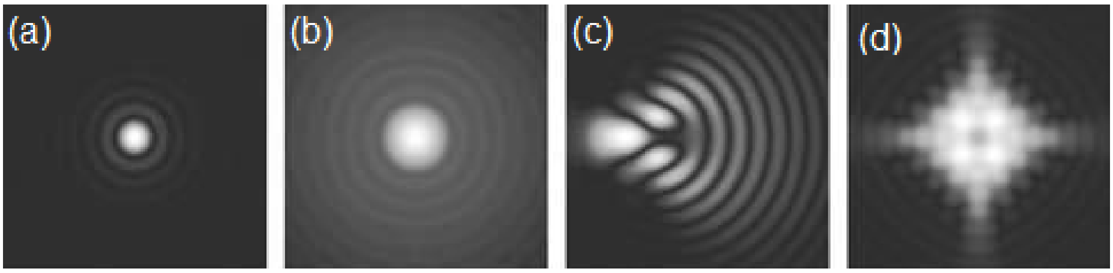

FIGURE B.1: Images of a point source under influence of different monochromatic aberrations: (a) Diffraction-limited, (b) Spherical aberration, (c) Coma, (d) Astigmatism. Figure from [103].

of refraction,

$$\Delta\frac{1}{b} = \frac{\Delta n}{n-1}\frac{1}{f}. \tag{B.10}$$

A combination of two or more lenses made from different glasses can then be designed, by a suitable choice of radii of curvature R for each component, to have equal focal lengths at two or more specified wavelengths. For the two neighboring lenses with focal lengths of $f_1$and f_2 we have $1/f = 1/f_1 + 1/f_2$. This remarks the addition of the refractive power of the lenses. If focal length of the system is not supposed to change, then,

$$\Delta\frac{1}{f} = \frac{\Delta n_1}{n_1-1}\frac{1}{f_1} + \frac{\Delta n_2}{n_2-1}\frac{1}{f_2} = 0. \tag{B.11}$$

This gives a condition on the correction of the chromatic effect by means of two lenses. Such a combination is called achromatic doublet or achromate lens.

Since some aberrations are caused by the lens parameters, the lens manufacturing is moving towards designing the aberrations free imaging systems. In Fig. B.2, Three products of Edmund optics company [107] are characterized. A Plano convex lens: has a positive focal length, ideal for collecting and focusing light in imaging applications, a doublet achromate: consists of two optical components cemented together, which is computer optimized to correct for on-axis spherical and chromatic aberrations and finally a precision aspherized achromatic lens: is truly achromatic and diffraction limited over the full visible spectrum. The "Ray Fan Plot" and the "Optical Path difference (OPD) plot" determine the different types and magnitudes of aberrations present in an optical system. The Ray Fan plots show the ray aberrations as a function of pupil coordinate and in the OPD plot, the difference between the path length of the ray and the path length of the aberration free wavefront is shown as a function of pupil coordinate. In an ideal optics, the difference tends to zero. Comparing the associated plots and the optical layout to each individual lens, one can see the great influence of the corrections on the image quality. The aspherized achromatic lens, introduces the most aberration free lens system among all, while the plano convex delivers a high-aberrated image.

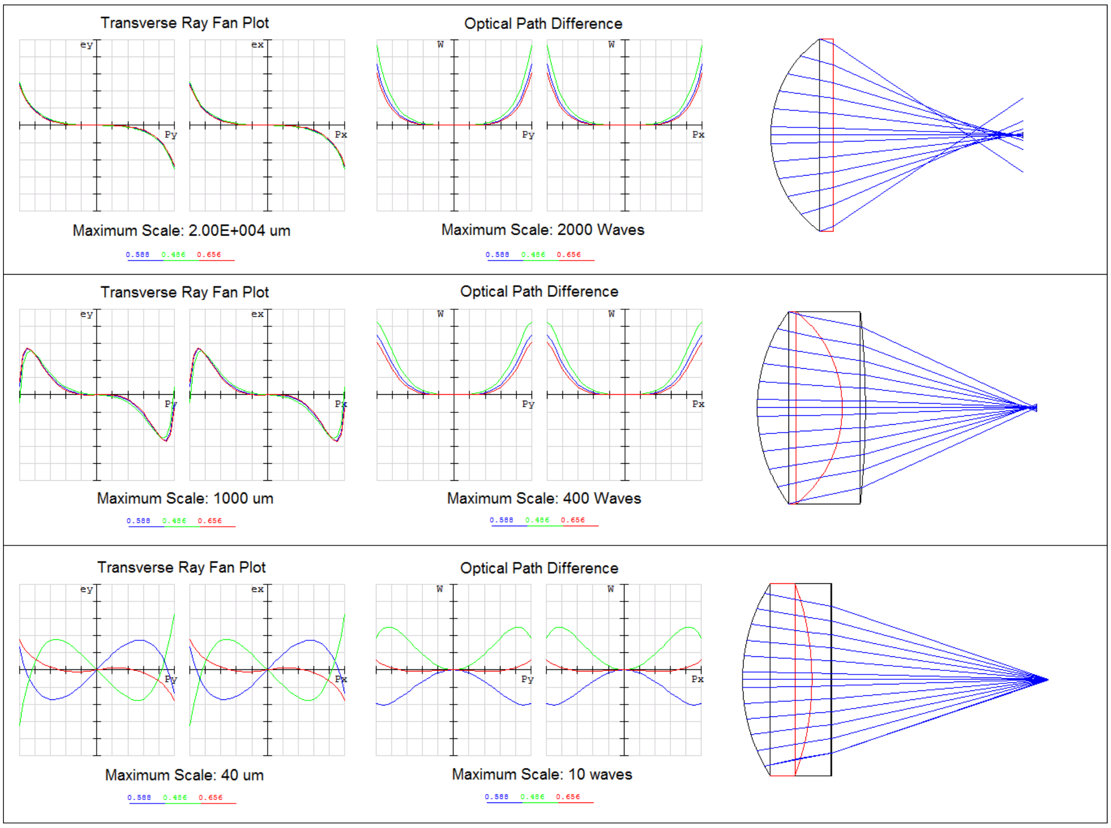

FIGURE B.2: Ray Fan, OPD plots and optical ray layout of a Plano Convex lens (top), a doublet achromatic (middle) and a precision aspherized achromatic lens (bottom). The lens diameters and focal lengths are identical.

Appendix C

Transverse emittance of the beam

The mathematical descriptions of the beam emittance, as well as two conventional methods to determine this quantity are explained within the context of this appendix. The presented material can be found in [108].

C.1 Beam optics: emittance

Particles inside a beam occupy an elliptical region in the phase space. The area of the ellipse divided by π is a measure of the beam's emittance. According to Liouville's theorem [109], the density of particles in phase space does not change along a beam transport line, under the influence of conservative forces (e.g. free from scattering and space charge forces). Therefore, as an invariant parameter of the beam, the emittance is of great importance to evaluate the beam quality in the accelerators. As the beam accelerates, the angles shrink and the emittance is therefore reduced. The approximation of an invariant emittance can still be valid if it is scaled to the beam energy, $\epsilon_n = \epsilon\beta\gamma$, where γ is the Lorenz factor and $\beta = v/c$. The normalized emittance is then constant as a function of the energy. The previously defined, non-normalized, emittance is the so called geometrical emittance.

For the trace-space emittance, the area occupied in the (x, x') and (y, y') planes is calculated, where $x' = p_x/p_z$ and $y' = p_y/p_z$. The trace-space beam emittance is then defined as,

$$\epsilon = \sqrt{\langle x^2 \rangle \langle x'^2 \rangle - \langle xx' \rangle}. \tag{C.1}$$

The ellipse in 2-dimensional trace-space, which encircles the particles of the beam is described as follows:

$$\gamma x^2 + 2\alpha x x' + \beta x x'^2 = \epsilon, \tag{C.2}$$

where x and x' denote the coordinates of a particle in the trace-space, representing the position and slope related to the particle, respectively. α, β, γ are the so called Courant-Snyder parameters, which determine the orientation and shape of the ellipse, while ϵ denotes the occupied area by the particles, i.e. the emittance. Based on the geometric properties of an ellipse, the Courant-Snyder parameters are related to each other according to the formula:

$$\beta\gamma - \alpha^2 = 1. \tag{C.3}$$

The beam half width is $\sqrt{\beta\epsilon}$ and the beam half divergence is $\sqrt{\gamma\epsilon}$. α also describes how x and x' are correlated; it is to zero at the beam "waist", where the beam size is minimum. Since the emittance remains invariant along the beam transport line, we only need to know how the ellipse parameters transform along the beam line to be able to describe the whole particle beam in the trace-space. If the initial ellipse at $Z = 0$ is described by

$$\gamma x_0^2 + 2\alpha_0 x_0 x_0' + \beta_0 {x_0'}^2 = \epsilon. \tag{C.4}$$

The trajectory of a particle from an initial point to any other point is transformed as:

$$\begin{pmatrix} x \\ x' \end{pmatrix} = \begin{pmatrix} C & S \\ C' & S' \end{pmatrix} \begin{pmatrix} x_0 \\ x_0' \end{pmatrix}, \tag{C.5}$$

$M = \begin{pmatrix} C & S \\ C' & S' \end{pmatrix}$ is the so called transfer matrix. Solving Eq. C.5 for x_0 and x_0' yields,

$$\begin{aligned} \epsilon &= (C'^2\beta_0 - 2S'C'\alpha_0 + S'^2\gamma_0)x^2 \\ &+ 2(-CC'\beta_0 + S'C\alpha_0 + SC'\alpha_0 - SS'\gamma_0)xx' \\ &+ (C^2\beta_0 - 2SC\alpha_0 + S^2\gamma_0)x'^2 \end{aligned} \tag{C.6}$$

After sorting Eq. C.6 the new ellipse parameters are,

$$\gamma = C'^2\beta_0 - 2S'C'\alpha_0, \tag{C.7}$$

$$\alpha = -CC'\beta_0 + (S'C + SC')\alpha_0 - SS'\gamma_0, \tag{C.8}$$

$$\beta = C^2\beta_0 - 2SC\alpha_0 + S^2\gamma_0 \tag{C.9}$$

The transport of the particle through each optical element is described by an individual transfer matrix. For instance, the matrix in a drift section can be written as,

$$M_{drift} = \begin{pmatrix} 1 & L \\ 0 & 1 \end{pmatrix}, \tag{C.10}$$

with L denoting the length of the drift section. Using the above transfer matrix in Eq. C.5, it can be noted that the position of the particles along the drift changes, while the slope of the trajectory does not. The transfer matrix of a focusing magnetic lens, in the thin lens approximation, is derived as,

$$M_{lens} = \begin{pmatrix} 1 & 0 \\ -1/f & 1 \end{pmatrix}, \tag{C.11}$$

where f is focal length of the lens and $1/f$ is the focusing strength of the magnetic lens. According to Eq. C.5, passing through the lens, the particles' positions remain almost constant, while their slopes change. In case of multiple optical elements in the beam line, the solution for the complete lattice of optical elements is the product of the individual matrices in the desired sequence. Figure C.1 shows the propagation of an electron beam along the z direction. A focusing magnet is the only existing element in the beam line. The divergent beam in the first drift space (L_a), is characterized by a rotated ellipse in trace-space, which extends from bottom left to upper right. After the lens, due to the change in the particle's divergence, the upper part moves from right to left while the lower part tends from left to right, meaning that the beam is convergent. In the second drift space (L_b), the upright ellipse characterizes the beam phase, where the beam size is minimum. For the described system, the transfer matrix from point a to c can be written as,

$$M = M_{drifc}\, M_{lens}\, M_{drifta} = \begin{pmatrix} 1 & L_c \\ 0 & 1 \end{pmatrix} \cdot \begin{pmatrix} 1 & 0 \\ -1/f & 1 \end{pmatrix} \cdot \begin{pmatrix} 1 & L_a \\ 0 & 1 \end{pmatrix}. \tag{C.12}$$

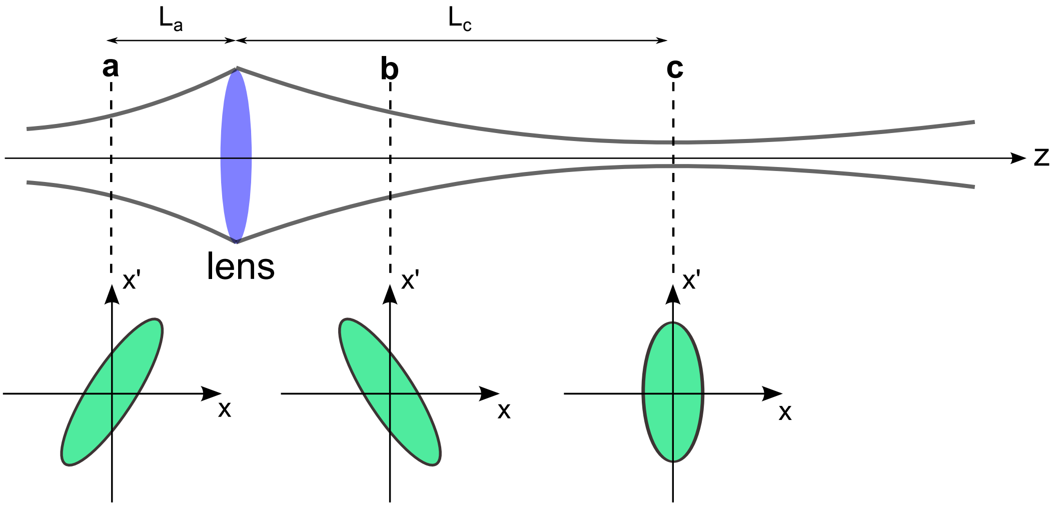

Figure C.1: The phase space ellipse evolution in orientation and size, as the beam propagate along the beam transport line. Starting from a divergent beam, the ellipse extends from lower left to upper right. After the focusing lens, it becomes convergent, represented by an ellipse extending from upper left to lower right. Further change occurs as the beam moves in a drift space toward the beam waist with the minimal size. For each state, one can define a transfer matrix, which describes the beam envelope with respect to the reference point.

C.2 About emittance measurement

From Eq. C.6, provided that the initial Courant-Snyder parameters and the transfer matrix elements are known, the emittance can be determined. However, the only measurable value of the beam in the transverse plane is the beam size. From the equation of motion (see Eq. C.5),

$$x = Cx_0 + Sx'_0 \tag{C.13}$$

and using Eq. C.1 the RMS envelope equation can be derived [99, 110],

$$x^2_{rms} = C^2 x^2_{0,rms} + 2CSx_{0,rms}(x_{0,rms})' + S^2(\frac{\epsilon^2_{rms}}{x^2_{0,rms}} + (x_{0,rms})'^2). \tag{C.14}$$

If the transverse beam size is measured at different locations or under different focusing conditions, so that different parts of the ellipse are probed by the beam size monitor, then the beam emittance can be determined.

C.2.1 Multi-screen method

In multi-screen methods, the beam width is measured on the transverse beam profile monitors along a drift section. At least three independent measurements are required to acquire $x_{0,rms}$, x'_{rms} and ϵ_{rms} at the reference point. For each point of measurement, the transfer matrix is defined based on the characteristic drift length (see Eq. C.10), which is the distance from the reference point to the relevant screen.

$$\begin{aligned} x^2_{1,rms} &= x^2_{0,rms} + 2L_1 x_{0,rms}(x_{0,rms})' + L^2_1(\frac{\epsilon^2_{rms}}{x^2_{0,rms}} + (x_{0,rms})'^2), \\ x^2_{2,rms} &= x^2_{0,rms} + 2L_2 x_{0,rms}(x_{0,rms})' + L^2_2(\frac{\epsilon^2_{rms}}{x^2_{0,rms}} + (x_{0,rms})'^2), \\ x^2_{3,rms} &= x^2_{0,rms} + 2L_3 x_{0,rms}(x_{0,rms})' + L^2_3(\frac{\epsilon^2_{rms}}{x^2_{0,rms}} + (x_{0,rms})'^2) \end{aligned} \tag{C.15}$$

$x_{1,rms}$, $x_{2,rms}$ and $x_{3,rms}$ denote the RMS of the beam size on each individual screen monitor. Three desired unknown values that are needed to determine the beam emittance can be obtained, consequently.

C.2.2 Quadrupole scan

Via the quadrupole scan method, different focusing strengths are introduced to a magnetic lens, while the RMS of the beam size is measured on a single screen downstream the lens. The transfer matrix is a product of the transfer matrices in the drift space after the lens (see Eq. C.10) and the focusing element (see Eq. C.11). Three different points in the focusing scan suffice to measure the emittance. Nevertheless, more points of measurements contribute to more accurate results.

$$\begin{aligned} x^2_{1,rms} &= (1-\tfrac{L}{f_1})^2 x^2_{0,rms} + 2(L-\tfrac{L^2}{f_1})^2 x_{0,rms}(x_{0,rms})' + L^2(\frac{\epsilon^2_{rms}}{x^2_{0,rms}} + (x_{0,rms})'^2), \\ x^2_{2,rms} &= (1-\tfrac{L}{f_2})^2 x^2_{0,rms} + 2(L-\tfrac{L^2}{f_2})^2 x_{0,rms}(x_{0,rms})' + L^2(\frac{\epsilon^2_{rms}}{x^2_{0,rms}} + (x_{0,rms})'^2), \\ x^2_{1,rms} &= (1-\tfrac{L}{f_3})^2 x^2_{0,rms} + 2(L-\tfrac{L^2}{f_3})^2 x_{0,rms}(x_{0,rms})' + L^2(\frac{\epsilon^2_{rms}}{x^2_{0,rms}} + (x_{0,rms})'^2) \end{aligned} \tag{C.16}$$

$x_{1,rms}$, $x_{2,rms}$ and $x_{3,rms}$ denote the RMS of the beam size on the screen monitor behind the lens. Applying the least square formalism to minimize the difference between the predicted beam size and the measured one, the best estimation of the ellipse parameters or the emittance is achieved. A descriptive sketch of both methods is illustrated in Fig. C.2. In the described emittance measurement methods, the effects of the space charge that cause the beam envelope to change are not taken into account.

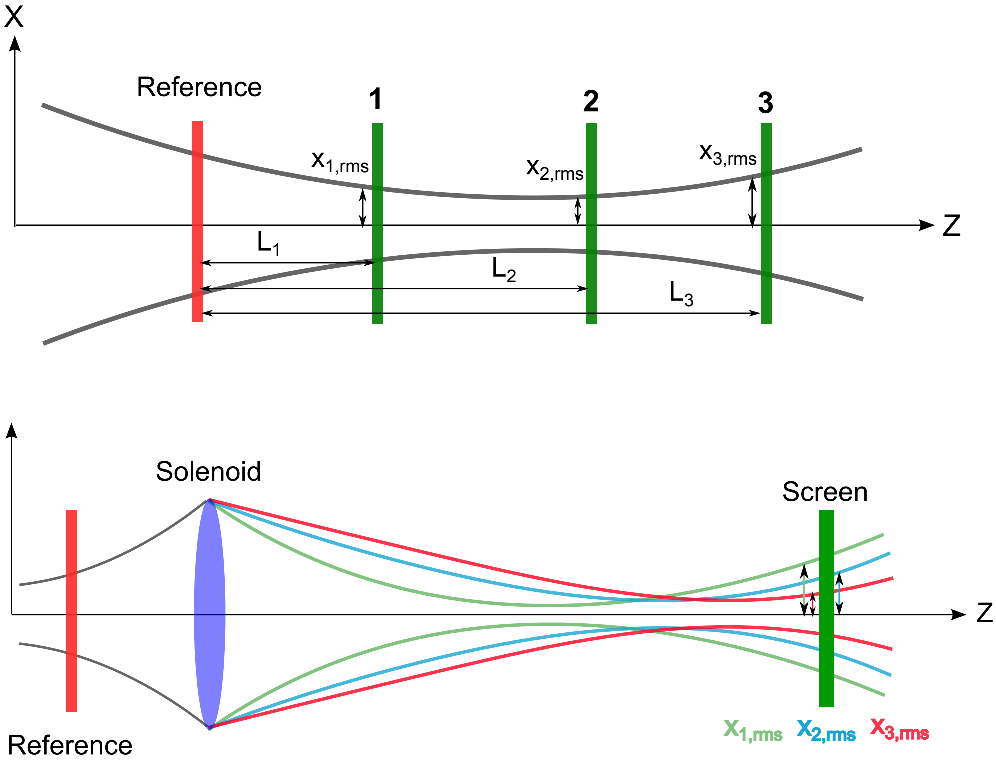

FIGURE C.2: Schematic of two methods for the measurement of the emittance, based on transverse beam profile characterization. In the multi-screen method (top), the beam size is measured on multiple transverse monitors along a drift space. The quadrupole scan method is based on measuring the beam size on a single screen as a function of the focusing strength of a focusing magnet upstream the monitor.

Bibliography

[1] C. Davisson and L. H. Germer. Diffraction of Electrons by a Crystal of Nickel. *Phys. Rev.*, 30:705–740, Dec 1927. URL `http://link.aps.org/doi/10.1103/PhysRev.30.705`.

[2] L. de Broglie. Recherches sur la theorie des quanta (Researches on the quantum theory). *PhD thesis*, 1924.

[3] L. de Broglie. Recherches sur la theorie des quanta (Researches on the quantum theory). *Ann. Phys. (Paris)*, 3, 1925.

[4] Ray F. Egerton. *Physical Principles of Electron Microscopy.* 2005.

[5] J. C. Polanyi and A. H. Zewail. Direct observation of the transition state. *Acc. Chem. Res*, 28:11932, 1995.

[6] R. J. D. Miller. 2000 John C. Polanyi Award LectureMother Nature and the molecular Big Bang. *Canadian Journal of Chemistry*, 80(1):1–24, 2002. URL `http://dx.doi.org/10.1139/v01-199`.

[7] R. J. D Miller. Making the Molecular Movie: First Frames Coming Soon with REGAE Musik. *Microscopy and Microanalysis*, 18:590–591, 7 2012. URL `http://journals.cambridge.org/article_S1431927612004801`.

[8] G. Sciaini and R. J. D Miller. Femtosecond electron diffraction: heralding the era of atomically resolved dynamics. *Reports on Progress in Physics*, 74(9):096101, 2011. URL `http://stacks.iop.org/0034-4885/74/i=9/a=096101`.

[9] B.K. Vainshtein. *Structure analysis by electron diffraction, tr.* URL `http://books.google.de/books?id=QmmRnQEACAAJ`.

[10] Hebeisen C. T. Ernstorfer R. Harb M. Deyirmenjian V. B Jordan R. E Dwyer, J. R. and R. J. D Miller. Femtosecond electron diffraction: 'making the molecular movies'. *Phil. Trans. R. Soc. A*, 364:741–778, 2006.

[11] PETRA III. URL `http://petra3.desy.de`.

[12] SPring-8. URL `http://www.spring8.or.jp/en/`.

[13] ESRF. URL `http://www.esrf.eu`.

[14] Free-electron laser FLASH. URL `http://flash.desy.de`.

[15] Linac Coherent Light Source (LCLS). URL `lcls.slac.stanford.edu/`.

[16] FERMI@Elettra. URL `www.elettra.trieste.it/FERMI/`.

[17] SACLA (XFEL). URL `xfel.riken.jp/eng/`.

[18] B. J. Siwick, J. R. Dwyer, R. E. Jordan, and R. J. D. Miller. An Atomic-Level View of Melting Using Femtosecond Electron Diffraction. *Science*, 302(5649):1382–1385, 2003. URL `http://www.sciencemag.org/content/302/5649/1382.abstract`.

[19] G. Sciaini et al. Electronic acceleration of atomic motions and disordering in Bismuth. *Nature*, 458:56–9, 2009. URL `http://dx.doi.org/10.1038/nature07788`.

[20] T. Wangler. *RF Linear Accelerator*. Wiley-VCH, New York, 1997.

[21] T. van Oudheusden, E. F. de Jong, S. B. van der Geer, W. P. E. M. Op Op Root, O. J. Luiten, and B. J. Siwick. Electron source concept for single-shot sub-100 fs electron diffraction in the 100 kev range. *Journal of Applied Physics*, 102(9):–, 2007. URL `http://scitation.aip.org/content/aip/journal/jap/102/9/10.1063/1.2801027`.

[22] REGAE, Time resolved diffraction with relativistic electrons. URL `http://regae.desy.de/`.

[23] J. B. Hastings, F. M. Rudakov, D. H. Dowell, J. F. Schmerge, J. D. Cardoza, J. M. Castro, S. M. Gierman, H. Loos, and P. M. Weber. Ultrafast time-resolved electron diffraction with megavolt electron beams. *Applied Physics Letters*, 89(18):184109, 2006. URL `http://scitation.aip.org/content/aip/journal/apl/89/18/10.1063/1.2372697`.

[24] P. Musumeci, J. T. Moody, C. M. Scoby, M. S. Gutierrez, and M. Westfall. Laser-induced melting of a single crystal gold sample by time-resolved ultrafast relativistic electron diffraction. *Applied Physics Letters*, 97(6):063502, 2010. URL `http://scitation.aip.org/content/aip/journal/apl/97/6/10.1063/1.3478005`.

[25] Li. Renkai, H. Wenhui, D. Yingchao, Y. Lixin, D. Qiang, S. Jiaru, H. Jianfei, C. Huaibi, D. Taibin, X. Haisheng, et al. Note: Single-shot continuously time-resolved MeV ultrafast electron diffraction. *Review of Scientific Instruments*, 81 (3):036110–036110, 2010.

[26] K. Floettmann. ASTRA simulation. URL `http://www.desy.de/~mpyflo/`.

[27] F. Mayet. Simulation and characterization of the RF system and global stability analysis at the REGAE linear electron accelerator. MS, University of Hamburg, 2012. URL `https://bib-pubdb1.desy.de/record/141143`. Masterarbeit.

[28] M. Felber, M. Hoffmann, U. Mavric, H. Schlarb, S. Schulz, et al. Laser Synchronization at REGAE using Phase Detection at an Intermediate Frequency. *Conf.Proc.*, C1205201:2624–2626, 2012.

[29] Coherent Company. URL `http://www.coherent.com/`.

[30] D. Zhang. Femtosecond Structural Dynamics on the Atomic Length Scale. *PhD thesis, University of Hamburg*, 2013. URL `http://www.physnet.uni-hamburg.de/services/fachinfo/___Kurzfassungen/Dongfang___Zhang.htm`.

[31] D. Strickland and G. Mourou. Compression of amplified chirped optical pulses. *Optics Communications*, 56(3):219 – 221, 1985. URL `http://www.sciencedirect.com/science/article/pii/0030401885901208`.

[32] K. Flottmann. Design and Performance of Printed Circuit Steering Magnets for the FLASH Injector. *Conf.Proc.*, C100523:MOPEB003, 2010.

[33] T. Gehrke. Design of Permanent Magnetic Solenoids for REGAE. Ms, University of Hamburg, 2013. URL `https://bib-pubdb1.desy.de/record/154592`. University of Hamburg, Masterarbeit, 2013.

[34] J. Hirscht. Collimators. URL `https://regae-wiki.desy.de/index.php/Collimators`.

[35] H. Delsim-Hashemi. Imaging Detector for Relativistic-Electron-Microscope REGAE. *REGAE Internal note*, 2012.

[36] S. Manz. Towards ultrafast electron diffraction and dynamic microscopy with REGAE. *Banff structural dynamics workshop*, 2013. URL `https://regae.desy.de/e135097/e135098/`.

[37] B. W. Reed, T. LaGrange, R. M. Shuttlesworth, D. J. Gibson, G. H. Campbell, and N. D. Browning. Characterization of ultrashort electron pulses by electron-laser pulse cross correlation. *Rev Sci Instrum*, 81(5):053706, 2010. URL `http://www.biomedsearch.com/nih/Solving-accelerator-condenser-coupling-problem/20515144.html`.

[38] T. Gehrke. Design of Permanent Magnetic Solenoids for REGAE. 2013. URL `http://www-library.desy.de/preparch/desy/thesis/desy-thesis-13-046.pdf`.

[39] Laboratory for Laser- and beam-driven plasma Acceleration (LAOLA). URL `http://laola.desy.de/`.

[40] M. Kronberger, C. W. Fabjan, and P. Lecoq. *Optimization of the light extraction from heavy inorganic scintillators*. PhD thesis, Vienna, Tech. U., Vienna, 2008. Presented on 18 Jun 2008.

[41] P. Lecoq, A. Annenkov, A. Gektin, M. Korzhik, and C. Pedrini. Inorganic scintillators for detector systems: Physical principles and crystal engineering. 2006.

[42] J. Beringer et al. Passage of particles through matter. *Particle Data Group*, PR 37, 2012. URL `http://pdg.lbl.gov/2013/reviews/rpp2013-rev-passage-particles-matter.pdf`.

[43] E. A. Uehling. Penetration of Heavy Charged Particles in Matter. *Annual Review of Nuclear Science*, 4(1):315–350, 1954. URL `http://dx.doi.org/10.1146/annurev.ns.04.120154.001531`.

[44] National Institute of standards and technology (NIST). URL http://physics.nist.gov/PhysRefData/Star/Text/ESTAR.html.

[45] A. Lempicki, A.J. Wojtowicz, and E. Berman. Fundamental limits of scintillator performance. *Nuclear Instruments and Methods in Physics Research Section A: Accelerators, Spectrometers, Detectors and Associated Equipment*, 333(23): 304 – 311, 1993. URL http://www.sciencedirect.com/science/article/pii/016890029391170R.

[46] D.W. Cooke, K.J. McClellan, B.L. Bennett, J. M. Roper, M. T. Whittaker, R. E. Muenchausen, and R. C. Sze. Crystal growth and optical characterization of cerium-doped $Lu_{1.8}Y_{0.2}SiO_5$. *Journal of Applied Physics*, 88(12):7360–7362, 2000.

[47] C.L. Melcher and J. S. Schweitzer. Cerium-doped lutetium oxyorthosilicate: a fast, efficient new scintillator. *Nuclear Science, IEEE Transactions on*, 39(4):502–505, 1992.

[48] B. Chai. Method of enhancing performance of cerium doped lutetium yttrium orthosilicate crystals and crystals produced thereby, January 23 2007. URL http://www.google.com/patents/US7166845. US Patent 7,166,845.

[49] J. Chen, L. Zhang, and R. Y. Zhu. Large size LYSO crystals for future high energy physics experiments. *Nuclear Science, IEEE Transactions on*, 52(6):3133–3140, 2005.

[50] Ludivine Pidol, Andree Kahn-Harari, Bruno Viana, E. Virey, Bernard Ferrand, P. Dorenbos, J. T M de Haas, and C. W E Van Eijk. High efficiency of lutetium silicate scintillators, Ce-doped LPS, and LYSO crystals. *Nuclear Science, IEEE Transactions on*, 51(3):1084–1087, 2004.

[51] R. Mao, L. Zhang, and R. Y. Zhu. LSO/LYSO Crystals for Future HEP Experiments. *Journal of Physics: Conference Series*, 293(1):012004, 2011. URL http://stacks.iop.org/1742-6596/293/i=1/a=012004.

[52] URL http://www.omegapiezo.com/.

[53] *Scintillation detectors Crismatec Saint Gobain Catalog*, 1992.

[54] T. K. Gupta. *Radiation, Ionization, and Detection in Nuclear Medicine*. Springer, 2013.

[55] Hamamatsu Photonics. X-ray Scintillator. URL http://shpat.com/docs/hamamatsu/ALS_ACS_FOS_TMCP1031E03.pdf.

[56] M. Ito, M. Yamaguchi, and K. Oba. CsI(Na) Scintillation Plate with High Spatial Resolution. *Nuclear Science, IEEE Transactions on*, 34(1):401–405, Feb 1987.

[57] S. M. Gruner, M. W. Tate, and E. F. Eikenberry. Charge-coupled device area X-ray detectors. *Review of Scientific Instruments*, 73(8), 2002.

[58] Geant4a simulation toolkit. *Nuclear Instruments and Methods in Physics Research Section A: Accelerators, Spectrometers, Detectors and Associated Equipment*, 506 (3):250 – 303, 2003. URL `http://www.sciencedirect.com/science/article/pii/S0168900203013688`.

[59] Absorption Length — CsI(Tl) Cesium iodide doped with Tallium. URL `http://gentitfx.fr/litrani/AllModules/FitMacros/AbsorptionLength_CsITl.C.html`.

[60] Index of refraction — CsI(Tl) Cesium iodide doped with Tallium. URL `http://gentitfx.fr/litrani/AllModules/FitMacros/RefrIndex_CsITl.C.html`.

[61] Andor Technology. URL `http://www.andor.com/pdfs/specifications/Andor_Neo_sCMOS_Specifications.pdf`.

[62] M. Thiel, W.M. Doring, V. Dormenev, P. Drexler, R.W. Novotny, M. Rost, and A Thomas. High-Energy Photon Detection With LYSO Crystals. *Nuclear Science, IEEE Transactions on*, 55(3):1425–1429, 2008.

[63] I. Holl, E. Lorenz, and G. Mageras. A measurement of the light yield of common inorganic scintillators. *IEEE Transactions on Nuclear Science*, 35:105–109, 1988.

[64] D. Lipka, J. Lund-Nielsen, and M. Seebach. Resonator for Charge Measurement at REGAE. 2nd International Beam Instrumentation Conference, Oxford(United Kingdom), 09/16/2013 - 09/19/2013 2013. URL `https://bib-pubdb1.desy.de/record/166172`.

[65] H. Delsim-Hashemi, K. Floettmann, M. Seebach, and Sh. Bayesteh. Charge Monitors at The Relativistic Electron Gun for Atomic Explorations - REGAE. 2nd International Beam Instrumentation Conference, Oxford(United Kingdom), 09/16/2013 - 09/19/2013 2013.

[66] A. A. Hebeisen T. C. Miller R. J. D Siwick, B. J. Green. Characterization of ultrashort electron pulses by electron-laser pulse cross correlation. *Opt. Lett.*, 30: 1057–9, 2003.

[67] K. Floettmann and V. V. Paramonov. Beam dynamics in transverse deflecting RF structures. *Phys. Rev. ST Accel. Beams*, 17:024001, 2014. URL `http://link.aps.org/doi/10.1103/PhysRevSTAB.17.024001`.

[68] V.L. Ginzburg and I.M. Frank. Radiation of a uniformly moving electron due to its transition from one medium into another. *J.Phys.(USSR)*, 9:353–362, 1945.

[69] P. Goldsmith and J. V. Jelley. Optical transition radiation from protons entering metal surfaces. *Philosophical Magazine*, 4(43):836–844, 1959. URL `http://dx.doi.org/10.1080/14786435908238241`.

[70] L. Froehlich. Thermal load on wirescanners in the flash linac. *Technical Note*, 2006. URL `https://bib-pubdb1.desy.de/record/81062`.

[71] S. Wesch and B. Schmidt. Summary of COTR effects. *Proceedings of DIPAC Conference*, 2011.

[72] M. Yan. *Suppression of COTR in Electron Beam Imaging Diagnosis at FLASH*. DESY thesis. DESY, 2011. URL `http://books.google.de/books?id=N7tPMwEACAAJ`.

[73] G. B. Airy. On the Diffraction of an Object-glass with Circular Aperture. *Transactions of the Cambridge Philosophical Society.*, 5, No Date Available. URL `http://citebank.org/uid.php?id=120424`.

[74] C. E. Shannon. Communication in the presence of noise. *Proc. Institute of Radio Engineers*, 37:10–21, 1949.

[75] S. Agostinelli et al. GEANT4: A Simulation toolkit. *Nucl.Instrum.Meth.*, A506: 250–303, 2003.

[76] Radiant Zemax. URL `https://www.radiantzemax.com/en`.

[77] W. Smith. *Modern Optical Engineering, 4th Ed.* McGraw Hill professional. McGraw-Hill Education, 2007. URL `http://books.google.de/books?id=DrtM_bAnf_YC`.

[78] RCA Corporation. *RCA electro-optics handbook*. Technical series - RCA Corporation. RCA/Commercial Engineering, 1974. URL `http://books.google.de/books?id=VNaZAAAAIAAJ`.

[79] H. Delsim-Hashemi, Sh. Bayesteh, and K. Floettmann. Diagnostics of electron bunches at REGAE. *Banff Meeting on Structural Dynamics, Poster presentation*, 2012.

[80] APPLIED IMAGE Inc. USAF 1951 Chart Standard Layout Product Specifications . URL `http://www.aig-imaging.com/mm5/PDF/USAF%201951%20Test%20Target%20T-20_v1-04.pdf`.

[81] F. J. Richards. A Flexible Growth Function for Empirical Use. *Journal of Experimental Botany*, 10(2):290–301, 1959. URL `http://jxb.oxfordjournals.org/content/10/2/290.abstract`.

[82] W. Boyle and G. Smith. Buried channel charge coupled devices, February 12 1974. URL `http://www.google.com/patents/US3792322`. US Patent 3,792,322.

[83] W. Boyle and G. Smith. Three dimensional charge coupled devices, March 12 1974. URL `http://www.google.com/patents/US3796927`. US Patent 3,796,927.

[84] H. Kikuchi, H. Takaoka, and S. Baba. Complementary metal-oxide semiconductor, September 8 1981. URL `http://www.google.com/patents/US4288804`. US Patent 4,288,804.

[85] Scientific CMOS Technology. URL `http://www.scmos.com/files/low/scmos_white_paper_2mb.pdf`.

[86] AVT Prosilica GC Technical Manual. URL `http://www.alliedvisiontec.com/fileadmin/content/PDF/Products/Technical_Manual/Prosilica_GC/70-0064_GC_TechMan_V2.0.pdf`.

[87] Sony, ICX285AL. Diagonal 11 mm (Type 2/3) Progressive Scan CCD Image. URL http://www.1stvision.com/cameras/sensor_specs/ICX285.pdf.

[88] Sony. XCG-H280E technical datasheet. . URL http://www.automationnet.de/fileserver/henrich/files/4905.pdf.

[89] Sony. XCGH280E High Speed GigE Camera. . URL http://pro.sony.com/bbsc/ssr/product-XCGH280E/.

[90] ANDOR, An Oxford Instrument Company. URL http://www.andor.com/.

[91] Electron Multiplying Charged Coupled device. URL http://www.emccd.com/.

[92] R.A. Taylor and G.L. Solbrekken. Comprehensive system-level optimization of thermoelectric devices for electronic cooling applications. *Components and Packaging Technologies, IEEE Transactions on*, 31(1):23–31, 2008.

[93] ANDOR. Rolling and Global Shutter. . URL http://www.andor.com/learning-academy/rolling-and-global-shutter-exposure-flexibility.

[94] S. B. Howell, R. Ellis, J. Huchra, S. Kahn, G. Rieke, and P. B. Stetson. *Handbook of CCD Astronomy; 2nd ed.* Cambridge Univ. Press, Cambridge, 2006.

[95] ANDOR. CCD Detectors, Course Notes. . URL http://www.lot-qd.de/files/downloads/andor/en/cc_notesccd_deen.pdf.

[96] ANDOR. Concepts in Digital Imaging Technology, Quantum Efficiency. . URL http://hamamatsu.magnet.fsu.edu/articles/quantumefficiency.html.

[97] B.H.T. Chai and Y. Ji. Lutetium Yttrium Orthosilicate single crystal scintillator detector, July 26 2005. URL https://www.google.de/patents/US6921901. US Patent 6,921,901.

[98] S. Seifert, J. H. L. Steenbergen, H. T. van Dam, and D. R. Schaart. Accurate measurement of the rise and decay times of fast scintillators with solid state photon counters. *Journal of Instrumentation*, 7(09):P09004, 2012. URL http://stacks.iop.org/1748-0221/7/i=09/a=P09004.

[99] M. Hachmann. *Transverse Emittance Measurement at REGAE Via a Solenoid Scan*. DESY thesis. DESY, 2012. URL http://books.google.de/books?id=H27omgEACAAJ.

[100] M. Zhang. Emittance Formula for Slits and Pepper-pot Measurement. *FERMILAB-TM-1988*, 1996.

[101] R. K. Li, K. G. Roberts, C. M. Scoby, H. To, and P. Musumeci. Nanometer emittance ultralow charge beams from RF photoinjectors. *Phys. Rev. ST Accel. Beams*, 15:090702, Sep 2012. URL http://link.aps.org/doi/10.1103/PhysRevSTAB.15.090702.

[102] H. Hirayama, Y. Namito, A.F. Bielajew, S.J. Wilderman, and W.R. Nelson. The EGS5 code system. 2005.

[103] A. Lipson, S. G Lipson, and H. Lipson. *Optical Physics; 4th ed.* Cambridge Univ. Press, Cambridge, 2011.

[104] D. Meschede. *Optics, Light and Lasers: The Practical Approach to Modern Aspects of Photonics and Laser Physics, 2nd, Revised and Enlarged Edition.* Wiley-VCH, Berlin, 2006.

[105] E. Dereniak and T. Dereniak. *Geometric and Trigonometric Optics. 1st ed.* Cambridge Univ. Press, New York, 2008.

[106] Edmund optics. Chromatic and Monochromatic Optical Aberrations. URL `http://www.edmundoptics.com/technical-resources-center/optics/chromatic-and-monochromatic-optical-aberrations/`.

[107] Edmund optics website. URL `http://www.edmundoptics.com/`.

[108] H. Wiedemann. *Particle Accelerator Physics.* SpringerLink: Springer e-Books. Springer, 2007. ISBN 9783540490456. URL `http://books.google.de/books?id=S8CfmLe87RAC`.

[109] J. Liouville. Sur la théorie des Êquations transcendantes. *Journ. de Math.*, 3: 337–354, 2007.

[110] K. Floettmann. Beam dynamics in RF guns and injectors. *Draft version*, 3:337–354, 2011.

Achknowledgments

This thesis would not have been possible without the help and contributions of a number of people.

First of all, I am indebted to my supervisors. All of them have been instrumental in the production of the work that went into this dissertation. I owe deep gratitude to my supervisor Jörg Roßbach for taking me on as his student and for his constant support and encouragement throughout my years working at DESY. My warmest acknowledgment goes to Hossein Delsim-Hashemi for his continuous guidance, explanations and true commitment to all the projects we worked on together. His support and supervision were absolutely paramount for the completion of this dissertation. I am equally and deeply grateful to my third supervisor, Klaus Flöttmann, for his insightful advices that shaped many of the concepts presented in this thesis, as well as for all his encouragement and unreserved help. A very special thanks is also dedicated to the project leader of REGAE, R.J. Dwayne Miller, for his unconditional support and help that were vital for me to continue working on my project.

During my time as a doctoral student I was blessed with a friendly and cheerful group of hard working and talented scientists at REGAE. I learned a lot from all of them. Many thanks go to Sascha Epp, Dongfang Zhang, Stephanie Manz, Masaki Hada, Yin Peng Zhong, Rolf Loch, Albert Casandruc, Max Hachmann and Frank Mayet. I am especially thankful to Sascha for his valuable input during the writing of this thesis. I would also like to thank my DESY colleagues Gero Kube, Hans-Christian Schroeder, Stefan Weisse, Michael Seebach, Carsten Kluth, Rolf Zahn, Josef Gonschior, Carsten Meklenburg and Valeri Saveliev, for their scientific and technical support, but also for all their valuable advices and contributions.

This work would not have been possible without the financial support of the GrK 1355 initiative of the University of Hamburg and of the Max Plank Research Department for Structural Dynamics. To both institutions I am grateful for allowing me to work under excellent conditions.

Outside the working environment, my time in Hamburg was made more cheerful and colorful thanks to a number of close friends: Nezhla Aghaei, Reza Mehrshad Hodajerdi, Reza Safari and Roxana Tarkeshian. I am grateful for the time we spent together. It certainly made the time to complete this thesis so much more pleasant.

My deepest and sincere gratitude goes to my family for their continuous and unconditional love and support. I am forever indebted to my parents for their endless sacrifice. I cannot express how grateful I am to them for enabling my dreams and visions to come true. This work is dedicated to them.

Last but certainly not the least, for his constant and unfailing care and love, I am enormously thankful to my dearest, Panos Katsas. Without his support, encouragement and patience I would never have succeeded to complete this work.